MORPHOLOGY OF LIQUID TIN SHEETS FORMED BY LASER IMPACT ON DROPLETS

VRIJE UNIVERSITEIT

MORPHOLOGY OF LIQUID TIN SHEETS FORMED BY LASER IMPACT ON DROPLETS

ACADEMISCH PROEFSCHRIFT

ter verkrijging van de graad Doctor of Philosophy aan
de Vrije Universiteit Amsterdam,
op gezag van de rector magnificus
prof.dr. J.J.G. Geurts,
in het openbaar te verdedigen
ten overstaan van de promotiecommissie
van de Faculteit der Bètawetenschappen
op dinsdag 13 december 2022 om 13.45 uur
in een bijeenkomst van de universiteit,
De Boelelaan 1105

door

Bo Liu

geboren te Hunan, China

Cover: A front-view picture of a liquid tin sheet that reflects light at 30° angle of incident. The reflection light reveals characteristic features of the sheet morphology such as a center disk, ripples (induced by capillary instabilities) at the liquid interface, a bounding rim, ligaments, and fragments.

Bookmark: The background is a twilight sky photo taken from Science Park, Amsterdam.

CONTENTS

CHAPTER 1

INTRODUCTION

As memorably captured in the movie *2001: A Space Odyssey*, the evolution of technologies developed by humans has taken several steps, from the creation of primitive stone tools, to more recent breakthroughs in space exploration [1] and artificial intelligence [2], to name a few. The flourishing of these technologies is often attributed to the ever-increasing capacity and complexity of integrated circuits, or microchips. On a microchip, a large number of electronic components such as transistors, resistors, and capacitors are integrated, providing the foundation for almost every electronic device used today. Increasing the spatial density of such components on a chip enables the production of smaller and faster devices. Photolithography is the defining step in determining the density of the electronic components on microchips [3, 4]. It uses light to image a pattern – determined by a so-called "optical mask" – onto a photosensitive material coated on the surface of a substrate, that is, a silicon wafer [5, 6]. This process, also called the exposure, is followed by a series of treatments including chemical development, etching, and deposition, forming a certain structure on the surface of the wafer [6, 7]. The complete fabrication of the patterns on the microchips is then achieved by repeating this cycle of coating, exposure, and so on.

As indicated by its name, photolithography shares fundamental principles with an optical system whose optical resolution can be improved by employing a shorter wavelength. In the pursuit of ever-smaller microchip features, the wavelength of light used in the exposure process has shrunk over time: from 436 nm wavelength visible light in the early stages [8], to the current state-of-the-art 13.5 nm wavelength extreme ultraviolet (EUV) light [8, 9].

1.1   Microdroplet-tin LPP source for EUV lithography

One of the sources for the photons at 13.5 nm is laser-produced plasma (LPP), generated by firing a high-energy laser pulse onto a material target. Current state-of-the-art sources for lithography produce a tin-plasma by focusing a CO_2 laser onto a liquid tin microdroplet which is delivered by a droplet generator. The subsequent emission of EUV light by the tin plasma is redirected to the scanner by a collector mirror — a multilayer mirror that is typically located in the vicinity of the laser-droplet interaction region [10–12]. The CO_2 laser is chosen not only for its commercial availability at the required high laser output power, but also due to its high conversion efficiency (CE), that is, the ratio of in-band EUV light emitted within a 2% bandwidth centered as 13.5 nm into the half-sphere covered by the collector mirror, over the energy of the drive laser.

1.1.1   Prepulse-induced dynamics of a droplet

One of the primary requirements for an EUV source is that it generates sufficient output in-band EUV power at high CE. Key breakthroughs meeting this requirement came with the introduction of a separate laser pulse, named *prepulse*, which interacts with the droplet prior to the arrival of the *main pulse* that generates the tin plasma and the subsequent EUV emission. The operating principle of this two-step scheme is illustrated in Fig. 1.1. The goal of the prepulse is to manipulate the geometry of the target, specifically its lateral size, morphology, and the distribution of the tin material, leading to a more suitable target to couple with the main pulse for EUV generation.

The geometry of the target following the prepulse impact is highly conditioned by laser parameters such as the laser intensity and temporal and spatial profiles. When a microdroplet is irradiated with a nanosecond-long prepulse, a plasma cloud will form on the surface of the droplet facing the incident beam. This rapidly expanding plasma cloud in turn exerts an instantaneous recoil pressure with a magnitude of ~100 kbar on the droplet surface, leading to a radial expansion of the spherical droplet into a *pizza*-shaped geometry. The subsequent target comprises a thin, axisymmetric sheet with a thickness of several tens of nanometers, and a micrometer-thick rim that bounds the edge of the sheet [13–17]. The prompt radial expansion (at a speed of order 100 m/s) leads to a target diameter of several hundreds of micrometers on a timescale of a few microseconds, matching the beam size of the main pulse. The radial expansion is initiated by the plasma-induced-acceleration of the droplet to a center-of-mass propulsion speed (of order 100 m/s) along the direction of the laser pulse. The correlation between these two orthogonal speeds, i.e., propulsion vs. expansion
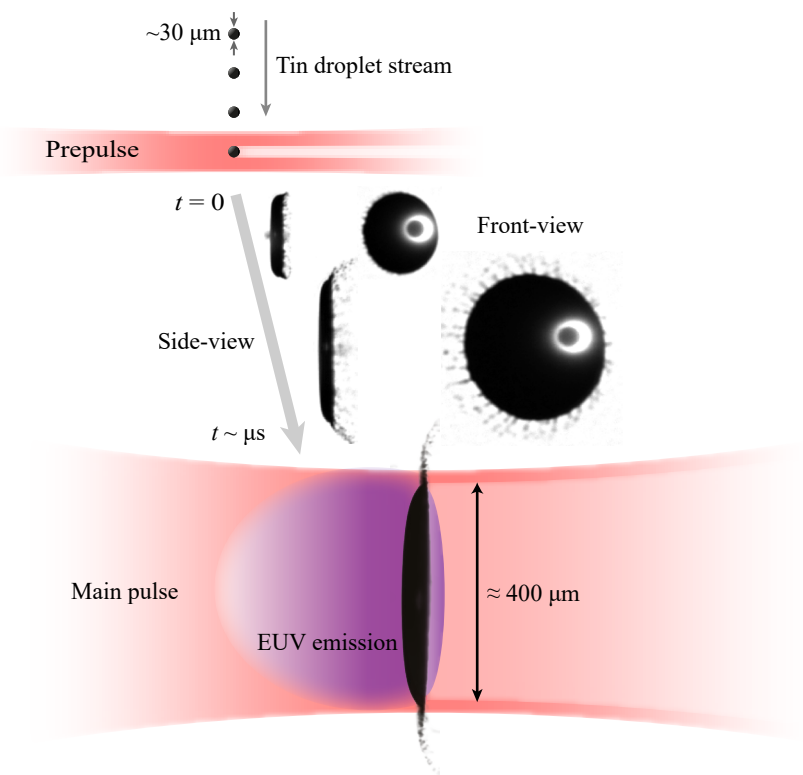
Figure 1.1: Principle scheme of a tin droplet-based LPP EUV source. Liquid tin microdroplets with typical diameters of 30 μm are first irradiated with a prepulse at $t = 0$. For a nanosecond-long prepulse, the droplet will deform into an axisymmetric sheet target, as shown by both the side- and front-view shadowgraphy images taken in the experiments. After a few microseconds, the expanding sheet reaches a desired diameter of typically several hundred micrometers. The target is then irradiated with a more powerful laser pulse, i.e., the main pulse, to produce a hot and dense plasma. EUV light will be emitted from this plasma and will be redirected by a collector mirror (not shown in the figure) to the scanner.

speed, is important not only for shaping and placement of the target, but also for the (energy-)efficiency and stability of the target-formation process. At the microsecond-timescale, it is the hydrodynamic motion of the liquid tin that drives the redistribution of material and the formation of the target morphology that eventually interacts with the main pulse. As is clear from Fig. 1.1, the target formation process also leads to the ejection of liquid tin microparticulate debris. Controlling such debris is a crucial aspect in designing a prepulse strategy [18, 19]. The fast-moving debris may carry a considerable amount of tin, cutting down the useful material that contributes to

the later interaction with the main pulse, and contaminating the nearby collector mirror. Therefore, descriptions of the speed, size, and instantaneous position of these fragments are relevant for the lifetime of current and future EUV lithography sources.

1.1.2   Phenomenology of droplet impact

To better understand the underlying fluid dynamics that governs the reshaping of the droplet by the prepulse laser, we refer to the ubiquitous cases of droplet impact on solid substrates. Here, the phenomena of thinning, expansion, retraction, and fragmentation of a liquid sheet are characterized by the interplay of surface tension, capillary instabilities, inertial force, and other relevant parameters of the fluid system [20–27]. These impact dynamics upon solids have been extensively studied, giving fruitful results which provide inspiration for our research. Prior works from, e.g., Klein *et al.* [17, 28, 29], Gelderblom *et al.* [14], Kurilovich *et al.* [13, 30], Hudgins *et al.* [31] indicate that the fluid-dynamic response of laser-impacted droplets is similar to that of droplets impacting solids. This observation is surprising, especially given the significantly different lengths and timescales typically involved, and the fundamentally different build-up mechanism of the pressure that sets the motion of the liquid.

Figures 1.2(a) and 1.2(b) show a water droplet falling on a pillar [20], and a front-view picture of a liquid tin sheet produced from laser-pulse impact on a microdroplet captured by our experiments, respectively. It is readily observed that in both cases, droplets expand into an axisymmetric *sheet*, accompanied by a myriad of fine *fragments* (debris) that break from the 'fingers', or *ligaments* extruding radially outward from the edge of the sheet. Comparing Figs. 1.2(a) and 1.2(b) also motivates us to speculate on the presence of certain characteristics that cannot first be visualized directly for a metallic liquid sheet. For example, taking advantage of the transparency of liquid water, Fig. 1.2(a) indicates the existence of a bounding rim at the edge of the sheet, which inspires us to postulate the presence of a bounding *rim* also for the liquid tin sheet shown in Fig. 1.2(b). Our subsequent experiments, shown in Figs. 1.2(c.1) and 1.2(c.2), do indeed indicate the presence of this rim.

Although Figs. 1.2(a) and 1.2(b) demonstrate a qualitative agreement between liquid droplets impact upon solids and laser-pulse impact, the fundamental difference in the driving mechanism for the droplet deformation demands a detailed quantitative description of the characteristics of the target morphology. For the canonical case of a droplet falling on solids, the impactor (i.e., a solid substrate or a pillar) remains stationary, constantly transferring the vertical momentum to horizontal momentum [20] along the sheet expansion. Moreover, the droplet deformation is subject to the development of a viscous boundary layer in the vicinity of the contact liquid between
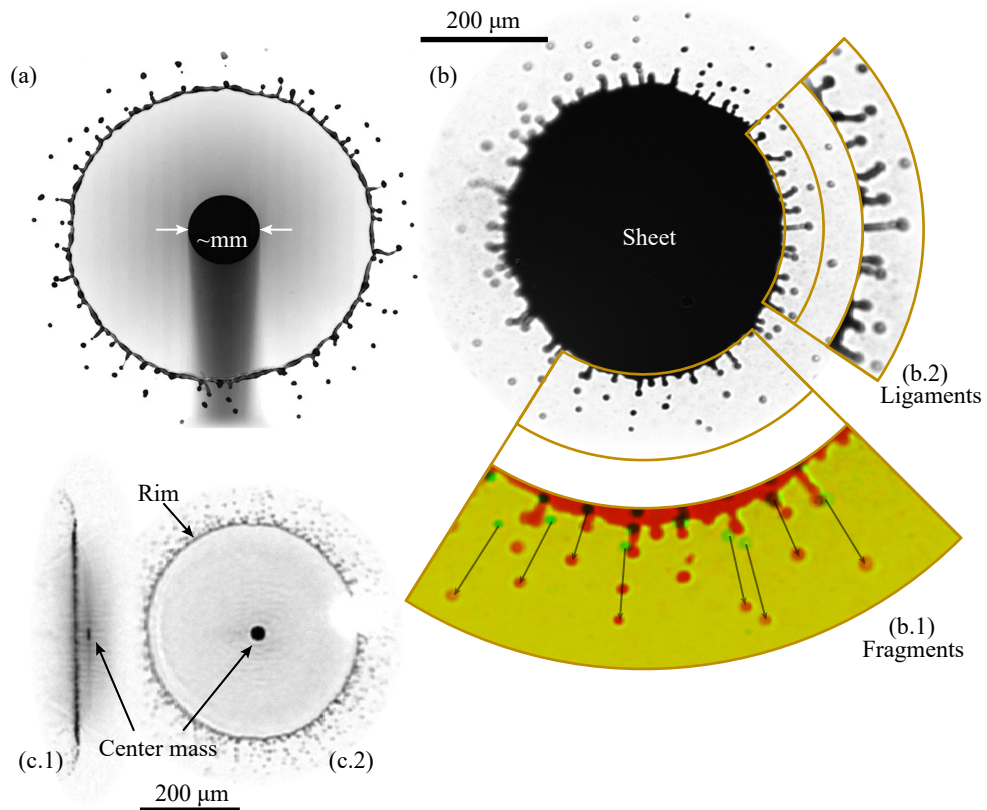
Figure 1.2: (a) A picture showing a millimeter-sized water droplet falling on a pillar of similar size, taken from Wang *et al.* [20]. (b) A front-view shadowgraphy image showing a typical expanding sheet following impact of a ~ 10 ns laser pulse on a droplet with an initial diameter of 67 μm. The laser beam is focused to a size of 110 μm at the position of the droplet and has a pulse energy of 20 mJ. Insets (b.1, b.2) provide a zoomed-in view of fragments and ligaments, respectively. Using a double-frame camera, in (b.1) we present two consecutive images of the same sheet. Pixels in black indicate overlap regions where tin is present in both frames. Yellow pixels indicate the background in the absence of tin. Green and red pixels indicate the presence of tin only in first and second frames, respectively. Arrows that connect the corresponding fragments in the first and second frames show the ballistic trajectory of those fragments. (c.1)(c.2) Side- and front-view shadowgraphy images of a liquid tin sheet (from irradiation by a nanosecond pulse) after being irradiated with a 50-ns-length vaporization pulse (for details see Chapter 3). The vaporization pulse removes the liquid from the thin sheet, leaving relatively thicker features including the bounding rim and the center mass behind.
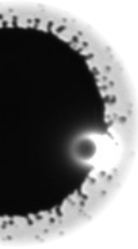
the impactor and the sheet [25, 32–35]. In the case of droplet irradiated by a laser pulse, the recoil pressure from the plasma, which exhibits a highly complex temporal and spatial profile, effectively gives an instantaneous kick to the droplet. This pressure impulse establishes an initial velocity field in the liquid in both the radial and propulsion directions on a nanosecond timescale (following the timescale of the laser pulse) which precedes any appreciable deformation of the droplet from the initial spherical shape [14, 28]. After the laser pulse ends, the magnitude of the pressure field drastically decreases and thus no longer contributes to the deformation and propulsion of the droplet. Furthermore, compared to the impact upon solids, the absence of a rigid solid in the laser impact suggests different boundary conditions for the droplet deformation, which could further influence features of the sheet including the thickness profile, the fragment speed, and the distribution of the liquid at the center of the sheet. One of the distinctive features in the laser impact that could reflect the difference between the plasma- and solid-driven expansion of a droplet is the presence of a *center mass* — a disk-shaped liquid residing in the center of the sheet, see Figs. 1.2(c.1) and 1.2(c.2).

1.2   Thesis outline and summary

Figure 1.2 indicates several main features of the target morphology: *sheet*, *rim*, *ligaments*, *fragments*, and *center mass*. Motivated by our observations of these features, this thesis aims to address the following questions which naturally arise when discussing the target preparation by the prepulse laser:

(i) *How is the liquid tin spatially and temporally distributed among these various components ?*
Answering this question may benefit the efficient utilization of tin mass by the main pulse. Insights generated in this direction would also be particularly valuable for a multi-prepulse scheme for target preparation.
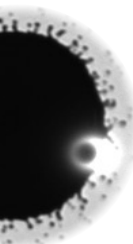
(ii) *What velocities are attained by those microparticulate fragments and how much mass do they carry ?*
Answering this question could assist with the optimal design of mitigation strategies aimed at preventing the aforementioned collector mirror from being contaminated by debris shed from the target.

In this thesis, we experimentally study the interaction of liquid tin microdroplets with a nanosecond-long Nd:YAG laser pulse. Our study focuses mainly on the underlying fluid dynamics that drives the thinning, fragmentation, and mass redistribution of the liquid target. The experiments reported in this thesis have been performed using a pre-existing experimental apparatus including a droplet-generating system, vacuum systems, shadowgraphy setups, and triggering systems as presented by Dmitry Kurilovich [36], and advanced laser systems as presented by Randy Meijer [37]. Compared to these previous studies, in this thesis the experimental setup has an improved shadowgraphy imaging resolution, and a double-frame camera system which effectively enables true time-resolution (compared to the previous stroboscopic imaging system). The details of our upgraded setup will be mainly discussed in Chapter 5.

In **Chapter 2**, we experimentally obtain the thickness of a target sheet by two independent methods from which we derive the mass content on the sheet. The results from both methods are in excellent agreement with each other and reveal a thickness of just several tens of nanometers for the sheet. We find a self-similar behavior of the thinning process, and we generalize the thickness profile in a model which allows a prediction of the thickness for a broad range of experimental conditions beyond those used in this Chapter. From the sheet thickness, we obtain the amount of liquid on the sheet. Our results indicate that more than half of the liquid is lost from the sheet to other channels a few microseconds after the laser pulse — a timescale relevant for lithography application. Furthermore, our results show that for a fixed droplet size, the loss of tin from the sheet is solely determined by time and is independent of the laser energy. A direct conclusion from this finding is that, in order to maximize amount of tin on the sheet, it is optimal that the second, successive laser follows the prepulse with the smallest possible time delay. To ensure that the tin target reaches a sufficient size in this short time, an energetic prepulse is needed to achieve a higher expansion rate of the droplet.

To verify the conclusion obtained in Chapter 2, it is necessary to determine the sheet thickness at earlier times than those studied during the sheet expansion. Motivated by this, in **Chapter 3**, we study the thickness and mass content of the sheet by irradiating it with a probe *vaporization pulse*. This probe laser pulse gradually removes liquid from the sheet, allowing us to access the sheet thickness profile at early times. The thickness profile, and from it the mass content on the sheet obtained by this vaporization pulse, agree well with the prediction from the model discussed in Chapter 2. Furthermore, with increasing time, the vaporization pulse will first remove the thin sheet, leaving features with larger thicknesses behind. In this way, we directly visualize the presence of the bounding rim and the center mass. Our results reaffirm our proposal to use a

more energetic prepulse and an earlier impact time for the main pulse, which should lead to a larger amount of tin contained in the sheet.

In **Chapter 4**, we study the partitioning of the kinetic energy that is channeled into the radial deformation and propulsion along the laser direction. Based on both an extensive set of experimental results and radiation-hydrodynamic simulations performed using the RALEF-2D code, we investigate the effects of varying droplet diameter, beam size, and pulse energy on the energy partitioning as well as the ratio of characteristic speeds associated with these two orthogonal motions. The simulation results are found to be in good agreement with the experiments. Furthermore, we find that the kinetic partitioning is solely determined by the width of the (Gaussian) pressure impulse resulting from the plasma at the droplet surface. This finding is consistent with the analytical description provided by Gelderblom *et al.* [14], supporting the ordering of characteristic timescales that separate the generation of the instantaneous plasma impulse from the early hydrodynamic deformation that can be well described by incompressible flow.

In **Chapter 5**, we experimentally measure the speed of the fragments generated by ligament breakup, and the temporal evolution of this speed throughout the sheet expansion process. Using a double-frame camera and a trigger system configured to provide dual backlighting, our imaging setup is capable of capturing the trajectory of each individual fragment. The speed of these fragments is obtained from these trajectories. We find that the upper bound of the fragment speed is the initial expansion speed of the sheet. Further analysis reveals a self-similar curve that characterizes the temporal evolution of the fragment speed. The robustness of this self-similar behavior is demonstrated by the extensive range of droplet sizes and pulse energies investigated in our experiments. We further explore the underlying physics of the observed self-similarity. Our results provide a powerful tool for predicting the instantaneous location and velocity of the fragments. This tool may be valuable in designing effective mitigation strategies against contamination by fragment debris in EUV sources.

With all the measurements performed and quantities provided by the previous Chapters, we finally discuss the global mass distribution among the target in **Chapter 6**. First, by combining the improved spatial resolution offered by our imaging system with machine learning capabilities, we are able to determine the diameter of each fragment. With the time-resolved capability provided by the double-frame camera (see Chapter 5), we obtain the instantaneous fragment diameters at the moment when they detach from the ligaments. These results, along with the tracking of the fragment number, provide the mass accumulated in fragments over time. Next, we determine the non-negligible amount of liquid contained by the ligaments and the rim by combining our experimental observations with an analytical model developed by Wang *et al.* [22].
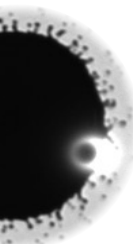
We also discuss the amount of liquid tin in the center mass. Finally, we provide a global map of the mass distribution among these aforementioned channels: sheet, rim, fragments, ligaments, and the center mass. The sum of the liquid in these channels is shown to account for $\approx 90\,\%$ of the total mass of the initial droplet. The still-missing fraction of mass is consistent with the mass fraction ablated by the laser pulse as indicated by our radiation-hydrodynamics simulations.

In summary, this thesis details the morphology of a liquid tin target induced by nanosecond-long laser-pulse impact on a liquid tin microdroplet, covering the early-time momentum kick and the related kinetic energy partitioning that set the subsequent target thinning, to the late-time fragmentation process that produces debris. The knowledge gained from our studies could play a crucial role in optimizing EUV generation with regard to a greater utilization of tin by the main pulse or a second prepulse in the context of a multi-prepulse scheme, and improved mitigation strategies against contamination from debris that may limit optics lifetime.

1.3 Outlook

One of the major advances made in this thesis is the identification and understanding of the microscopic structures of tin targets used in nanolithography. Even though significant progress has been made towards understanding the full mass distribution, several open questions have been brought to light by the studies presented in this thesis. One such example is the physics that governs the formation of the center mass. In this thesis, we hypothesize that the presence of the center mass is related to the influence of compressible flow, even though its influence on the overall droplet deformation is found to be minor (see Chapter 6). The relation between the center mass and the compressibility of the fluid could be explored by using laser systems with different temporal shapes. This temporal shape has recently been shown by Meijer *et al.* [38] to greatly affect the extent of the fluid's compressibility.

In this thesis, the thickness of the rim is analytically determined by invoking the model of Wang *et al.* [22]. A direct experimental quantification of the rim thickness, however, is challenging due to the resolution limit of our imaging system and the effects of the vapor generated as part of our efforts to visualize the rim (Chapter 3). To determine the rim thickness, future research may employ methods beyond direct optical inspection and to focus on phenomena that are driven by the evolution of the rim's thickness, such as size-dependent laser ablation threshold and the onset of plasma formation [37].

In our experiments, the lifetime of ligaments from early destabilization to later, semi-disordered growth of their length is visualized and quantified in detail (Chapter 5 and Chapter 6). Compared to the case of solid-impacted droplet, the formation of ligaments in our experiments exhibits a fundamental difference regarding their attainable length and breakup modes. These differences may propagate to the size and velocity distribution of fragment debris, where discrepancies with the available literature have been observed (see Chapter 5). To fully understand the origin of these discrepancies, experimental studies that incorporate the continuous time evolution of individual ligaments are required. Such dynamics could be explored experimentally, for example, by using cameras with multiple short exposure windows.

In the context of industry application, research on target preparation using a multi-prepulse scheme has shown promise [11, 12]. One such *advanced* target preparation scheme includes a second prepulse which vaporizes the sheet target (much like our studies in Chapter 3). Our results pave the way for the development of such strategies, providing a detailed understanding of the local thickness conditions and the material distribution on the sheet. However, the spatial distribution of tin material in this advanced target is currently unclear. Moreover, its phase upon vaporization, be it liquid, gaseous, or plasma, is not yet known. Given the highly practical relevance of this additional shaping of the target, experimental efforts and analytical modeling of the interaction between the second prepulse and the prior, nanosecond-laser-induced sheet is an important topic for future work.

CHAPTER 2
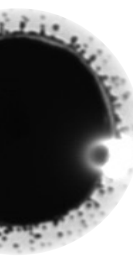
MASS LOSS FROM A STRETCHING SEMITRANSPARENT SHEET OF LIQUID TIN

Bo Liu, Dmitry Kurilovich, Hanneke Gelderblom, and Oscar O. Versolato

We experimentally study the morphology of a radially expanding sheet of liquid tin, formed by nanosecond-pulse Nd:YAG laser impact on a spherical microdroplet. Specifically, the sheet thickness profile and its time evolution are captured in detail over a range of laser-pulse energies and for two droplet sizes. Two complementary methods to determine this thickness are employed and shown to be in excellent agreement. All obtained thickness profiles collapse onto a single self-similar curve. Spatial integration of the thickness profiles allows us to determine the volume of the sheet. Remarkably, less than half of the initial amount of tin remains in the sheet under conditions relevant for industrial sources of extreme ultraviolet light, where these thin tin sheets serve as target material. Further analysis shows that the dominant fraction of the mass lost from the sheet during its expansion ends up as fine fragments. We propose that such mass loss can be minimized by producing the sheet targets on the shortest possible time scale. These findings may be particularly valuable for ongoing developments in state-of-the-art nanolithography.

2.1   Introduction

Tin microdroplets serve as mass-limited targets for high-energy lasers to produce a hot and dense plasma that emits extreme ultraviolet (EUV) light for state-of-the-art nanolithography [11, 12, 39–43]. The generation of EUV light is a two-step process, in which a first laser prepulse deforms the tin droplet into a liquid sheet that is suited to serving as a target for a second, more energetic main laser pulse that produces the EUV light. A detailed understanding of the prepulse-induced deformation is required to optimally produce EUV light with a minimal production of microparticulate "debris". Such debris could limit the lifetime of nearby light-collection optics [12, 31, 42–44]. Several recent studies have provided insight into the response of a tin microdroplet to a nanosecond laser pulse in which the propulsion [13, 30] accompanies a deformation [13, 14, 28, 30, 45] of the droplet into a thin sheet. The eventual break-up and fragmentation of the sheet into much smaller droplets has also been studied [17, 31]. The thickness evolution of expanding sheets formed by the impact of millimeter-sized water drops onto a pillar has been investigated in Refs. [20, 46]. Droplet deformation and fragmentation upon impact, be it onto a solid substrate or by a laser pulse, is a topic of particular current interest in fields ranging from epidemiology, governing the transport of pathogens from sneezes and coughs [20, 22], through sprays relevant in, e.g., agriculture [22, 47], to state-of-the-art nanolithography [13, 14, 28, 30, 43, 45]. Knowledge of the thickness profile of the thin liquid sheet formed upon impact is crucial for understanding the deformation and complex fragmentation processes involved. However, to date no experimental data are available on the thickness profile of the stretching nanometric liquid metal sheet formed after laser impact. Several theoretical models have been suggested [14, 20, 24] and applied to tin microdroplets [17] but it has not yet been possible to draw any clear conclusions regarding the thickness profile. Obtaining such information would enable us to estimate how much tin mass is actually retained in the expanding target sheet when it is hit by the main laser pulse in plasma sources of EUV light.

In this work, two complementary methods for determining the sheet thickness profile of laser-impacted tin microdroplets are introduced, compared, and applied under industrially relevant conditions. First, the finite transmissivity of the several-tens-of-nanometers-thick stretched liquid-metal sheet is recorded. As the optical constants of tin are well known [48] the transmissivity can be converted to a local thickness $h(r)$ as a function of the radial coordinate r, assuming cylindrical symmetry. Second, the Taylor-Culick opening speeds [49] of spontaneously formed holes in the stretching sheet are experimentally measured, which again allows to obtain $h(r)$. Next, we employ an existing self-similar model [20] of the sheet-thickness evolution and

find good agreement between this model and our experiments. Finally, we use the measurement data to determine the fraction of the volume — or, equivalently, mass — that is retained in the target at times relevant for main laser-pulse impact. Channels for mass loss from the sheet are subsequently identified and quantified using existing models [22, 24].

2.2 Experiments and methods

Our experimental setup is described in detail in Ref. [13]. The most important aspects and relevant upgrades are discussed here. A tin reservoir is situated on top of a vacuum chamber (10^{-7} mbar) and is kept at a constant temperature of 260 °C. From the reservoir, a nozzle produces a multikilohertz droplet train of 99.995% purity tin (with liquid density $\rho = 7.0$ g/cm^3 and surface tension $\sigma = 0.54$ N/m) that goes through the center of the chamber. The microdroplets relax to a spherical shape with a diameter set to be either $D_0 = 32$ or 26 μm before passing through a horizontal light sheet produced from a helium-neon laser. The resulting scattered light is detected by a photomultiplier tube, the signal from which is frequency down-converted to 10 Hz to enable triggering of the Nd:YAG laser system. This laser system produces pulses at a wavelength of 1064 nm and for a time duration of 10 ns at full width at half maximum (FWHM). The beam is focused to a Gaussian spot (105 μm FWHM) onto the droplets in the center of the chamber. By using a half-wave plate and a thin-film polarizer, the beam energy can be adjusted without affecting the spatial beam profile. To maintain cylindrical symmetry the laser light entering the chamber has circular polarization, produced by employing a quarter-wave plate. The dynamics of the expanding droplets are captured by stroboscopic shadowgraphy imaging systems [13, 30, 50]. These systems are based on two broadband 560 nm wavelength (with a 12 nm FWHM bandwidth) 5-ns-long light pulses combined with three long-distance microscopes coupled with CCD cameras. The dye lasers provide backlighting that is rendered both temporally and spatially incoherent to avoid imaging artifacts. The spatial resolution of the imaging systems is approximately 5 μm. Two microscopes are aligned $\pm30°$ to the Nd:YAG laser beam propagation direction, giving two slightly tilted front-view images. A third microscope is aligned orthogonally to the Nd:YAG laser beam to provide side-view images. The microscopes are equipped with band-pass filters to suppress light emitted by the plasma induced by the laser-pulse ablation. The trigger signals for the two dye lasers are separately produced from two tunable delay generators, which enables us to adjust the time interval between images captured by the two $\pm30°$ microscopes.

$t = 3.4$ µs

(a1.1)   (a1.2)   (a1.3)

$t = 4$ µs

(a2.1)   (a2.2)   (a2.3)

$t = 4.4$ µs

(a3.1)   (a3.2)   (a3.3)

$t = 4.8$ µs   (b3) $t = 4.8$ µs + 150 ns

(b1)   (b2)

200 µm
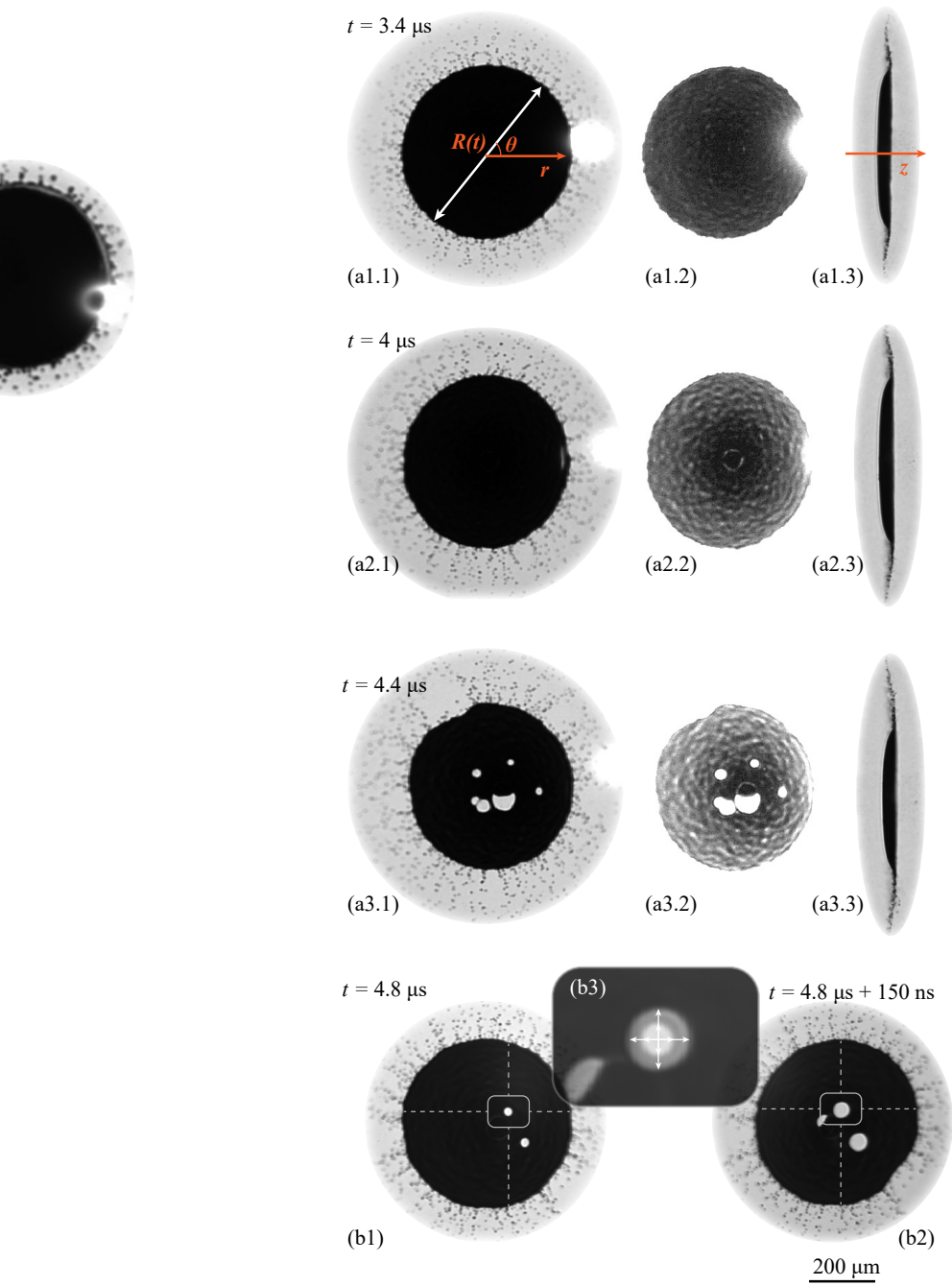
(Caption see next page)

Figure 2.1: (Previous page) Shadowgraph images of expanding sheets from tin microdroplets ($D_0 = 32\,\mu$m) hit by a nanosecond laser pulse with total energy $E = 55$ mJ. The droplet accelerates to a velocity $U = 160$ m/s (We $= 5\,400$). (a1.1),(a2.1),(a3.1) Front views of liquid sheets at time delay t (laser impacts at $t = 0$). The images are stretched along the horizontal axis to correct for the 30° observation angle. The bright spots in the images are from plasma emission. (a1.2),(a2.2),(a3.2) The same images with a digitally modified contrast. (a1.3),(a2.3),(a3.3) Corresponding side-view images indicate a weak curvature (laser impacts from the left, propelling the droplet to the right). In (a1.1) and (a1.3), the cylindrical coordinate system (r, θ, z) with its origin at the center of the sheet is depicted. At later times, holes appear cf. (a3), (b1), and (b2). The overlay of a hole (see the main text) is highlighted by a white box in both (b1) and (b2). The arrows in inset (b3) indicate the receding edge of the hole.

2.2.1 Sheet thickness from transparency measurement

Figure 2.1 presents typical shadowgraph images. The impact of the laser pulse accelerates the droplet to a center-of-mass speed U of order 100 m/s, and radially deforms it into a thin sheet with a radius $R(t)$ of order 100 μm on a time scale of several microseconds. The sheet expansion is axisymmetric, enabling its description in cylindrical coordinates (r, θ, z). Figures 2.1(a1.1), 2.1(a2.1), and 2.1(a3.1) further show many small fragments created by the destabilization of ligaments that have formed on the edge of the sheet. These ligaments and small droplets extend radially outward in the plane of the sheet. Figures 2.1(a1.3), 2.1(a2.3), and 2.1(a3.3) show corresponding side view shadowgraph images. These images indicate the presence of a weak curvature of the otherwise smooth liquid sheet that is thus seen to resemble an inverted umbrella. This curvature precludes obtaining the thickness directly from the side views. The curvature, typically with an angle $<2°$ over the majority of the sheet, increases near the peripheral edge to $<30°$. Similar to Ref. [46], we employ an optical method based on the transmission of light through the sheet to determine the sheet thickness. In our method, however, we probe much thinner sheets. The highly stretched sheet is partially transparent to the backlighting as is shown with a digitally enhanced contrast in Figs. 2.1(a1.2), 2.1(a2.2), and 2.1(a3.2). For a sheet of material with thickness h_m and complex refractive index n_m, the transmission $T(h_m)$ of a beam through the sheet as a function of thickness is given by [51]

$$T(h_m) = \frac{[(1 - \mathcal{R})^2 + 4\mathcal{R}\sin^2\delta]e^{-2\beta h_m}}{(1 - e^{-2\beta h_m}\mathcal{R})^2 + 4e^{-2\beta h_m}\mathcal{R}\sin^2(\delta + \alpha h_m)}, \tag{2.1}$$

with the reflectance under normal incidence given by $\mathcal{R} = |(n_0 - n_m)/(n_0 + n_m)|^2$, where n_0 presents the vacuum refractive index, i.e., $n_0 = 1$, and $\delta = \arctan[2k_0\beta/(\alpha^2$

+ β^2 - k_0^2)] with k_0 the wavenumber of the incident beam in vacuum. The wavevector inside the material is given by $\alpha = \text{Re}[k_0 n_m]$ and $\beta = \text{Im}[k_0 n_m]$[1]. Taking the 30° front-view angle into account, the actual tin-sheet thickness $h = h_m \cos 30°$. The small incident angle has a negligible influence on the reflectance $\mathcal{R}$.

Equation (2.1) allows us to estimate the tin sheet thickness from the CCD pixel values P_{ij} of the shadowgraph images. The local transmission is given by $T_{ij} = (P_{ij} - P_0)/(P_{b,ij} - P_0)$, where i and j are the pixel indices. Backlighting values $P_{b,ij}$ are obtained from shadowgraphs where no droplets are present in the region of interest. The values for P_{ij}, $P_{b,ij}$, and P_0 are discrete and have a limited, 8-bit dynamic range. Therefore, averaging over sufficient (typically 20) images is required to obtain an accurate mean value to represent the actual smooth transmission profile. Parameter P_0 characterizes a common background offset value that could originate from, e.g., dark noise or imaging glare. This parameter is experimentally established using thick fully opaque tin sheets in an early stage of deformation or particularly thick features within the sheets. The values of P_0 depend on the intensity of the backlighting, the particulars of the optical alignment, and the intensity of the plasma emission. These influences are taken into account by individually assessing P_0 for each shadowgraph image. We apply the transparency method for sheets with $h \lesssim 50\,\text{nm}$ and obtain spatial thickness profiles $h(r)$ spanning the full range $0 \leq r \leq R(t)$.

2.2.2   Sheet thickness from hole opening speed

In Figs. 2.1(a1.2), 2.1(a2.2), and 2.1(a3.2), we observe ripples. These ripples are the signature of a fluid-dynamic instability that will eventually puncture the sheet and cause the formation of holes [17, 52]. On uniform sheets these holes open at a constant Taylor-Culick (TC) speed [49],

$$u_{tc} = \sqrt{\frac{2\sigma}{\rho h}}, \qquad (2.2)$$

which expresses a balance between surface tension and inertia. After aligning the corresponding oblique ($\pm 30°$) front-view images with the centers of each pair of holes, we determine the distance traveled by the hole boundary [see Fig. 2.1(b3)]. From these distances and the time interval between the two images, we obtain the local TC speed and from Eq. (2.2) the local sheet thickness. Figures 2.1(b1), 2.1(b2), and 2.1(b3) show typical examples of the results of such alignment for a hole. First, an expanding sheet is captured by one camera at $t = 4.8\,\mu\text{s}$ [see Fig. 2.1(b1)]. Then, 150 ns later,

---

[1]The optical constants of liquid tin at 260°, with incident light wavelength at 560 nm (2.2 eV) in vacuum, are $\text{Re}[n_m] = 1.61$ and $\text{Im}[n_m] = 5.57$ [48].

the same target is recorded by the other front-view camera [see Fig. 2.1(b2)]. We align Figs. 2.1(b1) and 2.1(b2) with the center of this hole in Fig. 2.1(b3), where the two images are overlaid as visualized using different gray-scale values. We clearly observe the increase in the size of the hole with time. The distance traveled by the hole boundary is determined by tracing four points defined by the intersection of an orthogonal cross with the boundary. The local thickness is obtained for each point individually; the radial coordinate is provided by a correction procedure that takes into account the finite curvature close to the edge of the sheets (cf. the side views in Fig 2.1), which causes an apparent horizontal shift in the position of the hole in the two front-view shadowgraphs. With holes appearing nearly randomly over the sheet surface, an almost complete thickness profile $h(r)$ can be constructed by processing sufficient stroboscopic images taken at the same time delay. Holes appearing near the edge of the sheet cannot be used in the TC method due to significant nonuniformity of the local thickness profile [17]. In addition, the edge curvature distorts the hole overlay close to the sheet circumference. The TC method is only applicable within approximately $1\,\mu$s after the onset of hole formation τ^*. At later times many holes quickly appear and obstruct the analysis. Time τ^* has previously been observed to decrease with the Weber number $\mathrm{We} = \rho R_0 U^2/\sigma$ as $\tau^*/\tau_c \sim \mathrm{We}^{-1}$ [17]. Thus, with increasing Weber number the thickness is probed by the TC method at earlier times. Here, the Weber number is defined with the initial droplet radius $R_0 = D_0/2$ and the center-of-mass speed U. With the laser-pulse energy ranging from 40 to 200 mJ, U ranges from 100 to 300 m/s, yielding $\mathrm{We} = 2\,000$-$20\,000$ (see the Appendix). The capillary times characterizing the capillary sheet retraction $\tau_c = [\rho R_0^3/\sigma]^{1/2}$ are $\tau_c = 7.3$ and $5.3\,\mu$s for droplet sizes $D_0 = 32$ and 26 μm, respectively.

2.3 Results

2.3.1 Thickness profile

Figure 2.2 presents a selection of the measurement results for the sheet thickness obtained from the two methods: (a) transmission (with droplet sizes $D_0 = 32$, 26 μm) and (b) TC speed (with $D_0 = 32\,\mu$m). A comparison of the two methods in the parameter range in which both methods are applicable is presented in Fig. 2.2(c). Figure 2.2(a) shows that after impact from a laser pulse, the droplet deforms into a sheet with a thickness of several tens of nanometers. The profiles have a slender spatial gradient where h decreases with r. The thickness h generally decreases with time, as becomes clear comparing the 55-mJ pulse cases at different time delays. These features are consistent with the TC results presented in Fig. 2.2(b) where the reduction
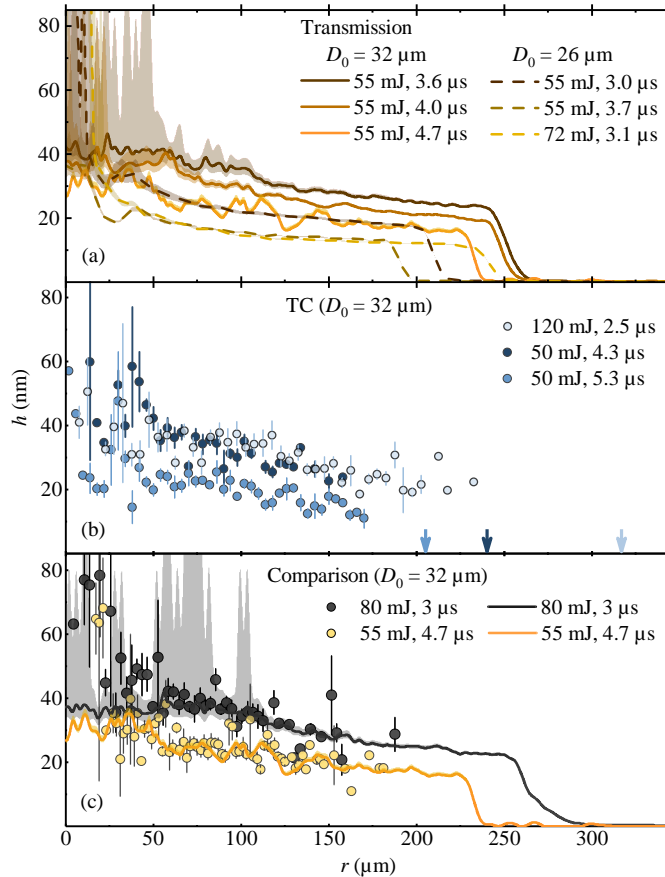
Figure 2.2: The sheet thickness as a function of the radial coordinate. (a) Results from the transmission method. Data from $D_0 = 32$ and 26 μm droplets are depicted by solid and dashed lines, respectively. The shaded areas following the data curves indicate the typical systematic uncertainties obtained by varying $P_0 \pm 3\%$. (b) Results from the TC method with $D_0 = 32\,\mu$m. Arrows positioned on the x axis represent the sheet radius. The uncertainty error bars are based on the standard deviation of binned data. (c) A comparison of the two methods.

of the thickness with time is seen by comparing the two 50-mJ cases. Laser pulses with higher energies deform the droplet faster: to thin the droplet to the observed thickness, it takes 4.3 μs for 50-mJ laser pulse, while a shorter time of 2.5 μs is required to reach a similar thickness for a more energetic pulse of 120 mJ. All cases shown present a profile that, with time, decreases both in thickness and in radial dimension. The reduction of the sheet radius occurs on the time scale of capillary retraction of the

sheet [24]. Figure 2.2(a) also shows the data from the smaller droplet size $D_0 = 26\ \mu$m, demonstrating that the thickness evolution is consistent with that of the larger droplet: h reduces both in t and r, and decreases faster with more energetic laser pulses.

The comparison of the two methods presented in Fig. 2.2(c) shows excellent agreement. This agreement validates our two methods of measurement. Some discrepancies appear in a small region of size approximately R_0 close to the origin, where both the transmission and the TC methods hint at the presence of a thicker feature. Visual inspection of Figs. 2.1(a2.2) and 2.1(a3.2) confirms the presence of such thick, disk-like features near the center of the sheet bounded by a much thinner halo. The stochastic nature of this feature leads to a locally increased standard deviation error on the binned data, e.g., as shown in Fig. 2.2. These features may be caused by jetting and bursting, phenomena that could originate from laser-induced cavitation inside the liquid [17, 45, 50]. The amount of mass contained in these features is expected to be small [17].

The dominant fraction of the data presented in Fig. 2.2 shows smooth thickness profiles $h(r,t)$ that decrease with both time and the radial coordinate. Under all experimental conditions and over all time ranges studied, we observe that the sheet profiles share remarkably similar shapes.

2.3.2 Model of the self-similar thickness profile

Following the work by Wang *et al.* [20] for sheet expansion upon droplet impact on a pillar, we use a self-similar solution to describe the sheet-thickness evolution. In this slender-slope model, the flow $u_r(r,t)$ in the expanding sheet is assumed to be radially outward. Furthermore, the flow is considered to be inviscid (the Reynolds number is of order 10^3) and curvature-induced radial pressure gradients are neglected. The flow in the sheet is then given by the axisymmetric Euler equation

$$\frac{\partial u_r}{\partial t} + u_r \frac{\partial u_r}{\partial r} = 0. \tag{2.3}$$

Equation (2.3) suggests that a flow field $u_r(r,t) = r/t$ is established on the time scale of sheet expansion, i.e., at times $t > D_0/U \sim 100$ ns. Completing Eq. (2.3) by the mass conservation equation for an axisymmetric sheet, one finds the (nondimensionalized) governing equation for the sheet expansion [20]

$$t^\star \frac{\partial h^\star}{\partial t^\star} + r^\star \frac{\partial h^\star}{\partial r^\star} + 2h^\star = 0, \tag{2.4}$$
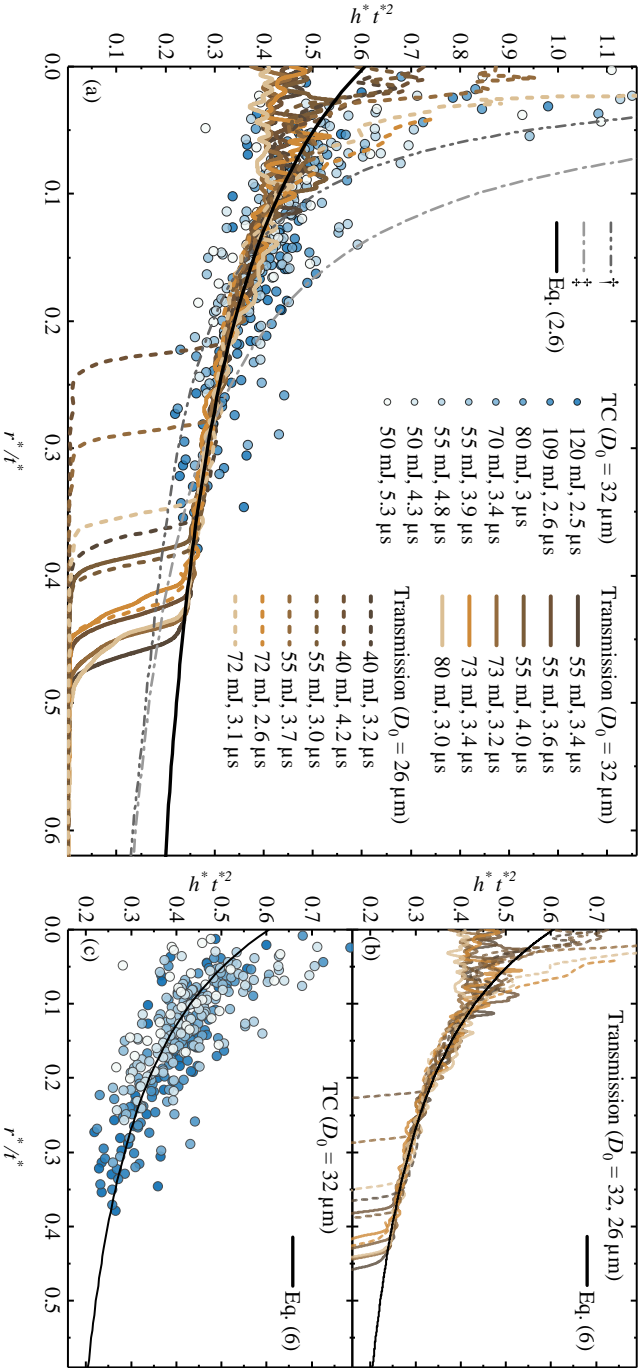
Figure 2.3: (a) The sheet-thickness data represented in terms of the similarity variables $r^\star/t^\star$ and $h^\star t^{\star 2}$ (see the main text). The transmission data from $D_0 = 32$ and $26\,\mu m$ are depicted by colored solid and dashed lines, respectively; TC data from $D_0 = 32\,\mu m$ are represented by scatter points. The corresponding pulse energy and time delay are indicated in the legend. The fit result of Eq. (2.6) to the full concatenated data range is depicted by a black solid line. Other models from Ref. [24]($\ddagger$) and Ref. [20]($\dagger$) are also shown, see legend. (b) A plot of the transmission data only. (c) A plot of the TC data only.

where $r^\star = r/D_0$, $h^\star = h/D_0$, and $t^\star = Ut/D_0$. The similarity solution to Eq. (2.4) is of the form [20]

$$h^\star t^{\star 2} = f(\frac{r^\star}{t^\star}).$$ (2.5)

Equation (2.5) predicts that all experimental data $h(r, t, U, D_0)$ can be collapsed onto a universal curve given by $y = f(x)$ with similarity variables $x = r^\star/t^\star$, $y = h^\star t^{\star 2}$. Figure 2.3(a) demonstrates the collapse upon rescaling in terms of the similarity variables for the all obtained data — which, for clarity, are subdivided into the transmission-method results in Fig. 2.3(b) and the TC-method results in Fig. 2.3(c). Without exception, all data collapse onto a single master curve.

For the similarity profile f in Eq. (2.5), several theoretical and empirical conjectures have been proposed for droplet impact on a solid [20, 25, 53, 54]. Inspired by Wang *et al.* [20], we formulate $f(x)$ for the tin-sheet expansion upon laser-pulse impact as

$$f(x) = \frac{1}{a_0 + a_1 x + a_2 x^2},$$ (2.6)

with its associated dimensional thickness profile

$$h(r, t, U, D_0) = \frac{D_0^3}{a_0 U^2 t^2 + a_1 U t r + a_2 r^2}.$$ (2.7)

The result of the fit of Eq. (2.6) to the full concatenated data yields $a_0 = 1.65(2)$, $a_1 = 6.9(3)$ and $a_2 = -2.4(8)$ with the number in brackets indicating the one-standard-deviation uncertainty. Data points within the central disk feature (typically of size approximately R_0), as determined by individual inspection of the shadowgram images, are excluded from the fit.

Equations (2.6) and (2.7) are of the same form as the ones in Ref. [20], but differ in the coefficients of the polynomial. Indeed, using the semi-empirical coefficients $a_1 = 23.2$, $a_2 = -38.4$, and a cubic term $a_3 = 34.2$ from Ref. [20], we find an overestimation of the thickness near the center of the sheet, and an underestimation of it closer to the edge, as shown in Fig. 2.3. These discrepancies reflect the different physical origins of the droplet deformation in the two cases: in our experiments it is the laser-produced plasma pressure that causes the deformation of the droplet into a sheet [13, 30, 50], while in the experiments by Ref. [20] it is the impact onto a solid surface. This difference affects the early-time deformation of the droplet; in particular, near the impact center. Therefore, we use an additional term a_0 to account for the different boundary condition at $r = 0$ and obtain different numerical values for a_1, a_2. Furthermore, we remove the cubic term that describes the early-time ($t \ll D_0/U$)

deformation dynamics [20] and does not impact the current late-time sheet expansion.

The collapsed experimental data for our tin droplets are seen to be excellently reproduced by Eq. (2.7). Hence, Eq. (2.7) provides a useful tool for predicting the thickness profile of expanding sheets for all droplet sizes and laser impact parameters at times relevant for nanolithography, i.e. at times $t \gg D_0/U$ when significant target expansion has occurred.

2.3.3   Mass distribution during sheet expansion

As shown in Fig. 2.2, the stretched sheet is several tens of nanometers in thickness. This thickness is a factor one half to one quarter of what one would estimate from global mass conservation by assuming a uniform sheet of thickness $h = 4R_0^3/[3R(t)^2]$. Additionally, at the time scales probed in this study, the thickness and the radius of the sheet decrease simultaneously with time (see Fig. 2.2). These findings suggest that a substantial amount of tin is removed from the sheet during its expansion.

To better understand the temporal and spatial distribution of the tin mass, we again revisit studies of droplet impact on a pillar [20, 22, 24, 46, 53] or on a solid substrate [25, 32]. In these studies, the Weber number $\text{We} = \rho U^2 R_0/\sigma$ is the pertinent parameter to describe the expansion dynamics. To facilitate a direct comparison with that body of available literature, we group our data by the Weber number hereafter, using the drop's center-of-mass speed U (see the Appendix).

A doughnut-shaped rim formed on the bounding edge of the expanding sheet has been universally reported. This rim progressively collects mass, ever increasing its volume V_{rim}. This rim cannot be seen separately in Fig. 2.1 as it has a diameter (see below) well below our resolution limit. It destabilizes due to capillary instabilities and forms ligaments that move radially outward and break into a fine spray of droplets [17, 24] which comprise a volume V_{fragment}. These ligaments and fragment droplets are clearly visible in Fig. 2.1. Thus, in addition to the volume in the sheet V_{sheet}, we ultimately interpret the tin distribution as

$$V_0 = V_{\text{sheet}} + V_{\text{rim}} + V_{\text{fragment}} \tag{2.8}$$

during the sheet expansion, which we will now analyze. In the following, given the constraints on the transmission and TC methods, we consider only the case of mostly intact sheets, i.e., those where no significant hole formation has occurred yet. Further experimental progress towards better visibility of fragment droplets may in the future enable a direct quantification of the fragment volume.
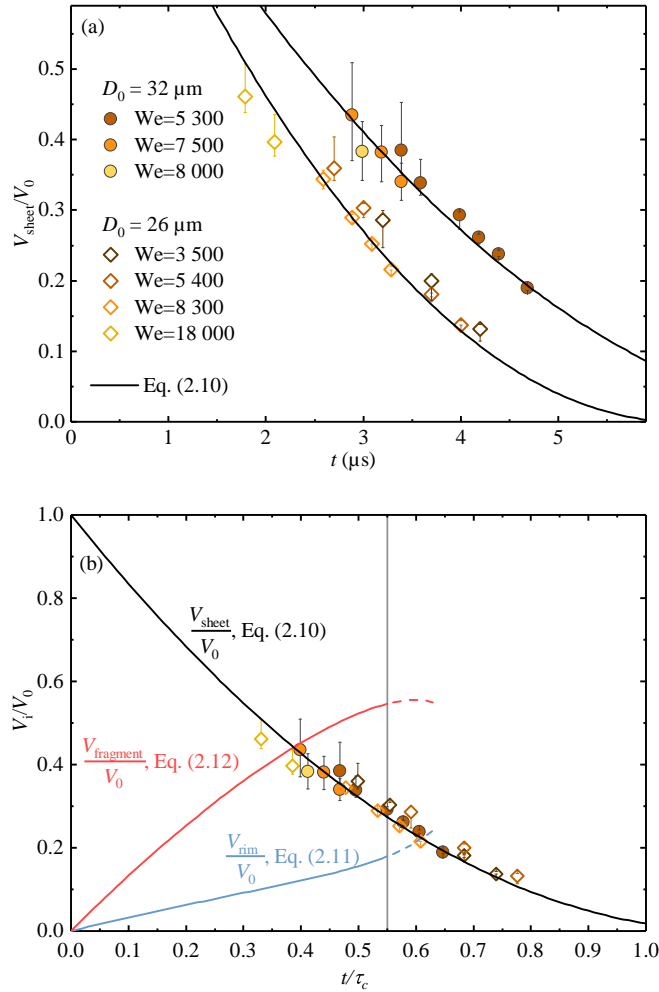
Figure 2.4: (a) The volume ratio of the sheet to that of the initial droplet V_{sheet}/V_0 as a function of time for droplet sizes $D_0 = 32, 26\,\mu$m. The Weber numbers for the various data sets are indicated in the legend. (b) The volume ratios V_i/V_0 as a function of the nondimensional time t/τ_c. Equation (2.10) for V_{sheet}/V_0 is presented by black solid lines in both panels. The volume ratios V_{rim}/V_0 from Eq. (2.11) and $V_{fragment}/V_0$ from Eq. (2.12) are depicted as blue and red lines, respectively. The vertical line marks $t/\tau_c \approx 0.55$ (see the main text).

2.3.3.a   Volume of the sheet

Figure 2.4(a) presents the volume ratio of the sheet to the initial droplet V_{sheet}/V_0 as a function of time with Weber numbers between 3 500 to 18 000. The volume V_{sheet} is obtained by integrating over the transmission data in rings contributing $\delta V_{\text{sheet}} = 2\pi r h\, \delta r$. TC data are not used here as these do not provide a description of $h(r)$ over the full domain of r. Over time, the sheet continuously looses liquid: about $2\,\mu$s after the laser-pulse impact, less than half the initial amount of tin is still in the sheet. For the smaller droplet ($D_0 = 26\,\mu$m) the fraction V_{sheet}/V_0 is smaller than that of the larger ($D_0 = 32\,\mu$m) droplet at equal times.

To derive a theoretical expression for the sheet volume, we require not only an expression for the time-dependent sheet thickness $h(r, t)$ but also for the sheet radius $R(t)$. To this end, we employ the model developed by Villermaux *et al.* [24] for pillar impact, in which the sheet radius is given by

$$\frac{R(t) - R_0}{R_0} = \sqrt{\text{We}}\,\frac{t}{\tau_c}\left(1 - \frac{t}{\tau_c}\frac{\sqrt{3}}{2}\right)^2. \tag{2.9}$$

This expression has previously been found to agree well with tin-droplet expansion after laser-pulse impact [13, 17]. The thickness profile that corresponds to Eq. (2.9) is given by $f(x) = 1/(12\,x)$ in Ref. [24], which is consistent with Eq. (2.6) taking $a_1 = 12$ and $a_0 = a_2 = 0$. This thickness profile is in quite reasonable agreement with our data, given the fact that the model does not contain any free fit parameter (see Fig. 2.3). Using Eq. (2.9) together with this thickness profile, we obtain, for the sheet volume,

$$\frac{V_{\text{sheet}}}{V_0} = \frac{1}{V_0}\int_{R_0}^{R(t)} 2\,\pi\,rh(r,t)dr = \left(1 - \frac{\sqrt{3}}{2}\frac{t}{\tau_c}\right)^2. \tag{2.10}$$

This result shows that the sheet volume is independent of the Weber number and, furthermore, is solely parametrized by the nondimensional time t/τ_c. Note that the integration in Eq. (2.10) starts from $r = R_0$ as the original model assumes $u_r = 0$ at the pillar edge with the sheet remaining attached to the pillar while it expands [24]. To legitimize the comparison of the experiment with this model, the integration of the experimental data is performed over the same interval. The omitted center region (i.e., $r \in [0, R_0]$) may further contribute to the total volume with the disk feature contained in it (see Sec. 2.3.3.c). Taking as inputs the values of τ_c (i.e., 7.3 and 5.3 μs for droplet size $D_0 = 32$ and $26\,\mu$m, respectively), we find that Eq. (2.10) is able to predict the volume ratio with a high degree of accuracy [see Fig. 2.4(a)]. Figure 2.4(b) shows

the same data but now as a function of t/τ_c, along with Eq. (2.10). All data collapse together onto the universal curve given by Eq. (2.10), which demonstrates that t/τ_c is indeed the only relevant parameter for describing the volume fraction of the sheet.

2.3.3.b   *Volume of the rim and fragmentation*

Having experimentally concluded that the sheet contains less than half the total available mass in the time domain investigated, we turn to a theoretical analysis of the channels of mass loss from the sheet. As discussed above, a bounding rim on the edge of the sheet develops during sheet expansion, which has a volume $V_{\mathrm{rim}} = \pi^2 R(t) b^2/2$, where b is the rim diameter. Recently, it was shown that the rim diameter b of an expanding liquid sheet that undergoes unsteady fragmentation is universally governed by a local instantaneous Bond number $\mathrm{Bo} \equiv -\ddot{R}(t)\rho b^2/\sigma = 1$ [22]. We again refer to Eq. (2.9) for the expansion radius and the associated instantaneous deceleration $\ddot{R}(t)$ and obtain, upon substitution into $\mathrm{Bo} = 1$,

$$\frac{V_{\mathrm{rim}}}{V_0} = \frac{3\,\pi}{16} \left(\frac{3\,(\frac{t}{\tau_c})^3 - 4\sqrt{3}\,(\frac{t}{\tau_c})^2 + 4\,\frac{t}{\tau_c} + 4\,\frac{R_0}{U\,\tau_c}}{4\sqrt{3} - 9\,(\frac{t}{\tau_c})} \right). \tag{2.11}$$

Since $R_0/(U\,\tau_c) = \mathrm{We}^{-1/2} \ll 1$ for all cases studied here, this term can be neglected. Equation (2.11) can thus be approximated as a function of just t/τ_c, shown as the blue line in Fig. 2.4(b). The Bond-number criterion can be used to determine the rim thickness as long as the rim undergoes a sufficiently large acceleration of $(-\ddot{R}) \sim R_{\mathrm{max}}/\tau_c^2 \sim U/\tau_c$ [22]. As in our experiments the rim acceleration decreases with time, we apply Eq. (2.11) up to the moment at which $(-\ddot{R}) \approx U/\tau_c$, from which we obtain, using Eq. (2.9), $t/\tau_c \approx 0.55$. This limiting time is indicated in Fig. 2.4(b) by the black vertical line.

Clearly, the relatively slow monotonic increase in V_{rim} alone cannot account for the fast decrease in V_{sheet}. This observation suggests that the majority of the mass is lost through the remaining channel of fragmentation V_{fragment}. We express this volume by the complementary fraction

$$\frac{V_{\mathrm{fragment}}}{V_0} = 1 - \frac{V_{\mathrm{sheet}}}{V_0} - \frac{V_{\mathrm{rim}}}{V_0}, \tag{2.12}$$

which is represented by a red line in Fig. 2.4(b). We note that in contrast to $V_{\mathrm{sheet}}(t)$ and $V_{\mathrm{rim}}(t)$, which represent instantaneous quantities, $V_{\mathrm{fragment}}(t)$ is a cumulative volume representing the total volume of fragments formed up to that point in time. The

models presented in Fig. 2.4 are valid in both expanding and contraction phases of the laser-impacted sheet when the combined requirements of (i) sufficient deformation ($t > D_0/U$) and (ii) sufficient rim deceleration ($-\ddot{R} > U/\tau_c$) are met.

2.3.3.c   *Further contributions to the tin mass distribution*

Besides the contributions V_{sheet}, V_{rim}, and V_{fragment}, several other weaker channels of mass loss can be identified.

First, mass is lost due to plasma formation upon the impact of the laser pulse onto the droplet. Through momentum conservation, it is this accelerated mass that sets the droplet into motion [13]. Plasma formation may also lead to small splashing events producing some microparticulate debris. Full radiation-hydrodynamics simulations have, however, shown that these mass-loss channels only contribute a few percent [30].

Second, there is the disk feature as discussed in Sec. 2.3.1. A direct estimate of the mass contained in this feature can be obtained by considering the residue of the disk after its complete separation from the sheet and its subsequent contraction. Side- and front-view shadowgraphs, where available, enable a volume estimate. A first such investigation, even though limited by the optical resolution, indicates that the mass fraction may be as large as 10 % in certain cases. The size of this contribution and its origins thus warrant further research. Regardless, this disk contribution is relatively minor and will not affect the main conclusions of our studies.

2.4   Conclusion

We experimentally study the morphology of a radially expanding sheet of liquid tin formed upon nanosecond-pulse laser impact on a spherical microdroplet under conditions relevant for EUV lithography. The thickness profile of the several-tens-of-nanometers-thick tin sheet and its time evolution is captured over a range of Nd:YAG laser-pulse energies and two droplet diameters, $D_0 = 26\,\mu\text{m}$ and $D_0 = 32\,\mu\text{m}$, by employing two complementary methods. First, the transmissivity of the stretching liquid-metal sheet is recorded and used to determine the local thickness. Second, the Taylor-Culick opening speeds of spontaneously formed holes in the stretching sheet are experimentally determined, which allows us to obtain the thickness profile through an independent method. The two methods are shown to be in excellent agreement.

We show that all the sheet thicknesses measured collapse onto a single curve that is well described by the similarity solution proposed in Ref [20]. Spatial integration of the thickness profiles obtained experimentally provides the volume of the sheet.

Remarkably, less than half of the initial droplet volume remains in the sheet under conditions relevant for nanolithography.

Our further theoretical analysis indicates that the dominant fraction of the mass lost from the sheet during its expansion ends up as fragmented droplets. This fragment debris may lead to coating of nearby optic elements and hence may reduce the lifetime of industrial apparatus. To minimize the amount of fragment debris, it is best that the main laser pulse that creates the plasma-emitting EUV follows the prepulse with the smallest possible time delay. To enable the tin sheet to attain a sufficient size at this short time delay, an energetic prepulse is required to give it the required high expansion speed. These changes would enable optimization of the amount of tin contained in the sheet while minimizing the volume contributing to microparticulate debris in industrial sources of EUV light.
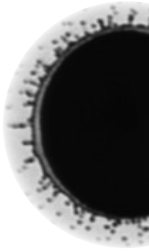
Appendix I: Scaling of the Weber number with pulse energy

The dynamics of droplet propulsion by laser-pulse impact have been detailed in Refs. [13, 30]. In these works, a scaling law of $U \sim E_{\text{od}}^{0.6}$ has been proposed that relates the center-of-mass speed U to the energy on droplet E_{od}, defined as the fraction of the incident pulse energy E that impinges onto the droplet. The Weber number $\text{We} = \rho U^2 R_0 / \sigma$ should then follow $\text{We} \sim E_{\text{od}}^{1.2}$. Figure 2.5 presents the scaling of the Weber number with the energy on droplet for three different droplet sizes. It is shown that the data are indeed in excellent agreement with the scaling law. Furthermore, the prefactors are consistent with the observations in Ref. [30], where the prefactor is predicted to be proportional to $R_0^{-2.2}$. Accordingly, the Weber numbers from different droplets sizes should follow the same trend when they are appropriately scaled as

$$\widetilde{\text{We}} = \text{We} \left(\frac{D_0}{45\,\mu\text{m}} \right)^{3.4}, \tag{2.13}$$

taking the droplet size in Ref. [30] ($D_0 = 45\,\mu\text{m}$) as a reference and also the prefactor from Ref. [30]. The inset in Fig. 2.5 shows that data from different droplet sizes collapse perfectly onto a single curve. These results enable the direct prediction of the
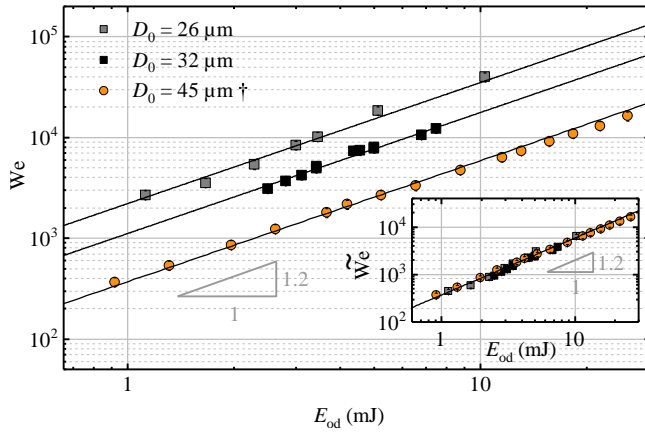
Figure 2.5: A double-logarithmic plot of the Weber number We as a function of the energy on the droplet E_{od} for the two studied droplet sizes. Individual fit results of the scaling law $\text{We} \sim E_{od}^{1.2}$ for different droplet sizes are shown as black lines. Data reproduced from Ref. [30] (†) for a larger droplet diameter ($D_0 = 45\,\mu\text{m}$) but for a similar beam size ($100\,\mu\text{m}$ FWHM) are also depicted, including the original scaling law. The inset shows the rescaled Weber number $\widetilde{\text{We}}$ as a function of E_{od}. The scaling law $\widetilde{\text{We}} \sim E_{od}^{1.2}$, with its prefactor taken from Ref. [30], is shown by a black line (see the main text).

Weber number from the laser-pulse energy impacting on the droplet over a wide range of experimental parameters.

CHAPTER 3

LASER-INDUCED VAPORIZATION OF A STRETCHING SHEET OF LIQUID TIN

Bo Liu⋆, Randy A. Meijer⋆, Javier Hernandez-Rueda, Dmitry Kurilovich, Zeudi Mazzotta, Stefan Witte, and Oscar O. Versolato
Journal of Applied Physics **129**, 053302 (2021)
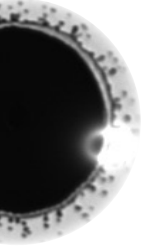
We experimentally study the mass distribution of a sheet of liquid tin formed by impact of a ns-laser pulse on a spherical microdroplet. The mass distribution is obtained using a low-intensity, second ns-laser pulse which induces vaporization of the stretching thin tin sheet. This careful vaporization enables the investigation of the thickness profile of the sheet, and its mass, at early times after laser pulse impact on droplet which have remained inaccessible by the methods used in recent work [B. Liu, *et al.*, Phys. Rev. Appl. **13**, 024035 (2020)]. The vaporization method moreover allows the visualization of the thick rim that bounds the thin sheet. Our results unambiguously demonstrate that increasing the energy of the ns-laser pulse incident on the droplet, which enables reaching a predetermined target radius more quickly, results in a larger mass fraction remaining in the sheet. Specifically, our studies show a doubling of the sheet mass fraction by reducing the required expansion time. As a corollary, less tin will end up in other channels of the mass distribution, such as fragments surrounding the sheet. Accordingly, more mass would be available in the target sheet for interaction with the more energetic, main laser pulse that is used in the industry to produce a hot and dense plasma from tin sheet targets in order to create extreme ultraviolet light for nanolithography.

⋆ Bo Liu and Randy A. Meijer contributed equally to this chapter as part of their PhD theses.

3.1   Introduction

State-of-the-art nanolithography machines make use of extreme ultraviolet (EUV) light which enables the continued miniaturization of semiconductor devices [12, 39–43]. In order to generate the EUV radiation, liquid tin microdroplets are used as mass-limited targets in a dual-laser-pulse irradiation sequence. First, a nanosecond laser pulse, termed *pre-pulse* (PP), irradiates the tin microdroplet, causing it to deform into a liquid sheet within a few microseconds [13, 14, 16, 17, 30, 31]. The sheet typically has a diameter of several hundreds of micrometers and thickness of several tens of nanometers [16, 17]. As the sheet expands, a bounding rim is formed at the edge of the sheet [16]. From this rim, a myriad of small fragments is propelled outwards along the radial direction [13, 16, 17, 30, 31]. When the sheet has reached a specified diameter, a second, more energetic *main-pulse* is used to generate a dense and hot tin plasma that emits the relevant EUV radiation [55].

Recently, our group reported on the hydrodynamic mechanisms that govern the thickness profile of nanosecond laser-induced sheets of liquid tin [16]. The experimental observations were used to benchmark a physical model that predicts the instantaneous sheet thickness and, from that, the mass of the sheet. Building on previous works [14, 20, 22, 24, 56], our research further confirmed the continuous loss of mass from the sheet over time. Remarkably, less than half of the initial amount of tin was found to remain in the sheet under currently relevant industrial conditions [16, 57, 58]. This finding is particularly pertinent in the context of EUV source lifetime, which is adversely impacted by tin debris. Our results further indicated that using a relatively more energetic PP could be beneficial: increasing the PP energy leads to a faster initial expansion rate of the target sheet, and thus any desired sheet size is reached earlier in the expansion trajectory, when more tin is carried by the sheet. To validate this proposition, knowledge of the sheet morphology at earlier times is needed. Since, inherently, the two methods previously used in Ref. [16] to determine the thickness profile are limited to mid- and late-time delays, we here employ an alternate method that is based on laser-induced vaporization. In this case, the sheets to be investigated will be irradiated by an auxiliary laser pulse, termed *vaporization pulse* (VP). This VP induces vaporization that gradually thins, or rarefies, the sheet into a mist comprising nanoparticles and, possibly, atomic tin. The vaporization process serves as a probe to estimate the amount of tin carried by the sheet: by measuring the time required to locally vaporize the sheet, we can infer its thickness profile at early time delays unattainable by the previously used methods. The obtained sheet thickness profile finally yields the fraction of the initial volume (or, equivalently, mass) still contained in the sheet.

In this paper, we investigate the tin mass distribution during laser-induced droplet deformation by introducing a method that allows us to obtain thickness profiles from careful laser-induced vaporization. Three target sheets are selected, representing the mass distributions formed using various PP energies and at different stages of the expansion process. All these targets share a common sheet radius $R_{sheet} \approx 210 \, \mu$m (referred to as $R^\star$ hereafter) when we probe their thickness profile and mass content using the auxiliary VP. This common sheet radius $R^\star$ lies within the range of diameters relevant for EUV generation in an industrial setting [57, 58] where this diameter range is set to a large degree by the diameter of the main-pulse. We use two different PP laser energies to demonstrate a higher mass content to be contained within the sheet when employing a higher PP energy. Additionally, we investigate two targets resulting from a constant PP energy yet at different moments during the expansion trajectory. We discuss the results stressing the importance of the time delay after the PP impact on the droplet as the key parameter that ultimately determines the mass distribution of the target.

3.2 Experiment and methods

In the experiment, a droplet generator, mounted on a tiltable bellow assembly, dispenses a vertically aligned microdroplet train of liquid tin (temperature 260 °C, density $\rho = 6968 \, \text{kg/m}^3$ and surface tension $\sigma = 0.55 \, \text{N/m}$) into a vacuum environment (10^{-7} mbar) with a velocity and repetition rate of approximately $10 \, \text{m s}^{-1}$ and 31.5 kHz, respectively. The droplets have a diameter of $D_0 = 2R_0 \approx 29 \, \mu$m (where R_0 is the droplet radius that is established with an uncertainty of $\pm 0.5 \, \mu$m) and a stable position, with instabilities on the order of a single micrometer in both horizontal and vertical directions. The droplet stream passes through a horizontal light sheet produced by a helium-neon laser and positioned approximately 2 mm above the center of the vacuum vessel, i.e., the laser-droplet-interaction point. The consequent light scattered by the droplets is detected by a photo-multiplier tube and the kHz-frequency signal is down-converted to 10 Hz to serve as a trigger for the acquisition and laser systems. For further details on the droplet generator, see also Ref. [36].

Two circularly polarized laser beams from independent Nd:YAG systems operating at 1064 nm wavelength are collinearly aligned onto the droplet [59]. The timing sequence of the laser pulses from these two systems is illustrated in Fig. 3.1(a). The PP, with a Gaussian 10 ns (full width at half maximum, FWHM) temporal shape, is focused down to a Gaussian spot with a size of 55 μm (FWHM) at the location of the droplet. The VP, delayed by a time interval Δt, is produced by an in-house built
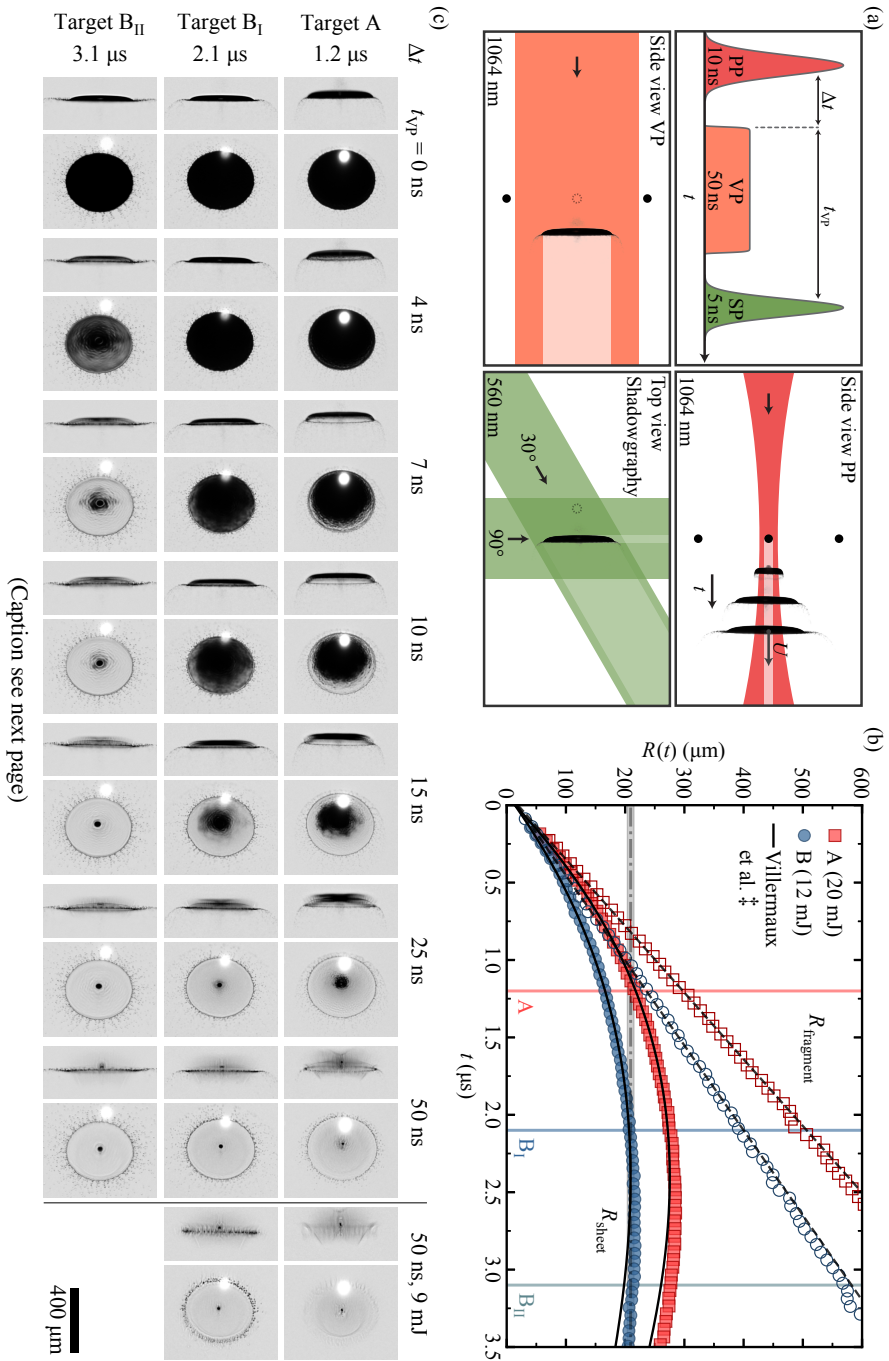
(Caption see next page)

Figure 3.1: (Previous page) (a) Illustration of the laser pulse sequence and the respective irradiation geometries. Upper-left: timing of the irradiation scheme, starting with the pre-pulse (PP), followed by the vaporization pulse (VP) after a time interval Δt. To visualize the dynamics of the tin target, the shadowgraphy illumination pulse (SP) is scanned through time t, where $t = 0$ marks the onset of the PP. The start of the VP is indicated by time delay $t_{VP} = 0$. Upper-right & lower-left: side-view schematics of the irradiation conditions during PP and VP, respectively. Lower-right: top-view of 30° and 90° shadowgraphy backlighting. (b) Sheet expansion radius R_{sheet} and farthest fragments distance-to-center $R_{fragment}$ as a function of time t for two PP energies (20 mJ and 12 mJ). The horizontal dash-dotted line (along with a shaded area to indicate the uncertainty) is at a constant 210 μm radius (i.e., $R^\star$). This line intersects the R_{sheet} curves at $t = 1.2$, 2.1 and 3.1 μs (as indicated by the vertical lines), at which moments the sheets are referred to as target A, B_I and B_{II}, respectively. The solid lines (‡) following R_{sheet} are fits of the model from Ref. [24] to the data up to 2 μs. The dashed lines along $R_{fragment}$ result from a linear fit to the data up to 1.5 μs. (c) Series of side-view (left) and front-view (right) shadowgraphy images of the three targets during illumination by the VP for different time delays. The VP energy $E_{VP} = 5$ mJ excluding the last column, where $E_{VP} = 9$ mJ. At $t_{VP} = 0$, all three targets share a common sheet size $R^\star$.

system with arbitrary pulse shaping capabilities [60]. The system is programmed to output a temporally square 50 ns pulse, and its top-hat spatial profile is imaged onto the target with a beam diameter of ≈ 950 μm. Therefore, the VP has a constant intensity distribution [denoted as I_{VP} (W/m^2)], both spatially and temporally.

The dynamics of the irradiated targets are captured by stroboscopic shadowgraphy imaging systems [13, 16, 31]. These systems combine incoherent pulsed backlight-illumination at 560 nm with CCD cameras coupled to long-distance microscopes, yielding a spatial resolution of approximately 5 μm. A dye laser provides the back-lighting shadowgraphy pulses (SP) with a spectral bandwidth of 12 nm (FWHM) and a pulse duration of 5 ns (FWHM). As depicted in Fig. 3.1(a), the shadowgraphy systems simultaneously provide front- and side-view images of the tin targets, with 30° and 90° angles with respect to the Nd:YAG laser beam propagation direction, respectively.

Initial optimization of the PP laser-to-droplet (L2D) alignment is performed by observing the target tilt and center-of-mass velocity U using the shadowgraphy systems [59]. As droplet position and beam pointing instabilities are on the order of single micrometers, no additional active stabilization is needed. Per shadowgraphy time delay, multiple (typically 10) frames are recorded to allow for post-filtering on optimal L2D.

Figure 3.1(a) (upper right panel) illustrates the typical response of a droplet to the impact of a PP [13, 14, 16, 17, 30]. The droplet is rapidly propelled to the velocity U on the order of 100 m/s along the propagation direction of the laser [13, 30]. Furthermore, the droplet deforms into an axisymmetric sheet that radially expands to a size R_{sheet} over *time* (indicated as t hereafter, where $t = 0$ marks the arrival of the PP). These orthogonal motions, characterized by U and the initial expansion rate immediately

after laser pulse impact $\dot{R}(t=0)$ (referred to as $\dot{R}_0$ hereafter), are driven by plasma pressure [13, 17, 30]. Typically, $\dot{R}_0 \sim U$ as in the analogous case of droplet-pillar impact studied in Ref. [24]. The time scale of the acceleration is similar to the laser pulse length ($\sim$ ns), vastly shorter than the time scale of the ensuing fluid dynamic deformation ($\sim \mu$s) [14, 43].

The sheet is irradiated by the VP [see Fig. 3.1(a), lower left panel] when it acquires a radius of $R^\star$. This onset moment of the VP is referred to as $t_{\text{VP}} = 0$. The result of irradiation by the VP is a gradual vaporization of the target sheet which we observe using the shadowgraphy imaging system as discussed further in Sec. 3.3.2.

3.3   Results and discussion

3.3.1   Target selection

To determine the moments at which the sheet reaches $R^\star$ for the chosen PP energies of $E_{\text{PP}} = 12$ mJ and 20 mJ, we first investigate the sheet size evolution $R_{\text{sheet}}(t)$ presented in Fig. 3.1(b). After PP impact, the sheet expands with an initial rate $\dot{R}_0$. With a higher PP energy, $\dot{R}_0$ is larger, and hence less time is required to reach $R^\star$. For the case of $E_{\text{PP}} = 20$ mJ, the sheet attains this specific size at $t = 1.2\ \mu$s. We refer to this target as target A. For the lower energy case of $E_{\text{PP}} = 12$ mJ, $R^\star$ is first reached at $t = 2.1\ \mu$s. We refer to this target as target B_{I}. After passing the apex of its expansion trajectory, the sheet retracts due to the surface tension exerted at the sheet edge [14, 16, 17] and again acquires $R^\star$ at $t = 3.1\ \mu$s, which we refer to as target B_{II}. We find that $R_{\text{sheet}}(t)$ agrees well with the analytical model developed by Villermaux and Bossa [24] for the analogous case of droplet impact onto a pillar. Such an agreement has been previously reported in Ref. [17]. By fitting this model to the data, we obtain the initial expansion rate $\dot{R}_0$ (for $E_{\text{PP}} = 20$ and 12 mJ, $\dot{R}_0 = 244$ and 182 m/s, respectively) with it being the only free fit parameter. Figure 3.1(b) also presents the radial position of the furthest fragments as a function of time $R_{\text{fragment}}(t)$. We find that these fragments follow an expected ballistic trajectory [21], the slope of which matches the initial expansion rate of the sheet $\dot{R}_0$. We note the significant difference in the distance between the outermost fragments and the sheet edge for the three targets. Each of these three targets, with the common sheet size of $R^\star$, is irradiated by the VP to infer the thickness profile $h(r)$ and mass content of the sheet.

3.3.2 Target vaporization

Figure 3.1(c) presents the front- and side-view shadowgraphy images of the targets through the duration of the VP with an energy of $E_{VP} = 5$ mJ. At the beginning of the VP (i.e., $t_{VP} = 0$), the images show that the main features of these targets include a sheet of liquid tin that is surrounded by small fragments. During VP illumination, we observe a gradual mass removal from the sheet as it becomes transparent to the background illumination light. The vaporized material does not significantly impede the shorter-wavelength shadowgraphy light and, thus, is not expected to influence the vaporization pulse. Over time, this transparency is seen to move from the periphery inward toward the center of the sheet, leaving a retreating inner sheet with a radius R_{inner}. Given the fact that the VP has a uniform intensity across the beam profile, we reasonably assume that more time is needed to vaporize a sheet that contains more tin and, as a result of the common sheet-size $R^\star$, is also thicker. Among the three targets, target A requires the longest time for its sheet to be completely vaporized, followed by targets B_I and B_{II}. We infer that the respective global sheet thicknesses and volumes follow the same order. As a side note, we find that the periphery of target A starts to show transmission prior to that of target B_I ($t_{VP} = 7$ ns). When the periphery of the sheet is removed, a bounding rim appears (see, e.g., front-view images at $t_{VP} = 25$ ns). Such a bounding rim has been widely reported in various scenarios of droplet impact on a solid [20, 22, 24, 25, 53, 54]. For the case of laser-droplet impact, the thickness and mass of this rim has been analytically estimated in our previous work [16] and now is visualized. Note that for target B_{II}, the sheet as a whole appears to become transparent almost simultaneously [see Fig. 3.1(c) at $t_{VP} = 4$ ns] instead of gradually retreating inward. This is due to the vaporization taking place on a timescale similar to the duration (≈ 5 ns) of the shadowgraphy illumination pulse.

By the end of the VP ($t_{VP} = 50$ ns) the sheet is completely removed for all targets. In contrast, the rim and many of the fragments are still present, indicating that the sheet is much thinner than the rim and fragments, as was also identified in Ref. [16]. Although the rim and most of the fragments are not fully resolved by our imaging system, from the observed contrast [61] we do infer that target A has a thinner rim (with a diameter of approximately 1-2 μm) and finer fragments compared to the other targets. In fact, target A has such small-sized fragments that a VP of 5 mJ is capable of vaporizing a significant fraction of them by the end of the VP. With a higher VP energy of 9 mJ, all the fragments and the rim of target A are completely vaporized [see the rightmost column in Fig. 3.1(c)]. In contrast, for targets B_I and B_{II}, no clear vaporization of fragments is observed for a 5 mJ VP, and even with the 9 mJ VP some fragments and leftovers of the rim remain for target B_I. Besides the rim and fragments,

a remnant of tin resides at the center of the sheet ($t_{VP} = 50$ ns). Its presence after VP irradiation indicates that also its thickness is significantly larger than that of the sheet. The existence of this center mass is also consistent with our previous observations in Ref. [16].

In Fig. 3.2(a), we present the radius of the inner sheet $R_{inner}(t_{VP})$ as it evolves throughout the VP duration. The inner radii have been retrieved from shadowgraphy images such as those shown in Fig. 3.1(c). Again, in Fig. 3.2(a), we identify that R_{inner} reduces over time for all targets, among which that of targets A and B_{II} decreases at the slowest and the fastest rate, respectively. In the experiment, we found that at a given location r on the sheet, the local time $\tilde{t}_{VP}(r)$ required for the VP to vaporize the local thickness $h(r)$ is inversely proportional to I_{VP}. This has been systematically observed in a scan for various VP pulse energies (ranging from 2 to 9 mJ). The linear proportionality $\tilde{t}_{VP}(r) \propto I_{VP}^{-1}$ indicates that the thickness $h(r)$ is proportional to the VP energy locally deposited in the sheet, i.e. $h(r) \propto I_{VP}\tilde{t}_{VP}(r)$. With a constant VP intensity I_{VP}, we can thus conclude $h(r) = \tilde{t}_{VP}(r)\dot{h} \sim \tilde{t}_{VP}(r)$, where $\dot{h}$ refers to a time-average vaporization rate. We make the ansatz that $\dot{h}$ is independent of the local thickness. Thus, the thickness profile of the sheet can be directly obtained from R_{inner} radii shown in Fig. 3.2(a) by exchanging the x- and y-axes and using a single overall scaling factor $\dot{h}$.

3.3.3   Thickness & mass content of the targets

In Ref. [16], a partial transparency of the sheet to the shadowgraphy backlighting was used to determine the sheet thickness profile. A significant transmission signal can only be obtained if the sheet is sufficiently thin. We find that this transmission method can be applied to the thinnest target, B_{II}, and we determine its sheet thickness before VP impact ($t_{VP} = 0$). Subsequently, we are able to determine the scaling factor $\dot{h}$ from a fit such that $h(r) = \tilde{t}_{VP}(r)\dot{h}$ for target B_{II} matches its thickness as acquired from the transmission method in absolute terms, as presented in the inset of Fig. 3.2(b). The fit shows excellent agreement between the two methods regarding the shape of the sheet thickness. This fit yields $\dot{h} = 4.4(4)$ m/s, with the systematic uncertainty in brackets originating from uncertainties in the background correction related to, e.g., dark noise or plasma glare [16, 61]. The obtained $\dot{h}$ lies in the range of values obtained in other studies of the ablation of metals under similar irradiation conditions (here the VP fluence is ≈ 0.7 J/cm^2) [62, 63]. With the known value of $\dot{h}$, we are able to plot the thickness profiles for targets A and B_I.
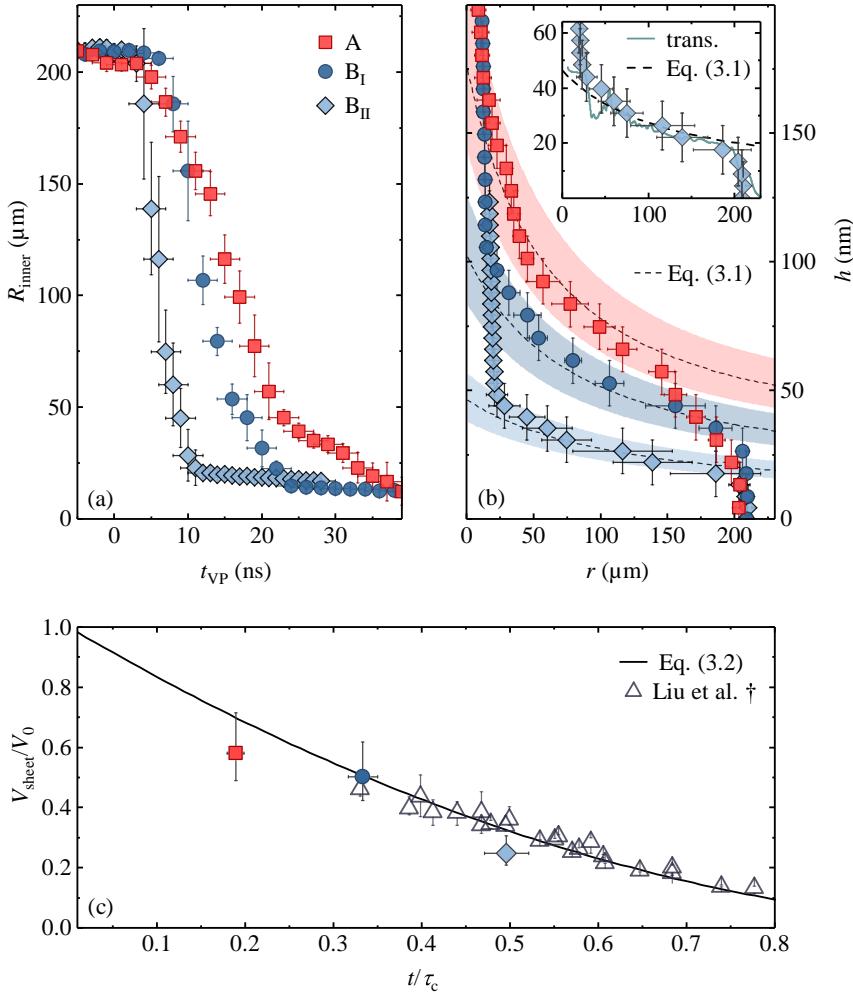
Figure 3.2: (a) Radius of the inner sheet R_{inner} as a function of t_{VP} during VP-induced vaporization. (b) Sheet thickness h, obtained by $h(r) = \tilde{t}_{\text{VP}}(r)\dot{h}$, as a function of radial position r. The time-averaged vaporization rate $\dot{h}$ is obtained by fitting the thickness of target B_{II} obtained from the transmission method to the corresponding data of $t_{\text{VP}}(R_{\text{inner}})$, see the main text. The result of this fit is presented in the inset. The thickness model given by Eq. (3.1) is presented by the dashed line, with the shaded region indicating the uncertainty propagated from $R_0 \pm 0.5\,\mu$m and $\dot{R}_0 \pm 5\%$. (c) Volume ratio of the sheet to the initial droplet V_{sheet}/V_0 as a function of the scaled time t/τ_c, where $\tau_c = 6.6\,\mu$s, with values $0.58^{+0.13}_{-0.09}$, $0.50^{+0.12}_{-0.08}$, and $0.25^{+0.06}_{-0.04}$ for targets A, B_{I}, and B_{II}, respectively. Previously reported data (open triangles) from Ref. [16] (†) are presented alongside the new results. The solid line depicts Eq. (3.2).

Figure 3.2(b) presents the sheet thickness $h(r) = \tilde{t}_{\mathrm{vp}}(r)\dot{h}$ as a function of the radial position r for all targets. Moreover, we plot the semi-empirical thickness model [16]

$$h(r, t) = \frac{D_0^3}{1.65\,(\dot{R}_0\,t)^2 + 6.9\,t\,r\dot{R}_0 - 2.4\,r^2}. \tag{3.1}$$

It is shown in Fig. 3.2(b) and its inset that Eq. (3.1) agrees well with the current thickness profiles, both obtained from $h(r) = \tilde{t}_{\mathrm{vp}}(r)\dot{h}$ and, for target B_{II}, also from the independent measurement from the transmission method. Here, we employ the initial expansion rate $\dot{R}_0$ as the characteristic velocity in Eq. (3.1) instead of the center-of-mass speed U as originally used in Ref. [16]. This substitution is motivated by a relatively strong deviation from the $\dot{R}_0 \sim U$ similarity [20, 24] for targets B_{I}, B_{II}, arising from the tight focusing condition of the PP used here. As elucidated in Ref. [14], the spatial distribution of the pressure field exerted by the expanding plasma on the droplet surface influences the ratio $\dot{R}_0/U$. A loosely focused beam (i.e. 105 μm at FWHM in Ref. [16]) and also an increasing PP energy [17] effectively results in a spreading pressure distribution that yields $\dot{R}_0/U \approx 1$. In contrast, an increasingly focused pressure field, which, for example, can be achieved by employing a tightly focused beam (i.e. 55 μm at FWHM for the present study), results in a larger fraction of the kinetic energy partitioned to expand the droplet rather than to propel it, and thus $\dot{R}_0/U > 1$. Our analysis indeed shows $\dot{R}_0/U = 1.26$ for targets B_{I} and B_{II}, and $\dot{R}_0/U = 1.09$ for target A, justifying choosing $\dot{R}_0$ as the relevant velocity describing the deformation dynamics.

The thickness data $h(r)$ shown in Fig. 3.2(b) enables the determination of the sheet volume by integrating $2\pi r h(r)\delta r$ along the radial coordinate, starting from R_0 to the edge of the sheet [16, 24]. The region $r < R_0$ is thus excluded from the integration (cf. Refs. [16, 24]) and with it the center mass remnant [see Fig 3.1(c)] that has a different physical origin [16]. Figure 3.2(c) presents the obtained volume ratio of the sheet to the initial droplet V_{sheet}/V_0 as a function of the nondimensional time t/τ_c, with capillary time $\tau_c = [\rho R_0^3/\sigma]^{1/2} = 6.6\,\mu$s. The data indicate a monotonic decrease of the fraction of tin contained in the sheet over time. At the moment of $t/\tau_c = 0.19$ (i.e., target A), the sheet carries close to 60% of the initial amount of tin. For comparison, the data of V_{sheet}/V_0 from Ref. [16] are also shown in panel (c). Despite the differences in the experimental conditions (regarding R_0, E_{PP}, and the focal spot size of the beam) between the present study and Ref. [16], these two data sets agree well with each other.

Additionally, in panel (c) we plot the model

$$\frac{V_{\text{sheet}}}{V_0} = \left(1 - \frac{\sqrt{3}}{2}\frac{t}{\tau_c}\right)^2, \tag{3.2}$$

which was derived in Ref. [16] using the analytical expression of the thickness profile and the radius of the sheet from Ref. [24]. Equation (3.2) was found in Ref. [16] to be able to describe the sheet volume for the laser-droplet impact case. Figure 3.2(c) shows that in the present study, Eq. (3.2) is consistent with the experimental findings also in the early time regime. Further experimental data would benefit the detailed study of the full evolution of the sheet thickness and its volume, and is needed to attest to the general validity of Eq. (3.2), in particular at the early times that have now become accessible employing the laser-induced vaporization method. In short, our results show a good agreement with the prediction from Eq. (3.2), and match well with our previous study in Ref. [16] in the late-time overlap region. We thus unambiguously demonstrate that increasing the energy of the laser pre-pulse that, crucially, enables the sheet to reach a specified target size more quickly, results in a significantly larger mass fraction contained in the sheet.

3.4 Conclusion

In this paper, we experimentally investigated the mass content of expanding sheets of liquid tin, formed upon nanosecond pre-pulse laser impact on tin microdroplets. An auxiliary vaporization laser pulse was used to gradually remove mass from the liquid sheet, thereby exposing the sheet's thickness profile and mass content. Furthermore, the removal of the sheet revealed and confirmed the presence of a sheet bounding rim and center mass. Three targets, generated by using two different PP energies, were selected at different times during their expansion trajectories such that they all shared a common sheet size $R^{\star} = 210\,\mu$m. The thickness of the thinnest target has been independently determined by an optical method that has been validated in Ref. [16]. The resulting thickness enabled the conversion of the local time of vaporization of the other two targets by the auxiliary pulse to the thickness profiles of the sheets. We have further shown that the thickness for each target agrees well with the model developed in Ref. [16]. The spatial integration of the obtained thickness profile yielded the volume fraction of the sheet for each target, for which we found a good agreement with previously reported models. The results confirmed how using a more energetic PP

is a favorable strategy for achieving a specified sheet size while minimizing mass loss from the sheet to the bounding rim and fragments. For the target with the highest PP energy studied here, we found that approximately 60% of the mass was still present in the sheet, more than doubling the mass fraction that may be expected to be contained in targets reported in the available literature relevant for the nanolithography industry [57, 58]. From the perspective of debris mitigation, such a target may also be preferred as, complementary to a larger sheet mass fraction, less mass is carried by the fragments. Investigations of the thickness profile and target mass at even earlier times after laser pulse impact are accessible by the laser-vaporization method. Our findings and method can serve a crucial role in the optimization of PP parameters, maximizing the tin mass available for the production of EUV light in tin-droplet-based plasma sources for nanolithography.
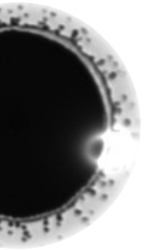
CHAPTER 4

EARLY-TIME HYDRODYNAMIC RESPONSE OF A TIN DROPLET DRIVEN BY LASER-PRODUCED PLASMA

Javier Hernandez-Rueda, Bo Liu, Diko J. Hemminga, Yahia Mostafa, Randy A. Meijer, Dmitry Kurilovich, Mikhail Basko, Hanneke Gelderblom, John Sheil, and Oscar O. Versolato
Physical Review Research **4**, 013142 (2022)[1]

We experimentally and numerically investigate the early-time hydrodynamic response of tin microdroplets driven by a ns-laser-induced plasma. Experimentally, we use stroboscopic microscopy to record the laser-induced dynamics of liquid tin droplets and determine the propulsion speed (U) and initial radial expansion rate ($\dot{R}_0$). The ratio of these two quantities is a key parameter to be optimized for applications in nanolithography, where laser-impacted tin droplets serve as targets for generating extreme ultraviolet light. We explore a large parameter space to investigate the influence of the tin droplet diameter, laser beam diameter and laser energy on the $\dot{R}_0/U$ ratio. We find good agreement when comparing the experimentally obtained U and $\dot{R}_0$ values to those obtained by detailed radiation-hydrodynamic simulations using RALEF-2D. From the validated simulations, we extract the spatial distribution of the plasma-driven pressure impulse at the droplet-plasma interface to quantify its influence on the partitioning of kinetic energy channeled into propulsion or deformation. Our findings demonstrate that the width of the pressure impulse is the sole pertinent parameter for extracting the kinetic energy partitioning, which ultimately determines the late-time target morphology. We find good agreement between our full radiation-hydrodynamic modeling and a generalized analytical fluid-dynamics model [Gelderblom *et al.* J. Fluid Mech. **794**, 676 (2016)]. These findings can be used to optimize the kinetic energy partition and tailor the features of tin targets for nanolithography.

---

[1]Bo Liu contributed to this chapter as part of his thesis regarding the design of experiments, data collection, and post-analysis.
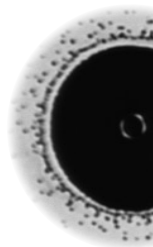
4.1   Introduction

Today, state-of-the-art nanolithography machines employ liquid tin microdroplets as mass-limited targets to generate extreme ultraviolet (EUV) light, which is then used to produce semiconductor devices with unprecedented spatial resolution [43, 57, 58, 64, 65]. In this context, the generation of EUV light is based on a two-step process, where a first laser pulse (prepulse) shapes an initially spherical droplet into a thin layer of tin (target) [12]. This target is then illuminated by a second pulse (main pulse) to produce a dense and hot tin plasma, where several of its charge states (Sn^{10+}– Sn^{14+}) preferentially emit EUV radiation with a wavelength centered around 13.5 nm [55, 66–70]. A full understanding and control of the (prepulse) laser-induced tin droplet dynamics over different timescales is key to optimize EUV source operation [41, 71–74].

The interaction of a nanosecond laser prepulse with a spherical tin microdroplet can be separated into three main phases: (i) the initial laser-tin interaction and plasma generation and expansion on a nanosecond timescale, followed by (ii) an early deformation of the droplet lasting hundreds of nanoseconds and a subsequent (iii) fluid dynamic response of the system on a microsecond timescale, where surface tension plays a central role in shaping the target morphology. The characteristic times of these stages are illustrated on a logarithmic timeline in Fig. 4.1(a), more details of the timescale separation can be found in Refs. [13, 14, 28]. During the *first stage*, the laser-tin interaction drives the generation of a plasma whose rapid expansion imprints a pressure impulse at the droplet-plasma interface, radially expanding the droplet and propelling it along the laser propagation direction. The initial expansion rate $\dot{R}_0$ and the ballistic propulsion velocity U are on the order of 100 m/s [13–16, 28, 30]. Any plasma onset effects are short, on the hydrodynamic time scale $\tau_h \sim 0.1$-1 ns [13, 28, 75] — much shorter than the laser pulse length τ_p, so $\tau_h \ll \tau_p$ such that an ablation front is established providing plasma pressure over the full $\tau_p \sim 10$ ns time scale. In the *second stage*, the droplet starts to deform into a circular thin sheet. This early deformation takes place during the inertial time $\tau_i = R_0/\dot{R}_0 \sim 100$ ns, for a droplet radius $R_0 \sim 10\,\mu$m. As deformation progresses towards the *third stage*, a rim forms at the periphery of the sheet, where surface tension causes a deceleration of the sheet's radial expansion rate on the capillary timescale $\tau_c = [\rho D_0^3/(6\sigma)]^{1/2} \sim 10\,\mu s^2$, with the droplet diameter D_0, the liquid density $\rho = 6900\,\text{kg m}^{-3}$ and the surface tension $\sigma = 0.55$ N/m [13–16, 22, 24, 28]. The surface tension drives the radial contraction of

---

[2]The definition of the capillary time in this Chapter is different from that used in Chapters 2 and 3 where $\tau_c = (\rho R_0^3/\sigma)^{1/2}$.

the sheet and fluid dynamic instabilities both on the sheet [16, 17] and at the rim [22, 23]. The instabilities at the rim, in turn, form ligaments that eventually shed fragments via pinch-off processes [17, 23]. Given the complexity of this dynamic deformation process, controlling the $\dot{R}_0/U$ ratio is crucial to tailor the precise target morphology. In an industrial setting, a specific target size is obtained by expanding at a rate $\dot{R}_0$ over a preset time interval. In this context, the propulsion speed U can be identified as a side-effect from obtaining $\dot{R}_0$, essentially a loss channel of kinetic energy. Therefore, it is highly relevant to elucidate the physics that dictates how much of the deposited laser energy is channeled to radial deformation kinetic energy $E_{k,d}$ and forward propulsion kinetic energy $E_{k,cm}$ of tin targets and enable optimization thereof [14].

To understand the kinetic energy partitioning in the current problem, we can draw upon well-established analogies with droplet impact upon a rigid substrate, where the impact velocity U is identified as the characteristic speed to describe the hydrodynamic response and sets the kinetic energy as the initial condition of the process [24, 25, 32, 33, 76–78]. However, in the classical case of drop impact onto a pillar, the late hydrodynamic response may further depend on the initial expansion rate $\dot{R}_0$ of the droplet, which deviates from U when varying the relative size of the drop with respect to the pillar diameter [20, 24, 79]. In case of droplets irradiated by pulsed lasers (be it vapor-propelled water [28] droplets or plasma-propelled tin droplets [13]), there is no rigid body and instead the impact process is governed by the laser-matter interaction, which requires a more complex description of the mechanisms involved in the impact. The relation between a predefined pressure pulse and the fluid dynamic response of a droplet has been analytically described in Ref. [14]. In that work, the initial velocity field inside a droplet was derived by considering inviscid and incompressible flow after applying an instantaneous pressure impulse at a liquid droplet surface. In Ref. [14], the full hydrodynamic response (early and late stages) is then solely and fully determined by the ratio of kinetic energy initially channeled to deform the droplet and the kinetic energy to propel its center-of-mass. Although this work established a solid link between the partitioning of kinetic energy $E_{k,d}/E_{k,cm}$ in the droplet and a given analytical (and instantaneous) pressure impulse, a detailed description and understanding of the pressure impulse generated by the expanding plasma cloud itself is lacking. Moreover, the validity of the aforementioned assumptions (i.e., instantaneous, inviscid, incompressible) remain to be ascertained for the current, rather extreme case of a laser-impacted tin droplet.

In this work, we combine experiments and radiation-hydrodynamics simulations to investigate the ns-laser-induced early-time fluid dynamic response of liquid tin microdroplets. First, we experimentally record the evolution of the liquid tin morphology using stroboscopic shadowgraphy, from which we extract both the propulsion velocity
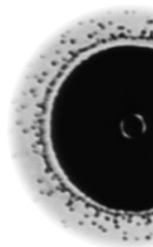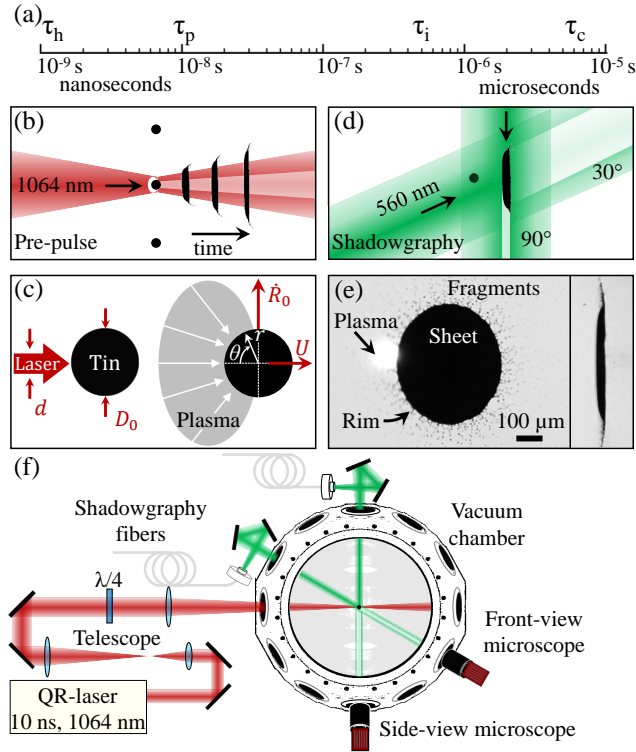
Figure 4.1: Schematics of laser-tin droplet interaction. (a) Characteristic times during and after the laser-droplet interaction. (b) Schematic of the irradiation geometry (side view). A liquid tin micro-droplet is irradiated using a single focused ns-laser beam. The black circles represent the tin droplets and the elongated shadows illustrate the expanding tin target. (c) Schematic of the laser-droplet system with the most relevant parameters, including the laser beam d and droplet D_0 diameters and the propulsion U and radial $\dot{R}_0$ velocities. The cartoon on the right-hand side illustrates the momentum transfer to the droplet mediated by the laser-induced plasma expansion recoil. The cartoon also shows the polar coordinate system (r,θ) with its origin at the droplet center. (d) Schematic representation (top view) of the shadowgraphy illumination at 30° and 90° used to image the deforming droplet target. (e) Experimental front-view (left) and side-view (right) shadowgraphy images of an expanding sheet of tin. (f) Schematic of the top view of the experimental system.

U and expansion velocity $\dot{R}_0$. We systematically investigate the influence of the droplet diameter D_0, beam diameter d and laser energy E on U and $\dot{R}_0$. The experimental U and $\dot{R}_0$ velocities agree well with those obtained from radiation-hydrodynamic simulations performed with the RALEF-2D code. The simulations further allow us to extract the pressure impulse at the droplet-plasma interface. We identify the

width of the pressure impulse as the crucial characteristic length governing the kinetic energy partitioning $E_{k,d}/E_{k,cm} = f(\sigma)$. Thus, we elegantly describe the balance of kinetic energy channeled to the deformation or propulsion of the droplet using a single parameter that comprises the effect of all the experimental parameters: d, D_0 and E. Finally, this energy partition is compared with the predictions of a purely fluid dynamic model developed in Ref. [14].

4.2 Experiment

Figure 4.1(b) illustrates the tin droplet irradiation geometry, where a single laser prepulse illuminates a tin micro-droplet. The recoil pressure exerted by the expansion of the laser-produced plasma gives rise to a propulsion and a radially symmetric deformation characterized by the center-of-mass velocity U and the radial velocity $\dot{R}_0$, as shown in Fig. 4.1(c). In the current experiments, these velocities are on the order of 100 m/s. To study the expansion and propulsion dynamics, we use a stroboscopic shadowgraphy system as depicted in Fig. 4.1(d). This system provides front- and side-view images as a function of the time between the laser prepulse and the shadowgraphy probe pulse. In Fig. 4.1(e) we provide an example of shadowgraphy images and illustrate the main constituents of the expanding tin target.

4.2.1 Experimental setup

In the following, we explain the experimental system illustrated in Fig. 4.1(f); more details can be found in Ref. [36]. A vertical train of spherical liquid tin droplets (260 °C) is dispensed using a piezo-electric-driven droplet generator, which is mounted on a motorized assembly that adjusts the direction of the train. Its repetition rate ranges from 5 kHz to 65 kHz, which allows for accurate control of the droplet diameter D_0 from 55 μm to 25 μm. The droplets have a speed of 11 m/s while they pass through the center of a vacuum vessel (10^{-7} mbar). The droplets are illuminated using a light sheet generated by a He-Ne laser combined with a cylindrical lens. The scattered light is collected by a photo-multiplier tube, down-converted to 10 Hz and used to trigger a Nd:YAG laser and the imaging systems.

For the laser experiments, we use a Nd:YAG laser system (Quanta-Ray, Spectra-Physics) that delivers linearly polarized pulses at a central wavelength of 1064 nm, with a repetition rate of 10 Hz. The laser has a Gaussian temporal profile with a pulse duration of $\tau_p = 10$ ns (FWHM). From this point forth, we simply refer to the prepulse laser as laser. The laser passes through a quarter-wave plate to attain circular polarization at the droplet surface, which allows us to attain cylindrical symmetry of the
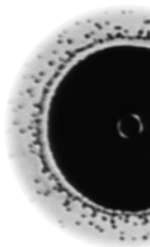
laser energy deposition at the surface of the droplets, thus leading to an axisymmetric expansion. We use two telescopes to provide beam diameters of either 1 or 4 cm before passing through our focusing optics. We then focus the laser beam using a lens with a focal distance of 300 mm and a diameter of 7.5 cm. The full width at half maximum (FWHM) of the focused laser beam at the droplet location was adjusted in the range 15–130 μm by carefully modifying the position of the lens. The 1 cm and 4 cm input beam diameters enable us to scan ranges of 40–130 μm and 15–50 μm, respectively. Before the laser-tin interaction experiments, the laser Gaussian spatial distribution was characterized using a beam profiler by recording images of the attenuated laser beam while changing the distance between the lens and the center of the vacuum chamber. These images were used to characterize the beam diameter and the laser energy fraction impinging on the droplet surface.

The laser-induced dynamics of the irradiated droplets were recorded using a stroboscopic shadowgraphy imaging system. This system uses incoherent light pulses at 560 nm with a pulse duration of 5 ns to illuminate the expanding tin target by imaging it onto the chip of a CCD camera using a long-distance microscope (K2 Distamax, Infinity). Two twin shadowgraphy systems are used to record the dynamics at 30° (front view) and 90° (side view) with respect to the laser beam propagation axis. These imaging systems provide a spatial resolution of 5 μm. The time delay between the prepulse laser and the shadowgraphy pulses was set to start at $t = $ -500 ns extending up to 4000 ns.

4.2.2   Experimental results

In the following, we will examine the laser-induced target morphology, propulsion speed U and the initial expansion rate $\dot{R}_0$ of the droplet and their dependence on the variables of E, d and D_0 for a large parameter space. The droplet response is also influenced by the polarization state [80] and the temporal intensity distribution of the laser [38, 81], which we set to be constant here.

4.2.2.a   Target morphology

In Fig. 4.2, we show a set of representative shadowgraphy images of the expanding tin target at several time delays (columns). These images illustrate a variety of morphologies that are the result of irradiating droplets with three different diameters (D_0 rows), while keeping a constant laser beam diameter and energy ($d = 20\ \mu$m and $E = 0.8$ mJ). The ablation of smaller droplets leads to flatter tin morphologies forming an axisymmetric thin sheet (see bottom row with $D_0 = 27\ \mu$m). For larger droplets, morphologies
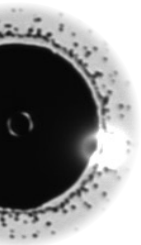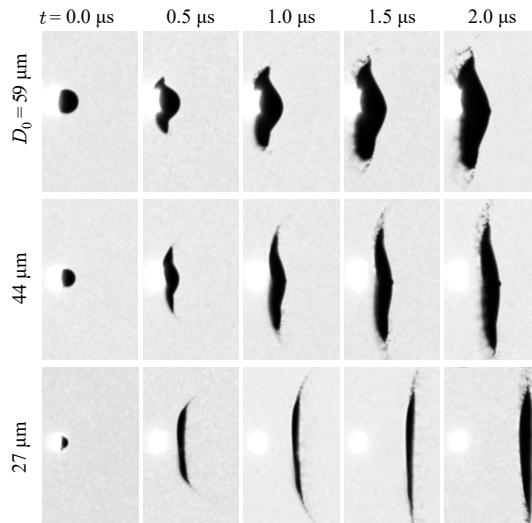
Figure 4.2: Set of representative side-view shadowgraphy images. Each image illustrates the target morphology considering different droplet diameters (rows) and time delay after laser illumination (columns). Note that the laser beam propagates from left to right in the images and thus impinges on the left side of the droplets. Here, we set $d = 20\,\mu m$ and $E = 0.8\,mJ$. The bright spot in all images corresponds to the laser-induced plasma emission. The images capture an area of 425 μm by 270 μm.

with a smaller radius of curvature are observed. This curved morphology is caused by a non-homogeneous (but cylindrically symmetric) laser energy deposition at the droplet surface, as the beam is much smaller than the droplet and a certain area of the droplet surface remains unaltered. The top row exemplifies this effect, where the beam diameter ($d = 20\,\mu m$) is approximately one third of the droplet diameter $D_0 = 59\,\mu m$. This case shows a partial ablation of the droplet surface around its pole, which resembles the ablation of a flat liquid pool as it generates a similar crown-shaped splash [82]. In contrast, the bottom row illustrates an experiment where the whole left hemisphere of the droplet is illuminated by the laser and, therefore, is ablated more homogeneously.

In addition to the morphology, the shadowgraphy images in Fig. 4.2 illustrate a change in propulsion speed and expansion rate when varying the droplet size. This becomes evident when comparing the sheet positions at $t = 2\,\mu s$ (rightmost column) between the $D_0 = 59\,\mu m$ and $D_0 = 27\,\mu m$ cases, where a faster propulsion speed for smaller, and thus lighter, droplets is observed. Furthermore, smaller droplets exhibit a faster initial expansion rate, which can be seen by comparing the sheet diameters at $t = 0.5\,\mu s$ for different droplet sizes. Next, we will quantitatively explore the propulsion
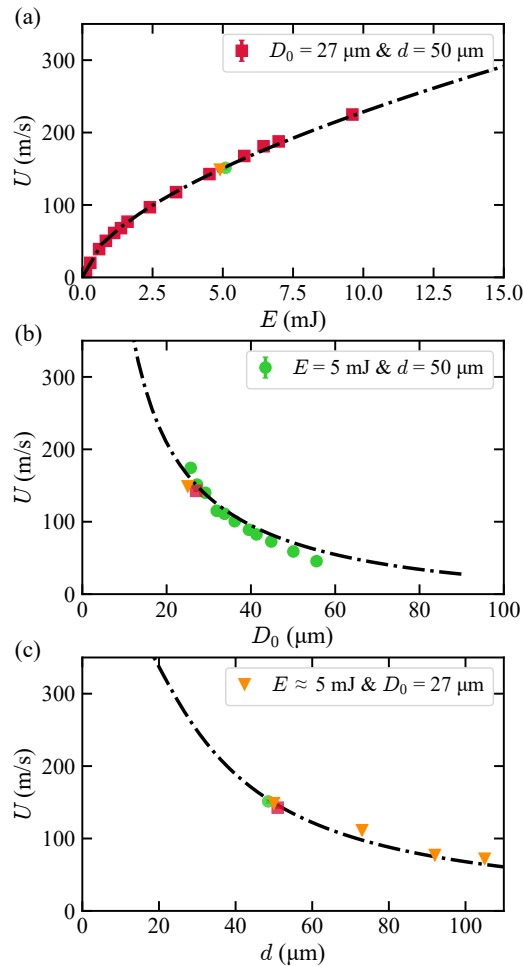
Figure 4.3: Experimental center-of-mass velocity U. Graphs of U as function of (a) the laser energy E, (b) droplet diameter D_0 and (c) beam diameter d. In (a), the droplet and beam diameters were set to $D_0 = 27$ μm and $d = 50$ μm, respectively. In (b), the beam diameter and the energy were set to $d = 50$ μm and $E = 5$ mJ. In (c), the droplet diameter and the energy were set to $D_0 = 27$ μm and $E \approx 5$ mJ. In all graphs the dash-dotted lines are the result of a global fit of Eq. (4.2) to the data. Overlapping symbols are horizontally offset for visibility.

and expansion rates and their dependence when varying E, d and D_0.

4.2.2.b   *Laser-induced propulsion of liquid tin droplets*

The acceleration of the droplet to a center-of-mass velocity U takes place in the short timescale of $\tau_p \sim 10$ ns, after which U remains constant. This velocity can be described by a function of several laser and geometrical parameters $U = f\left(d, D_0, E\right)$ as shown in Refs. [16, 28, 30]. Our current work explores this dependence for a much larger parameter space, in which we explicitly consider the case where the beam size is smaller than the droplet size $d < D_0$ (see full data sets provided in the Appendices). Figure 4.3 presents U as a function of E, D_0, and d as independent variables. The data indicate that the propulsion velocity increases with increasing laser energy in panel (a) and decreasing droplet (b) and beam diameters (c). These observations agree well with our previous study in Ref. [30], where the *energy-on-droplet* E_{od} was identified as the principal parameter determining U (considering a single D_0 value). The E_{od} is defined as the incident laser energy illuminating the droplet surface, i.e., it accounts for the geometrical overlap of the laser beam profile and the spherical droplet surface as

$$E_{od} = E\left(1 - 2^{-D_0^2/d^2}\right). \tag{4.1}$$

A power-law dependence of U with E_{od} has been established by Kurilovich *et al.* [30] as

$$U = K_U E_{od}^{\alpha}, \tag{4.2}$$

with $K_U = K_U'(50\,\mu\text{m}/D_0)^{1+2\alpha}$, where K_U' is a proportionality factor that does not depend on D_0 [30]. The exponent α originates from the correlation between the plasma pressure and the laser pulse intensity and was determined to be $\alpha = 0.6$ in Refs. [13, 30]. Naturally, an increase in pulse energy leads to a higher E_{od}, which yields a higher propulsion velocity, as seen in Fig. 4.3(a). On the one hand, a larger droplet size increases the overlap with the incident beam, leading to a larger E_{od} and to a larger impulse exerted by the plasma pressure. On the other hand, the mass of the droplet and hence the momentum corresponding to a certain propulsion velocity increases following $P \sim D_0^3 U$. As a result, the propulsion velocity is expected to decrease with increasing droplet size, which is consistent with our observations in Fig. 4.3(b). As for the beam size, a tightly focused beam, while keeping a constant $E-D_0$ combination, leads to a higher E_{od}, which therefore results in a larger U as shown in panel (c). Equation (4.2) is then fitted to our data in Fig. 4.3 with (a) E, (b) d and (c) D_0 as independent variables. We perform a global fit to all data in Fig. 4.3 with the power α fixed to 0.6 while leaving K_U' as a free fitting parameter. The fit
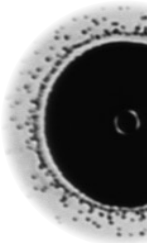
yields a sole prefactor equal to $K'_U = 41(5)\,\mathrm{m\,s^{-1}\,mJ^{-0.6}}$, which agrees well with a value $K'_U = 36(3)\,\mathrm{m\,s^{-1}\,mJ^{-0.6}}$ obtained in Refs. [13, 30]. The specified uncertainty is dominated by the error in characterizing the beam diameter d at the location of the droplet. Moreover, the global fit shown here is consistent with the fit presented in Fig. 4.8(a) in the Appendices, which also yields $K'_U = 41\ \mathrm{m\,s^{-1}\,mJ^{-0.6}}$. In Fig. 4.8(a), Eq. (4.2) is fit to the combined U, E_{od} data that collapses onto a single curve for seven beam diameters that scale from $17\,\mu\mathrm{m}$ up to $100\,\mu\mathrm{m}$.

    Our study validates the applicability of Eq. (4.2) over a wide range of $d{-}D_0{-}E$ combinations including the case where the laser focus is smaller than the droplet. For the case of $d < D_0$ we have no grounds to assume that the coefficient K_U is a function of D_0 only, and one should explicitly account for the dependence on d as well. In this case the imparted momentum would scale with d^2, following the intersecting beam-droplet area. However, the precise scaling is influenced by (i) the reduction of the fraction of propelled mass, as a result of employing a beam size that is smaller than the droplet ($d < D_0$), and (ii) plasma expansion from the illuminated droplet area, increasing the intersecting beam-plasma absorption area (see the following discussion in Sec. 4.3). Our results suggest that these effects compensate divergence in this $d < D_0$ case from the momentum scaling $P \sim D_0^2$ found in the $d > D_0$ case [30]. We emphasize here that the propulsion velocity U can be elegantly determined by $U = f(E_{\mathrm{od}}, D_0)$ with all data shown to collapse onto a single curve, see Fig. 4.8 in the Appendices. Such an independence of U on the beam size, when E_{od} and D_0 are given, however is not applicable to define the initial expansion rate $\dot{R}_0$, as we discuss in Sec. 4.2.2.c.

4.2.2.c   *Expansion dynamics of liquid tin droplets*

The ns-laser-induced expansion dynamics of liquid tin microdroplets has been studied previously in Refs. [14, 15, 17, 22, 24]. As discussed in Sec. 4.1, these works established how the radial trajectory $R(t)$ can be well described on a microsecond timescale by fluid-dynamics models in analogy to a droplet-pillar impact case that considers incompressible flow. After a rapid radial acceleration due to the impulse imparted by the impact, the droplet primarily deforms into a thin sheet delimited by a rim. The radial expansion hence undergoes an initial laser-driven acceleration and a subsequent deceleration due to the surface tension. In this way, the radius of the sheet increases, at an initial expansion rate of $\dot{R}_0$, reaches a maximum radius and then contracts. The maximum sheet size and the expansion trajectory $R(t)$ are determined by the deformation Weber number $\mathrm{We}_d = \rho D_0 \dot{R}_0^2 / \sigma$ with the liquid density $\rho = 6900\,\mathrm{kg\,m^{-3}}$ and the surface tension $\sigma = 0.55\,\mathrm{N/m}$ [16, 28]. In Fig. 4.4(a), the radius of the sheet $R(t)$
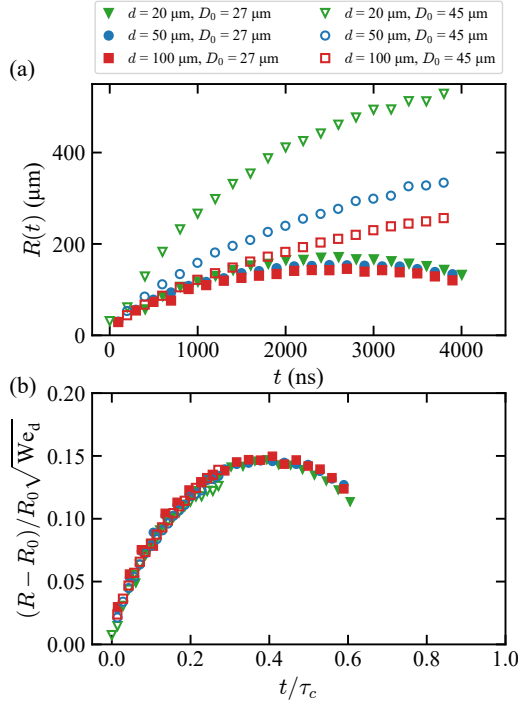
Figure 4.4: Sheet radius $R(t)$ from experiment as a function of time. (a) These experiments were performed using three beam diameters and two droplet diameters while keeping a constant propulsion velocity of 80 m/s. (b) Dimensionless sheet radius $(R - R_0)/R_0\sqrt{\mathrm{We_d}}$ as a function of the time relative to the capillary time τ_c. Open and solid markers indicate results for tin droplet diameters of 45 μm ($E_{\mathrm{od}} \approx$ 2.8 mJ) and 27 μm ($E_{\mathrm{od}} \approx 0.3$ mJ), respectively.

as a function of time is plotted for several combinations E, d and D_0, which all lead to the same propulsion velocity of $U = 80$ m/s. We choose data sets with the same U in order to discuss the origin of different expansion-to-propulsion ratios. Our data clearly illustrates (i) the initial radial expansion of the sheet and (ii) the effect of the surface tension that causes the gradual decrease of the expansion rate leading to the observation of an apex radius and a subsequent decrease of $R(t)$.

Figure 4.4(b) presents the dimensionless sheet radius $(R - R_0)R_0^{-1}\mathrm{We_d}^{-1/2}$ following Villermaux *et al.* [24], using the deformation Weber number $\mathrm{We_d}$ [17] as a function of the scaled time t/τ_c. Considering the droplet sizes used in the experiments (27 μm

and 45 μm), we obtain capillary times of 6.5 μs and 14 μs[3], respectively. Figure 4.4(b) shows that all the data collapse onto a single curve upon use of the scaled parameters. Such a collapse is consistent with the findings reported in Refs. [14, 21, 24].

As mentioned above, the initial expansion rate $\dot{R}_0$ has been identified as a crucial variable to characterize the fluid dynamic response that dictates the radial expansion. Therefore, we limit our analysis here to $\dot{R}_0$, which is obtained by a linear fit to the $R(t)$ data up $t = 300$ ns. In analogy to $U(E_{\mathrm{od}}, D_0)$ in Eq. (4.2), we first seek an expression of the form $\dot{R}_0 = f(E_{\mathrm{od}}, D_0)$. A quantitative study of the response of a droplet to laser impact for various laser parameters, but keeping U constant (see Fig. 4.4 and also the Appendices) shows that unlike the propulsion speed U, there is an additional, explicit dependence of $\dot{R}_0$ on the beam size d and, thus, $\dot{R}_0 = f(E_{\mathrm{od}}, D_0)$ is not complete. As predicted in Ref. [14], experiments performed using a tighter focused beam result in a larger $\dot{R}_0$. This effect can be seen in Fig. 4.4(a) by comparing the data obtained by using beam sizes $d^{\triangledown} = 20$ μm and $d^{\square} = 45$ μm, where $\dot{R}_0^{\triangledown} > \dot{R}_0^{\square}$ for equal U.

The nontrivial dependence of $\dot{R}_0$ on the laser beam size d and its relevance to explain the fluid dynamic response inspired us to numerically investigate the plasma pressure and its spatial profile at the droplet surface. In the next section, we will discuss the precise way in which momentum is transferred at the plasma-droplet interface through the use of radiation-hydrodynamic simulations.

4.3   Simulation

4.3.1   Code description

We have performed simulations of the laser-droplet interaction and subsequent droplet deformation and expansion using the two-dimensional (2D) radiation-hydrodynamic RALEF (Radiation Arbitrary Lagrangian-Eulerian Fluid dynamics) code [83, 84]. The code was originally developed to model high-temperature laser-plasma experiments conducted at GSI Darmstadt [85, 86]. In more recent times, however, the application domain of the code has shifted to the modeling of laser-driven tin plasmas in the context of EUV light sources for nanolithography [30, 55, 75, 87–89].

The hydrodynamic module of RALEF-2D is based on an upgraded version of the 2D CAVEAT code developed at Los Alamos National Laboratory [90]. The

---

[3]In the published work [Physical Review Research **4**, 013142 (2022)] that correspond to this Chapter, these two values for the capillary time for $D_0 = 27$ and 45 μm were wrongly written. These values are corrected now in this Chapter. We note that in the published work, the capillary time τ_c used in the relevant Fig. 4.4 followed the correct values (i.e., 6.5 μs and 14 μs for $D_0 = 27$ μm and 45 μm, respectively).
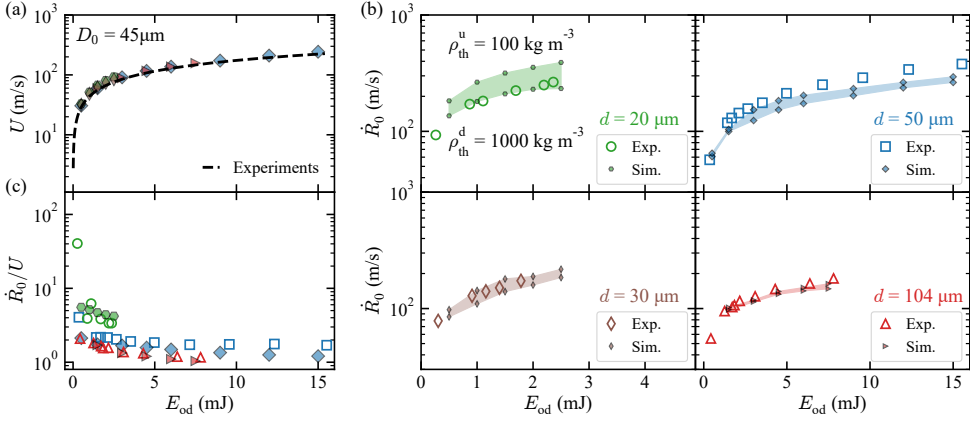
Figure 4.5: Comparison between experiments and simulations. In the $D_0 = 45$ μm case, the filled and empty markers represent the simulation and experimental results, respectively. Graphs of (a) the propulsion velocity, (b) the initial radial velocity and (c) the ratio $\dot{R}_0/U$ as a function of E_{od}. In (a) the dashed line represents the fit of the experimental data presented in Fig. 4.8(b). The shaded areas in panel (b) present the estimated $\dot{R}_0$ ranges using RALEF-2D, where the upper and lower limits correspond to the values calculated using density thresholds of 100 and 1000 kg m^{-3}, respectively.

code solves the single-fluid single-temperature hydrodynamic equations on a structured quadrilateral mesh using a second-order Godunov-type scheme, see Ref. [74] for more details. Algorithms for thermal conduction and radiation transport have been implemented using the symmetric semi-implicit method with respect to time discretization [91, 92]. Energy transport via thermal radiation is described by the quasi-static LTE (local thermodynamic equilibrium) radiation transport equation [75], and its solution is obtained using the method of short characteristics [93]. The angular dependence of the radiation intensity is modelled using the S_n quadrature method with $n = 6$ [94]. In order to obtain a solution of the LTE radiation transfer equation, one must have information on the radiative properties, i.e., the *spectral absorption coefficients* of the plasma. These data were generated with the THERMOS code [95, 96] and are imported into RALEF-2D in tabular format. For a given density-temperature (ρ, T) pair, the THERMOS code solves the system of collisional-radiative level population equations (in steady-state equilibrium) from which the spectral absorption coefficients are obtained. These data are discretized into 28 spectral groups for use in the simulations. The equation-of-state (EOS) of tin was obtained from the Frankfurt EOS (FEOS) package [97] which is based on the original QEOS model [98] and is an extension of the MPQeos code [99]. A very attractive feature of the FEOS model is its ability to model the low-temperature liquid-gas phase coexistence regions, which is enabled through

fully-equilibrium calculations with Maxwell's construction in the two-phase region. We note that the code does not take into account the effects of surface tension, whose influence during the early expansion phase is negligible considering that $\tau_i \ll \tau_c$.

We performed two sets of simulations for spherical tin droplets having diameters $D_0 = 27\,\mu$m and $45\,\mu$m. Our simulations were performed in the axisymmetric (z, r) geometry, where the symmetry axis of the tin sheet coincides with the laser propagation direction and passes through the center of the initially spherical droplet. As detailed in Ref. [30], we construct a polar coordinate system with its origin at the initial position of the droplet center. We adopted a detailed mesh structure of 1 mm radius exhibiting 360 zones over the π interval of the polar angle θ (defined with respect to the z axis pointing toward the incoming laser direction, see Fig. 4.1(c) and Ref. [30]). The mesh is progressively refined towards the initial droplet surface such that the thickness of the outermost cell is approximately 10 nm. The initial density of the liquid tin targets was set to $\rho_0 = 6900$ kg m^{-3}. The region outside the droplet was filled with a low-density tin vapour having $\rho = 10^{-7}$ kg m^{-3}. In the simulations, we employed a $\lambda = 1064$ nm laser pulse with a Gaussian temporal profile of $\tau_p = 10$ ns (FWHM). For both droplet diameter cases, simulations were performed with Gaussian laser beams with FWHM diameters $d = 20$, 30, 50 and $100\,\mu$m. The laser beam employed in the simulations was unpolarized. Laser light propagation and absorption in the plasma was treated using a hybrid model accounting for the effects of laser reflection and refraction in the corona of plasma [100]. The simulations were run up to a time $t_f = 300$ ns, where the center-of-mass speed has become insensitive to the choice of t_f. We note here that we do not adjust any parameters within our simulations to reproduce the experimental observations.
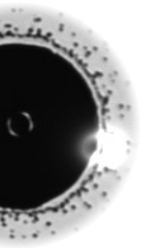
4.3.2 Simulation results

4.3.2.a Numerical validation: droplet propulsion and the expansion speed

In this Section, we will validate our simulations by comparing the propulsion speed U and the radial expansion rate $\dot{R}_0$ from RALEF-2D to the values determined in our experiments. The determination of U from the RALEF-2D simulations is straightforward and follows that outlined in Ref. [30]. This quantity is defined as the velocity of the center-of-mass (comprising all material having a density greater than 1000 kg m^{-3}) 300 ns after the laser pulse is switched on in the simulations. In Fig. 4.5(a) we present the U values as a function of E_{od}. The black dashed line corresponds to a fit of Eq. (4.2) (with $\alpha = 0.6$) to all the obtained experimental data with a droplet size

$D_0 = 45\ \mu$m (see Fig. 4.8 in the Appendices). The symbols represent the RALEF-2D predictions for laser beam diameters $d = 20$ (green hexagons), 30 (brown diamonds), 50 (blue squares) and 100 (red triangles) μm, respectively. The simulated data clearly follows the power-law dependence established in the experimental data.

The evaluation of the radial expansion velocity $\dot{R}_0$ from the RALEF-2D simulations is more complicated than that of U, mainly due to the difficulties in defining the liquid density at the boundary of the droplet and therefore $R(t)$ over time. From the simulations we extracted the radius that corresponds a density of (i) $\rho_{th}^u = 100$ kg m^{-3} and (ii) $\rho_{th}^d = 1000$ kg m^{-3}. We extracted the value of $R(t)$ every 10 ns within the time interval $100 \leq t \leq 300$ ns. We then fit a linear function to the $R(t)$ data, from which $\dot{R}_0$ was obtained.
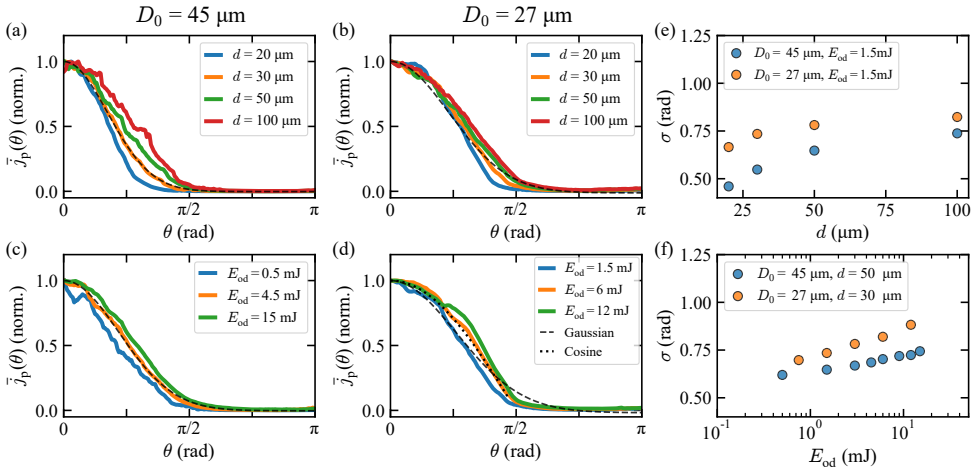

Figure 4.6: Normalized pressure impulse at the surface of a tin droplet extracted from our RALEF-2D simulations. Graphs in panels (a)-(b) present results considering a constant $E_{od} = 1.5$ mJ and four beam sizes while the results in panels (c)-(d) consider constant beam sizes of $d = 50\ \mu$m in (c) and $d = 30\ \mu$m in (d) and three energy-on-droplet values. The simulations were performed for two droplet sizes $D_0 = 27$ and 45 μm. The dashed lines in (a)-(d) illustrate Gaussian fits that enable characterizing the angular size σ. For comparison purposes, the dotted line in (d) shows a fit to a cosine function. Graphs of the angular size σ extracted from the pressure impulse profiles as a function of the d and E_{od}, are shown in (e) and (f), respectively.

In Fig. 4.5(b) we plot the experimental observations and RALEF-2D predictions for $\dot{R}_0$ as a function of E_{od}. The upper bound $\dot{R}_0$ simulated data correspond to a $\rho_{th}^u = 100$ kg m^{-3} reference density and the lower bound data points correspond to $\rho_{th}^d = 1000$ kg m^{-3}. It is clear that the largest spread in simulated $\dot{R}_0$ values is attributed to the $d = 20\ \mu$m case, where best agreement with experimental data can be found for

the $\rho_{th}^d = 1000$ kg m^{-3} reference density. With increasing beam diameter, this spread is observed to decrease. An interesting behaviour is observed for the $d = 50\,\mu$m case where the experimental data predicts a higher radial expansion velocity than both reference densities. Overall, our simulation results of U and $\dot{R}_0$ are in good to excellent agreement with our experimental findings, as shown in Figs. 4.5(a)-(b). Moreover, the $\dot{R}_0/U$ ratios in panel (c), calculated for several example cases, are also in good agreement with the experiments considering the reference density $\rho_{th}^d = 1000$ kg m^{-3}. We note that this ratio is larger than one in all instances. This good agreement validates the capability of RALEF-2D in simulating the laser-droplet impact under the current numerical settings, which emulate the experimental conditions in this study. Next, we will present numerical results on the pressure profile.

4.3.2.b   *Pressure impulse distributions*

As discussed above, the recoil pressure exerted by the expanding plasma imparts forward momentum, P, to the droplet and hence sets the propulsion and expansion behavior. The plasma pressure is related to the forward momentum obtained by the target through

$$P = \int_0^{t_f} \iint_A p_a(t, \theta)\, \mathbf{e}_z \cdot d\mathbf{A}\, dt, \tag{4.3}$$

where $p_a(t, \theta)$ is the plasma pressure at the droplet surface as a function of time t and polar coordinate θ [14]. We define the local impulse as the time integral of the local pressure $j_p(\theta) = \int_0^{t_f} p_a(t, \theta)dt$, which is therefore only a function of angle. This integration ends at 95 ns [45]. We note that 90% of the full pressure impulse is imparted within ~ 10 ns from the time at which the peak intensity of the laser pulse is achieved, which is set to 15 ns in this work. The momentum imparted to the droplet thus can be described by the spatial shape of $j_p(\theta)$ [45]. Figures 4.6(a)-4.6(d) illustrate profiles of the normalized pressure impulse $\bar{j}_p(\theta) = j_p(\theta)/j_p(0)$ at the droplet-plasma interface, where $j_p(0)$ corresponds to the pressure impulse at the droplet pole $\theta = 0°$. These profiles are associated with two droplet sizes, namely $D_0 = 45$ and 27 μm. We seek the dependence of $j_p(\theta)$ on the droplet size D_0, beam size d and energy-on-droplet E_{od}.

Figures 4.6(a) and 4.6(b) present $j_p(\theta)$ profiles for increasing beam sizes d, with a constant $E_{\text{od}} = 1.5$ mJ. The top panels illustrate how tighter laser foci lead to narrower pressure impulse distributions, e.g., see the blue curve in Fig. 4.6(a) with $d = 50\,\mu$m. This observation is expected as the ablation and the consequent plasma generation follow the local intensity of the incident beam [13, 101]. We also observe that the

irradiation of larger droplets, considering a constant beam size d, results in narrower impulse distributions, as shown for instance by comparing the blue curves in Figs. 4.6(a) and (b). The bottom panels (c) and (d) present graphs of $j_p(\theta)$ for increasing E_{od} values for a given beam size of $d = 20 \ \mu$m. Our data indicate that a higher E_{od} slightly broadens the pressure profile, creating a more uniform distribution. This is due to the faster expansion of the plasma (induced by the increased intensity),which wraps around the droplet, as was also reported in Refs. [30, 81].

We use the data shown in Figs. 4.6(a)-(d) to quantify the angular size of the pressure pulse at the droplet surface. We find that our data can be well described by a Gaussian distribution. This resemblance, along with the function employed in Gelderblom *et al.*, motivated us to fit a Gaussian function to our pressure curves as $j_p(\theta) = j_p(0) \exp(-\theta^2/(2\sigma^2))$ [14]. The fits provide the angular size σ (i.e. standard deviation) of the pressure distributions that we later use to calculate the size of the arc at the droplet surface $\sigma \times D_0$. Following Ref. [14], this angular size sets the late-time target morphology. We illustrate examples of these fits to the orange profiles as dashed lines in Figs. 4.6(a)-(d). Cosine-shaped pressure impulses, observed here for particularly large fluence cases in Fig. 4.6(d), constitute the limiting case in Ref. [14] projecting a flat momentum impulse distribution onto a spherical surface. Figures 4.6(e) and (f) show σ as a function of the beam size d and E_{od}, respectively. The data indicate wider pressure impulse profiles when using both a larger beam size and a higher energy-on-droplet, consistent with aforementioned observation in panels (a)-(d).

4.4 Discussion

Thus far, we have seen how varying the droplet diameter D_0, beam size d, and laser pulse energy E will influence the droplet expansion speed $\dot{R}_0$ and the propulsion speed U. The magnitudes of these speeds, and their ratio, provide valuable insight into the balance of kinetic energy channeled either to the radial deformation, $E_{k,d}$, or to accelerating the center-of-mass of the droplet, $E_{k,cm}$. As mentioned in the Introduction, in Ref. [14], the energy ratio $E_{k,d}/E_{k,cm}$ was identified as the pertinent quantity to describe the late-time evolution of the droplet morphology, e.g., at times $t \sim \tau_c \sim \mu$s. In Refs. [14, 17] direct estimates of the energy partitioning were retrieved from experimentally obtained velocities by using the relation $E_{k,d}/E_{k,cm} \propto \dot{R}_0^2/U^2$ (also see the Appendices). The calculation of the prefactors that accompany this power law relation depends on the assumptions made about the late-time geometry of the target. For instance, a 1/2 prefactor results from considering a thin disk, i.e. a sheet of
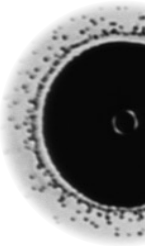
uniform thickness [14]. A 1/3 prefactor was obtained in Ref. [17] assuming a thickness
$h \sim 1/(rt)$, following Ref. [24]. In reality, the sheet thickness changes in a more
complex manner with the radial coordinate (over time) [16]. Even with a validated
model of the late-time sheet thickness for the current case [16], no reliable predictions
for early-time morphology can be extrapolated from it and instead we use RALEF-2D
to determine the early-time kinetic energies and their ratios and compare the results
with the model from Ref. [14].

   In our simulations, the total kinetic energy of the liquid body is determined by the
sum of the discretized kinetic energies corresponding to each cell with a volume δV_i
and a velocity vector $\mathbf{u}_i$

$$E_k = \sum_i \frac{1}{2} \rho_i \, \delta V_i \mathbf{u}_i^2, \tag{4.4}$$

with the liquid body containing all tin with a density larger than $1000 \, \text{kg m}^{-3}$, i.e., the
reference density used for the center-of-mass speed U and expansion velocity $\dot{R}_0$ in
Sec. 4.3. Following Ref. [14], we identify the kinetic energy of the center-of-mass as

$$E_{k,cm} = \frac{1}{2} U^2 \left(\sum_i \rho_i \, \delta V_i \right), \tag{4.5}$$

also over a region with $\rho_i > 1000 \, \text{kg m}^{-3}$. Next, the *deformation kinetic energy* is
defined as the remaining kinetic energy obtained when subtracting $E_{k,cm}$ from E_k,
namely

$$E_{k,d} = E_k - E_{k,cm}. \tag{4.6}$$

The energy partitioning between the deformation and the propulsion of the droplet
can thus be quantified by $E_{k,d}/E_{k,cm}$. Although we have shown that U can be de-
scribed by a function that solely depends on E_{od} and D_0, $\dot{R}_0$ cannot, and is a function
of E_{od}, D_0 and d. Therefore, we initially assume here that the energy partition fol-
lows $E_{k,d}/E_{k,cm} = f(E_{od}, D_0, d)$. We further seek for a representative parameter that
incorporates these three variables to simplify the expression for $E_{k,d}/E_{k,cm}$.

   We first investigate the dependence of the energy partition on the beam-to-droplet
size ratio d/D_0, the only *a priori* known dimensionless length scale in our system.
Figure 4.7(a) shows $E_{k,d}/E_{k,cm}$ as a function of d/D_0, where data for two droplet
sizes and multiple E_{od} (color bars) are presented. The graph illustrates that more
tightly focused beams, with respect to the droplet size (i.e., smaller d/D_0), lead to a
higher kinetic energy channeled to deform the droplet, $E_{k,d}$, instead of propelling it.
This observation can be expected from Fig. 4.5(c) where $\dot{R}_0$ increasingly exceeds U
when ever-smaller beams are employed. However, the beam-to-droplet size ratio d/D_0
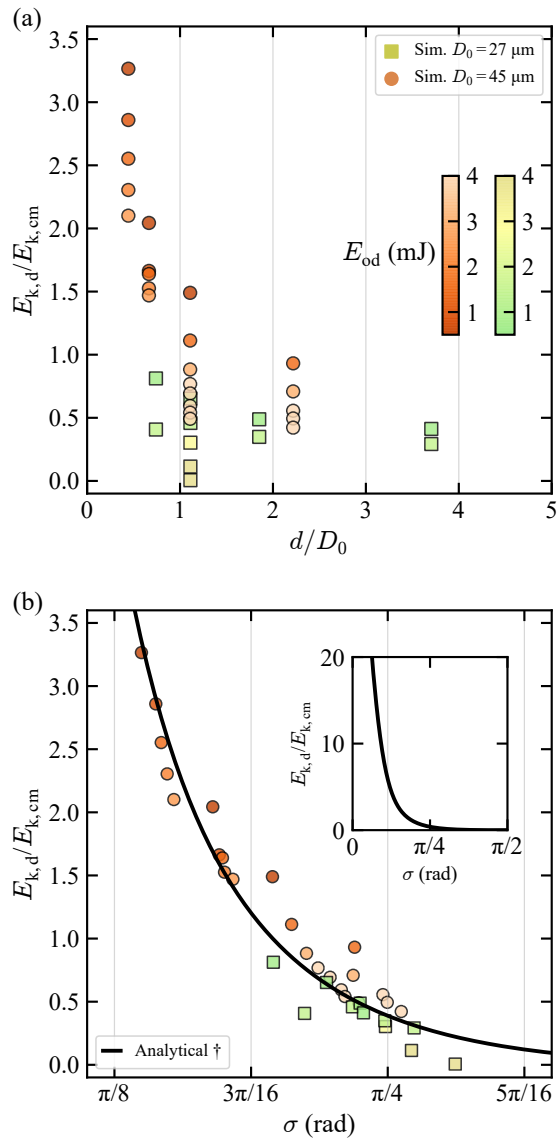
Figure 4.7: Simulated kinetic energy partition $E_{k,d}/E_{k,cm}$ as a function of (a) the size ratio d/D_0 and (b) the pressure impulse width σ. The black solid line † in (b) was calculated following the analytical expression proposed by Gelderblom *et al.* in Ref. [14].

cannot fully account for the effect of the E_{od} on the energy partition as illustrated in Fig. 4.7(a). Furthermore, it fails to capture the change in energy ratio comparing the two droplet sizes for any pulse energy. We thus conclude that d/D_0 is not the pertinent length scale for the problem at hand.

In Fig. 4.6, we describe the pressure impulse $j_p(\theta)$ using a Gaussian function, which provides an angle σ and hence a characteristic arc length σD_0 for each $d - D_0 - E_{od}$ combination. This length defines the actual width of the pressure field at the droplet surface. According to Figs. 4.6(e)-(f), for a given D_0, the width σD_0 increases with the size of the beam d and with the laser energy E_{od}. Therefore, the width of the pressure field σD_0 is a better choice of a characteristic length scale to determine the expansion response of the droplet as it comprises the effect of all experimental parameters.

Next, we describe the energy partition $E_{k,d}/E_{k,cm}$ as a function of σ, i.e. the ratio between the arc length of the pressure field and the droplet diameter $(\sigma D_0)/D_0 = \sigma$. Figure 4.7(b) presents $E_{k,d}/E_{k,cm}$ as a function of σ with the same data shown in panel (a). All the data fall onto a single curve, suggesting that σ is indeed the relevant dimensionless length scale, that simultaneously incorporates the effect of E_{od}, d and D_0 on the energy partition. In this way, we simplify the expression of the kinetic energy partitioning to: $E_{k,d}/E_{k,cm} = f(\sigma)$.

Reference [14] provides an analytical model that can predict the $E_{k,d}/E_{k,cm}$ ratio for any pressure impulse and studies in particular detail the response to a Gaussian-shaped pressure impulse. The close approximation of our $j_p(\theta)$ by a Gaussian function (see Fig. 4.6) hence enables our data to be directly compared to the results obtained from the fluid dynamic model using the very same definition of σ. This comparison is presented in Fig. 4.7(b), which shows an excellent agreement between our simulations and the model. We note that the most extreme cases, i.e. those with the largest σ values, correspond to scenarios where the dominant fraction of the initial droplet mass is ablated whereas the model assumes that a negligible mass fraction is ablated (for non-extreme cases this mass loss fraction is at the $\sim$10% level in line with Ref. [30]). At these large values of σ also the largest relative deviations between model and simulations are observed. These deviations should not be interpreted as a breakdown of the model, but instead as the limit of the range of validity of the current comparison. Considering the complexity of our RALEF-2D simulations, which include a plethora of physics aspects, the agreement shown between the simulation and the analytical model [14] is remarkable. This agreement validates the key model [14] assumptions of (i) an instantaneous pressure impulse causing an (ii) inviscid, (iii) incompressible flow. The assumption (i) is valid for the cases in the current work, where the liquid velocity field is established well before significant deformation occurs as $\tau_p \ll \tau_i$. The next model assumption (ii) of inviscid flow is valid as the typical Reynolds number

is of order Re $\sim 10\,000$. Finally, assumption (iii) on incompressibility is partially validated in the present study. The fluid dynamic response of a droplet is dominated by incompressible flow when the $\tau_p/\tau_a \gg 1$ (the St number) and $p_a/\rho c_s^2 \ll 1$ (the Ma number) [38, 45]. Here, $\tau_a = R_0/c_s$ is the acoustic time, which accounts for the time that an acoustic wave takes to travel half the droplet diameter at the speed of sound $c_s \sim 2500\,\text{m/s}$ [102]. In our current study, the pulse duration $\tau_p/\tau_a \approx 1\text{–}2$, which was shown in Ref. [38] to be sufficient to assure that the flow is dominated by compressible flow. The plasma pressure p_a differential is indicated by our simulations to be smaller, at $\sim 100\,\text{kbar}$, than the base pressure of liquid tin at $430\,\text{kbar}$, thus satisfying the condition $p_a/\rho c_s^2 < 1$ to a sufficient degree.

The level of agreement between our simulations and the analytical theory [14] suggests that approximating $j_p(\theta)$ by the Gaussian function is indeed an appropriate measure to characterize the pressure impulse profile in our context. More importantly, the agreement indicates that the combined effect of laser ablation and the dynamics of the plasma impacting droplet can be captured by a single dimensionless quantity σ that uniquely sets the energy partition, which in turn [14] determines the late-time response of the droplet target. The droplet response to laser impact can be accurately described by the incompressible hydrodynamic response of an initially undeformed droplet to an instant pressure impulse. These findings assist in the robust prediction of final target morphology in industrial sources of EUV light.

4.5   Conclusion

In this paper, we investigate the early hydrodynamic response of liquid tin microdroplets upon nanosecond laser irradiation. Both experimental and numerical methods were employed to explore and understand the influence of the laser energy E, beam diameter d and droplet diameter D_0 on the laser-induced dynamics of tin droplets. Experimentally, we recorded the expansion and propulsion of tin droplets using stroboscopic microscopy, which aids to determine the propulsion speed U and the initial radial expansion rate $\dot{R}_0$. Our results show that the irradiation of smaller droplets, while keeping constant E and d, leads to flatter morphologies and faster expansion and propulsion velocities, when compared to their larger counterparts. Moreover, we show how the propulsion velocity can be accurately described — for a large set of experiments with different E, d and D_0 combinations — using a function of $U = f\left(D_0, E_{\text{od}}\right)$ that was introduced in Ref. [13] for a single D_0. Our results also reveal a more complex behaviour of the radial expansion rate with an explicit dependence on the beam size $\dot{R}_0 = f\left(D_0, E, d\right)$.
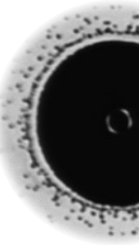
To be able to predict and fully understand the dependence of $\dot{R}_0$ on E, d and D_0 and its balance with U, we employed radiation-hydrodynamic simulations using RALEF-2D. The comparison between the experimental and numerical U and $\dot{R}_0$ results shows good agreement, which supports the validity of RALEF-2D in this context. In order to quantify the kinetic energy partition channeled to deform or propel laser-irradiated tin droplets, we retrieved the spatial distribution of the plasma-driven pressure $\bar{j}_p(\theta)$ at the droplet-plasma interface from our simulation. We found that $\bar{j}_p(\theta)$ profiles can be well approximated by a Gaussian function, from which we identify a dimensionless length scale σ to characterize the width of the pressure field.

The unique combination of experiments and simulations used here reveals that σ can be used as the sole relevant parameter to extract the kinetic energy partition $E_{k,d}/E_{k,cm}$ that further determines the target morphology on a microsecond timescale. Our description of the energy partition $E_{k,d}/E_{k,cm} = f(\sigma)$ using radiation-hydrodynamics modelling is in excellent correspondence with the generalized fluid-dynamics model of instantaneous pressure-driven droplet dynamics proposed by Gelderblom *et al.* [14]. These findings support the separation of characteristic timescales, reconciling the generation of the laser-driven pressure impulse (tens of nanoseconds) and the early hydrodynamic deformation during the inertial time τ_i (hundreds of nanoseconds). Following the conclusions from the here validated theoretical work [14], an optimized scheme for deforming a droplet without losing energy to propulsion is to employ the tightest possible laser focus. Naturally, any gains from such a scheme need to be balanced against increases in sensitivity to laser-to-droplet alignment as is elucidated in, e.g., Refs. [31, 59]. Furthermore, the final morphology, which is uniquely set by the choice of σ [14], may impact the obtainable conversion efficiency of drive laser light into in-band EUV photons. Our results thus contribute to further the development of laser-driven plasma sources for EUV nanolithography by aiding to accurately attain the desirable features and morphology of tin targets.
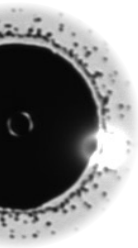
Appendix I: Scaling of U and $\dot{R}_0$ with laser energy on droplet

Figure 4.8 illustrates several panels with graphs of experimental U, $\dot{R}_0$ and $\dot{R}_0/U$ data as a function of the E_{od} for two different droplet diameters, namely $D_0 = 27\,\mu m$ (top panels) and $45\,\mu m$ (bottom panels). In Figs. 4.8(a) and (b), we present a large set of experimental $U - E_{\mathrm{od}}$ curves for several beam diameters and two different droplet diameters. We find that the experimental data collapse onto a single $U - E_{\mathrm{od}}$ curve for a given droplet size. The black dashed lines illustrates fits to Eq. (4.2), which shows good agreement with the experimental observations when considering $\alpha = 0.6$ and $K'_U = 41\ \mathrm{m\,s^{-1}\ (mJ)^{-0.6}}$. In Fig. 4.8(c) and (d), we present the radial velocity $\dot{R}_0$ as a function of the E_{od}. As a reference, we also plot the fits obtained in panels (a) and (b) to illustrate that the radial velocity is in most cases larger than the propulsion velocity. We also observe that the $\dot{R}_0 - E_{\mathrm{od}}$ curves do not overlap for the whole E_{od} range. Considering a constant D_0 and E_{od}, the laser-induced radial velocity is larger when using tightly focused beam than a loosely focused beam, see for instance the data
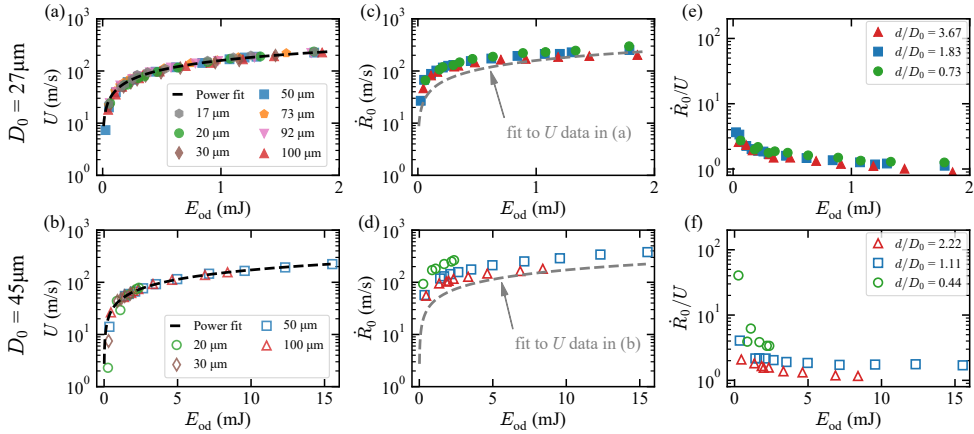
Figure 4.8: Experimental $\dot{R}_0$ and U for a large variety of $d - D_0 - E_{\mathrm{od}}$ combinations. Graphs of the experimental propulsion velocity U, (a) and (b), and the radial velocity $\dot{R}_0$, (c) and (d), as a function of the energy-on-droplet E_{od}. The graphs on the top and bottom rows present the results that correspond to experiments carried out using two droplet diameters, namely $D_0 = 27\,\mu m$ (filled markers) and 45 μm (empty markers), respectively. Different colors represent the data acquired using different beam diameters, ranging from 17 μm up to 100 μm. The dashed lines are fits to the experimental data in (a) and (b) using Eq. (4.2). (e)-(f) Ratio between the radial velocity and propulsion velocity as a function of the energy-on-droplet. Different colors represent data for several d/D_0 ratios as shown in the legend, which are consistent with the colors assigned to the beam diameters.

markers near $E_{od} = 2$ mJ in panels (c) and (d). We also note here that the differences in $\dot{R}_0$ are more pronounced for the $D_0 = 45$ μm case. These observations confirm that the expansion velocity depends not only on D_0 and E_{od}, like U, but also depends on the beam size d, as $\dot{R}_0 = f(D_0, d, E_{od})$, see Sec. 4.3.2.a. Consequently, overall the $\dot{R}_0/U$ ratios are larger for a larger droplet size as shown in panels (e) and (f).

Appendix II: Kinetic energy partition versus velocity ratio

Figure 4.9 presents the energy partition $E_{k,d}/E_{k,cm}$ obtained by RALEF-2D as a function of the velocity ratio $\dot{R}_0/U$. By assuming that the droplet ultimately deforms into a sheet with an uniform thickness, i.e. the velocity field of the liquid in the sheet linearly follows $u \sim r\dot{R}/R(t)$, Gelderblom *et al.* [14] elucidates an instantaneous energy partition for a well-deformed sheet as $E_{k,d}/E_{k,cm}(t) = \dot{R}(t)^2/(2U^2)$. Extrapolating this equation to the onset of the impact at $t = 0$ gives

$$\frac{E_{k,d}}{E_{k,cm}} = \frac{\dot{R}_0^2}{2U^2}. \tag{4.7}$$

Equation (4.7) is plotted as a dashed line in Fig. 4.9. It is shown that with a larger $\dot{R}_0/U$, Eq. (4.7) increasingly overestimates the energy partition from our simulation. This discrepancy might in part be due to a more curved sheet shape when employing a tighter laser beam (see Fig. 4.2 and the discussion in Sec. 4.2.1), leading to a larger
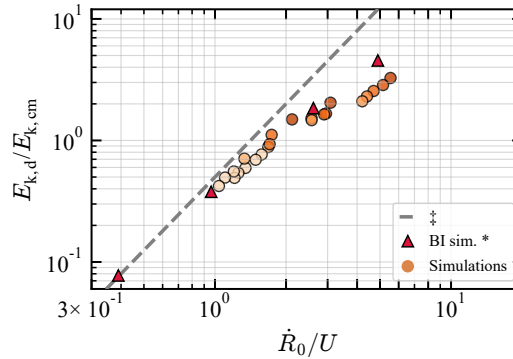
Figure 4.9: Simulated kinetic energy partition $E_{k,d}/E_{k,cm}$ as a function of the velocity ratio $\dot{R}_0/U$. The simulation data shown here as orange circles corresponds to that of Fig. 4.7. The dashed line ‡ were calculated using Eq. (4.7), as proposed by Gelderblom *et al.* in Ref. [14]. The red triangles are the boundary integral (BI) simulations extracted also from Ref. [14].

deviation of the target morphology from the assumption of a uniform sheet. We also plot the results of boundary integral (BI) simulations extracted from Ref. [14] (red triangles).
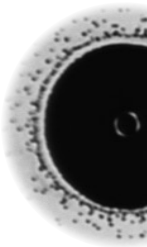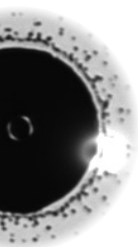
CHAPTER 5

SPEED OF FRAGMENTS EJECTED BY AN EXPANDING LIQUID TIN SHEET

Bo Liu, Javier Hernandez-Rueda, Hanneke Gelderblom, and Oscar O. Versolato

We experimentally investigate the speed of fragments produced by ligament breakup in the laser-induced deformation of tin microdroplets into axisymmetric sheets. The experiments were carried out covering a wide range of droplet diameters and laser-pulse energies. In addition to fragments produced by end-pinching, we also observe fragments shed via Rayleigh-Plateau breakup of long ligaments at late times. A double-frame backlit camera was used to obtain the speeds of the fragments u_f and the time of their detachment t_d. We show that by normalizing u_f to the initial expansion speed of the sheet $\dot{R}_0$, all data collapse onto a single, universal curve that is a function of the dimensionless time t_d/τ_c only, where τ_c is the capillary time. This universal curve is explicitly independent of the droplet's Weber number. The collapse of u_f is supported by energy conservation arguments. Our findings enable the prediction of the instantaneous speed and position of the fragments shed from liquid tin targets used in state-of-the-art extreme ultraviolet nanolithography, facilitating the design of effective mitigation strategies against microparticulate debris.

5.1 Introduction

Liquid fragmentation caused by the impact of droplets is a ubiquitous process in nature that is important in numerous industrial applications. In agriculture, the efficiency of the uptake of nutrients by the leaves of a plant is affected by the splashing that originates from the impact of droplets in pesticide sprays [103]. In the case of airborne-transmitted diseases, fragments of liquid that originate from the respiratory system of animals can travel a long distance and transport biological agents [21, 104, 105]. In the semiconductor industry, splashing and fragmentation processes also play a key role [17, 82]. Modern sources of extreme ultraviolet (EUV) light for nanolithography use liquid tin to generate EUV light with a wavelength centered at 13.5 nm in a two-step process [43, 57, 58, 64, 65]. In the first step, a ns-laser prepulse illuminates a spherical microdroplet of liquid tin, inducing its propulsion and deformation into an expanded target consisting of a thin sheet and a rim that bounds the perimeter of the sheet [15, 16]. This target is subsequently irradiated by a second laser main-pulse to produce a hot and dense plasma that emits EUV light [55, 66–68, 70]. The droplet deformation driven by the prepulse also results in the generation of micron-sized fragment "debris", which may drastically reduce the lifetime of the collection optics within the commercial sources of EUV light [12, 17, 31, 42]. Therefore, a thorough understanding of the shedding mechanism of fragmentation in the context of laser-pulse impact on a droplet is highly relevant to optimize the performance and to extend the lifetime of EUV sources.

To better understand the physics that dictates the fragmentation of tin droplets after prepulse irradiation, we draw on analogies to canonical cases of droplets impacting onto solid substrates. Such analogies have been made in prior experimental work by Klein *et al.* [17, 28] and in a theoretical study by Gelderblom *et al.* [14], in order to describe the deformation and fragmentation of a sheet produced from a laser-pulse impacted droplet. Upon impact, a droplet deforms into a thin sheet, bounded by a thicker rim. The liquid contained in the sheet flows outward towards the periphery, progressively increasing the mass content of the bounding rim [24]. Due to the restoring force exerted by the surface tension, the rim continuously decelerates. On the other hand, the fluid particles on the sheet follow ballistic radial paths since there are only weak pressure gradients along the radial direction [21, 24]. Once coalesced with the decelerating rim, the velocity of the liquid flowing from the sheet suddenly decreases [24]. This rapid change in speed leads to an increase of the static pressure and to a loss of total energy [24]. In addition, the gradual deceleration of the rim leads to Rayleigh–Taylor (R-T) instabilities which, combined with the Rayleigh-Plateau (R-P) instabilities, cause azimutal undulations that ultimately aggregate into ligaments fed by the pressurized

liquid contained in the rim [17, 22, 24]. Finally, the ligaments break into fragments via ligament pinch-off. The produced fragments have a speed u_f which equals the speed of the corresponding ligament tip at one necking time prior to the pinch-off [21]. Overall, the fragmentation dynamics is the result of a complex interplay of local rim destabilization and flow in the sheet, set in motion by the impact of the droplet.

While splashing and fragmentation processes related to the impact of droplets on solids have been widely studied, it is surprising that only a few studies deal with the velocity of the produced fragments. Riboux *et al.* [26, 27] and Thoroddsen *et al.* [35] investigated the speed of fragments produced by the impact of mm-sized water droplets on a large solid surface. These works however focus on the initial stage of the fragment's behaviour shortly after impact at $t \ll t_i$, where $t_i = D_0/U$ is the inertial time with D_0 and U the diameter and the initial speed of the impacting droplet, respectively. In these cases, the distribution of fragment size and velocity are influenced by the capillary force and the viscous stress at the lamella in contact with the surface. These effects on the fragmentation process are expected to depend on the area of the solid on which the droplet impacts. Inspired by the splashing effects occurring close to the edge of plant leaves, Wang *et al.* [21] investigated the impact of mm-sized droplets on a pillar with a diameter similar to the droplets, studying the speeds of fragments as shed from the growing and retracting sheet. They found experimental evidence of a self-similar behavior of the speed of fragments, later supported by an analytical work in Ref. [79]. In the case of tin microdroplets irradiated with a laser pulse, it is the violent expansion of the laser-produced plasma near the droplet surface that provides a recoil pressure with a magnitude of 100 kbar [13, 14, 30, 106], which results in an effectively instantaneous ($\sim 10\,\text{ns} \ll t_i$) momentum kick leading to propulsion and expansion velocities on the order of 100 m/s [13, 30, 106]. In this extreme context, where time- and spatial dimensions significantly differ from those found in droplet-impact-on-solid cases, the interplay of the parameters that condition the speed of fragments is not obvious. The absence of a rigid surface implies that there is no solid contact - there is no impactor. This difference in the boundary conditions will influence the fluid dynamic response of the droplet [14], modifying the evolution of the sheet and its thickness [14–16, 20]. Furthermore, different magnitudes of initial perturbations, when comparing water and tin laser-impacted droplet systems, appear to induce disparities in the capillary instabilities that govern the breakup of the sheet [17, 107]. The influence of the amplitude of such initial perturbations on the speed of shed fragments is unknown. Therefore, there is a need for a systematic study of the speed of fragments induced by a laser impact on tin microdroplets.

In this manuscript, we experimentally investigate the speed u_f of fragments that result from the laser-induced deformation of tin microdroplets. We include droplets

with different diameters D_0 impinged by laser pulses of various energies E_p, which enables us to cover a wide range of Weber numbers and relevant time scales. We employ stroboscopic microscopy using a double-frame camera to capture the ballistic trajectory of fragments shed from ligaments protruding from the rim. Our imaging systems, with the optical resolution enhanced with respect to our previous studies, allow observations of fragments shed from ligaments not only by the canonical end-pinching mode, but also by a R-P instability occurring on those long ligaments that appear at later moments. Our benchmark studies of the dynamics of the sheet's expansion and contraction underscore the validity of using a global deformation Weber number to characterize these dynamics following Ref. [17]. Next, we present the results of our measurements of fragment speed u_f and the dependence thereof on detachment time t_d and Weber number. The speed of the fragments is shown to always exceed the instantaneous expansion velocity of the rim $\dot{R}_r$, where the difference $u_f - \dot{R}_r$ increases with time, starting at zero at the onset of the impact, i.e., $u_f \to \dot{R}_r$ at $t_d \to 0$. Furthermore, we show that normalizing u_f to the initial expansion speed $\dot{R}_0$ provides a universal curve $u_f/\dot{R}_0$ that is a function of the dimensionless time t_d/τ_c only and is independent of the Weber number. This self-similar behavior of u_f is demonstrated to be supported by energy conservation arguments, when considering the fraction of the total energy taken by the fragmentation channel.

5.2   Experimental setup

Figure 5.1(a) presents a schematic top-view of the experimental setup. A detailed description of the subsystems of the setup can be found in Refs. [13, 16]. The laser-tin interaction experiments are carried out in a vacuum chamber (10^{-7} mbar) with several ports that provide optical access. A tin reservoir is situated on top of the chamber and is kept at a constant temperature of $260\,°C$ that is well above the melting point of tin ($234\,°C$ [108]). From the reservoir, a droplet generator dispenses a vertically aligned train of liquid tin microdroplets, which retain the initial $260\,°C$ temperature during their in-vacuum flight with liquid density $\rho = 7000$ kg/m^3, and surface tension $\sigma = 0.54$ N/m, and dynamic viscosity $\mu = 1.8 \times 10^{-3}$ Pa s [109]. In the experiments, we systematically investigate droplets with five diameters $D_0 = 27, 34, 39, 43$ and $67\,\mu$m. A few millimeters above the center of the chamber, the droplet stream passes through a horizontal light sheet produced by a helium-neon (He-Ne) laser. The light scattered by the droplets is detected by a photo-multiplier tube (PMT), providing a signal with a repetition rate on the order of kHz. This signal is down-converted to 10 Hz, sent to a delay generator, and used to trigger the data acquisition and laser systems.
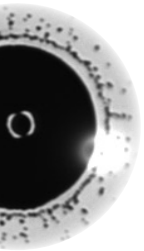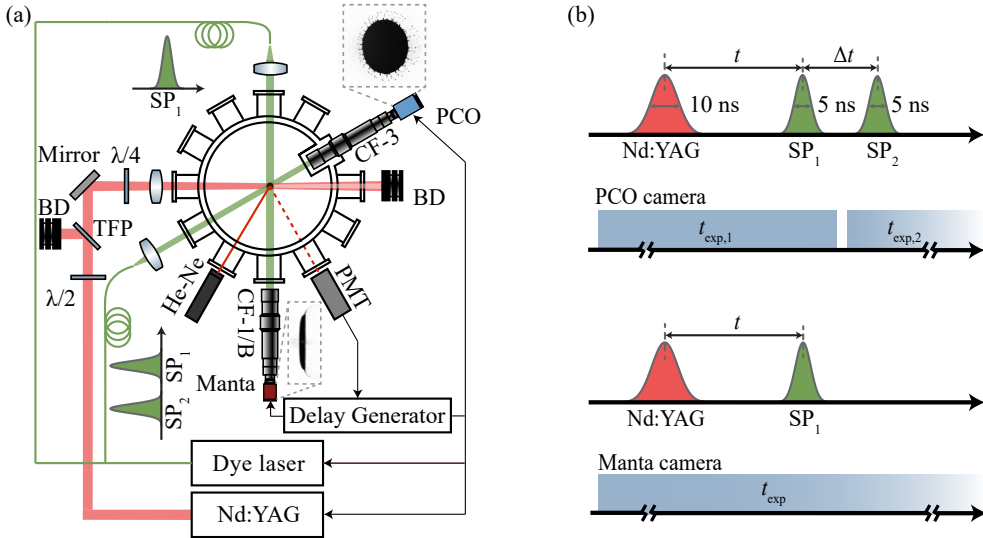
Figure 5.1: (a) Top-view schematic of the experimental setup including a vacuum chamber, synchronization & trigger systems, Nd:YAG drive laser and imaging systems. During the experiments, individual liquid tin microdroplets are irradiated by single ns-laser pulses. The energy of the laser pulse is controlled by using a half-wave plate and a thin-film-polarizer (TFP). The beam is dumped in a beam dump (BD). A quarter-wave plate is used before the final focusing lens to set a circular polarization. The imaging systems employ a double-frame CCD camera (PCO-4000) and a single-frame CCD camera (AVT Manta B145-G), which provide front- and side-view images of the expanding tin sheet at 30° and 90° with respect to the laser direction, respectively; see inset example front- and side-view shadowgraphy images as recorded by the PCO and Manta cameras. Two consecutive shadowgraphy probe pulses SP_1 and SP_2 are used as illumination sources for the front-view microscope, whereas a single pulse SP_1 is used for the side-view system. (b) Time sequence of the illumination pulses and their relation with the much longer exposure windows of the cameras. The time $t = 0$ sets the moment at which the drive laser pulse illuminates a droplet. At a time delay t, the first probe pulse SP_1 illuminates the expanding tin, overlapping with the exposure windows of both PCO cameras ($t_{exp, 1}$) and Manta (t_{exp}). After SP_1, the second probe pulse SP_2 is collected by the PCO camera at $t + \Delta t$, within its second exposure window $t_{exp, 2}$. The full temporal span of the target dynamics is obtained by scanning the time delay t.

Once a droplet reaches the center of the chamber, it is irradiated by a circularly polarized laser-pulse at 1064 nm with a pulse duration of 10 ns at full width at half maximum (FWHM). The laser pulses are delivered by a Nd:YAG laser system (Quanta-Ray, Spectra-Physics). The laser is focused to a Gaussian-shaped beam profile with a diameter $\approx 135 \mu$m (FWHM) at the surface of the droplets. We employed two different laser pulse energies for each droplet size, enabling us to cover a wide range of the relevant Weber number from approximately 1100 to 5500. In our experiments, the

Ohnesorge number $Oh = \mu/\sqrt{\rho\sigma D_0} \sim 10^{-3}$, which indicates a negligible influence of viscosity to the impact dynamics compared to the surface tension. The droplet capillary time scale $\tau_c = [\rho D_0^3/(6\sigma)]^{1/2}$ ranges from 6.5 to 25 μs. Detailed experimental conditions and parameters derived are summarized in Tab. 5.1 in the Appendices [1] [2].

The expansion and fragmentation dynamics of the sheet are inspected using a stroboscopic shadowgraphy imaging system, which consists of long-distance microscopes (K2 DistaMax, Infinity Photo-Optical) attached to CCD cameras. We record the droplet dynamics at 90° and 30° with respect to the laser propagation direction, as shown in Fig. 5.1(a), thus obtaining side- and front-view images, respectively. The imaging systems use incoherent light pulses at 560±10 nm with a pulse duration of 5 ns (FWHM) to provide the backlighting of the image. These probe pulses are generated within rhodamine 6G dye cells that are pumped with 532 nm pulsed laser light. The side-view system uses a CCD camera (Manta G145-B, AVT), which utilizes a CF-1/B objective (Infinity Photo-Optical) and captures single frames generated by a single shadowgraphy probe pulse SP_1 during the exposure of the camera t_{exp}. The front-view microscope is equipped with an CF-3 objective (Infinity Photo-Optical) with a shorter working distance for an increased resolution ($\sim 3\,\mu$m), and is set up at a distance of 110 mm from the target sheet. This microscope uses a camera (PCO-4000) capable of acquiring two consecutive frames of the same tin sheet with an effective minimum inter-frame delay of 280 ns. This double-frame camera captures two consecutive probe pulses SP_1 and SP_2 with a relative time delay Δt, which is tunable and typically ranges from 1 to 5 μs in the experiments. The time sequence of the probe pulses SP_1 and SP_2, and the corresponding exposure windows of the cameras, t_{exp}, $t_{exp,\,1}$, and $t_{exp,\,2}$, are shown in Fig. 5.1(b).

5.3   Ligament breakup

Figure 5.2 presents a set of high-resolution front-view images collected in this study that illustrate the sheet expansion at different time delays. In this specific case, a droplet with an initial diameter of $D_0 = 67\,\mu$m was irradiated using a laser pulse with an energy of $E_p = 7$ mJ. After laser excitation, the droplet is propelled along the laser propagation direction and deforms into an axisymmetric sheet, which expands, contracts, and fragments over time. The expansion and propulsion of the droplet are induced by the recoil pressure that results from the violent expansion of a laser-produced plasma

---

[1]The definition of the capillary time in this Chapter differs from that in Chapters 2 and 3 where $\tau_c = (\rho R_0^3/\sigma)^{1/2}$.

[2]In this Chapter, the characteristic length incorporated by the droplet Weber number is the diameter D_0, which is different from that used in Chapters 2 and 3 where the radius of the droplet R_0 was used.
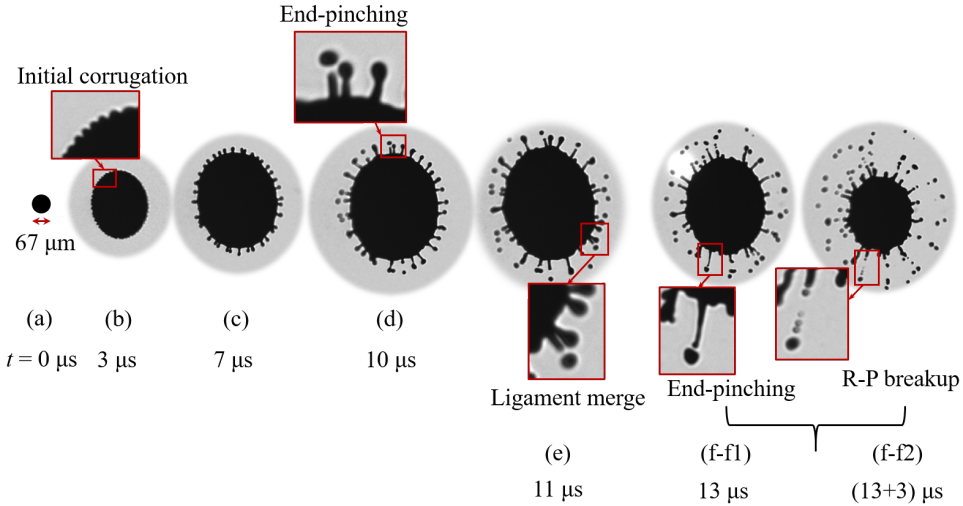
Figure 5.2: Front-view shadowgraphy images of the laser-induced tin sheet expansion and fragmentation at different time delays t, where $t = 0$ marks the onset of the ns-laser impact (each time delay, from panel (a) to (f-f1), corresponds to a different laser-droplet impact event). These images were obtained using droplets with a diameter of $D_0 = 67\,\mu$m and a laser pulse energy of $E_p = 7$ mJ. (a) Shadowgraphy image of a droplet right before laser exposure at $t = 0$, which serves as scale bar. (b) At $t = 3\,\mu$s, the droplet promptly expands into an axisymmetric sheet, with an initial expansion rate of $\dot{R}_0 \approx 38$ m/s. The inset provides a zoom of the emergent rim corrugations. (c) At $t = 7\,\mu$s, corrugations further develop into ligaments. (d) At $t = 10\,\mu$s, fragments are shed via end-pinching, further illustrated in the zoomed-in inset. (e) At $t = 11\,\mu$s, some ligaments merge together (also see zoomed-in inset). (f-f1) At $t = 13\,\mu$s, ligaments have grown to a typical length of several tens of micrometers. The inset illustrates the formation of a fragment that has just detached from the tip of a ligament with a length of $\approx 50\,\mu$m. (f-f2) The very same sheet shown in (f-f1), but 3 μs later. The inset shows the same ligament as in (f-f1) here breaking into several fragments via R-P instability.

(see, e.g., Refs. [13, 14, 16, 28]). As the sheet expands, a rim forms at the perimeter of the sheet, typically reaching a rim thickness of several micrometers, as reported in Refs. [15, 16]. Shortly after the formation of the rim, it destabilizes due to the combined effect of R-T and R-P instabilities that progressively enhance any initial perturbation on the rim to visible corrugations [22, 24].

Figure 5.2(b) taken at $t = 3\,\mu$s shows the initial corrugations a fraction of which [17, 23] further develop into ligaments that grow along the radial direction, as we illustrate in Fig. 5.2(c) at $t = 7\,\mu$s. Tin from the sheet continuously feeds the base of the ligaments, and thus these grow over time and ultimately break into small fragments. This breaking process is first dominated by *end-pinching* [21], shedding one droplet at a time as illustrated in Fig. 5.2(d) at $t = 10\,\mu$s. The inset shows an enlarged picture to exemplify

the end-pinching event. We observe that the onset of fragment generation decreases with increasing Weber number. A detailed analysis will feature in a forthcoming work. Later on, the ligaments merge [see panel (e)] and stretch, reaching lengths of several tens of micrometers. Figure 5.2(f-f1) at $t = 13\,\mu$s shows such a long ligament, with a length of approximately $50\,\mu$m. At this stage, the fragments are generated not only via end-pinching but also via *R-P breakup*, where multiple droplets are produced nearly simultaneously. Such a ligament breakup event is presented in the insets of (f-f1) and (f-f2), which illustrate the evolution of the exact same ligament with over a time interval $\Delta t = 3\,\mu$s as recorded by our double-frame camera. The ligament shown in the insets exhibits both an end-pinching event in (f-f1) and a R-P breakup in (f-f2).

Ligament breakup via R-P instability

To explain the occurrence of both the end-pinching and R-P breakup modes, we now discuss the relevant dynamics of the ligaments in more detail. Wang *et al.* [23], in their work on droplet-pillar impact, reported on ligaments breaking into fragments via end-pinching. They did not observe ligaments growing into long liquid jets required for the R-P breakup mode. The absence of this second mode of breakup was explained in the context of a critical Weber number We_c [23] which was originally introduced by Clanet *et al.* [110] for the flow out of a stationary orifice and was later refined by Ambravaneswaran *et al.* [111]. For droplet impact, at small ligament Weber numbers $\mathrm{We}_l = \rho u_l^2 w_l / \sigma < \mathrm{We}_c$, fragments form from ligaments solely via end-pinching; here u_l is the ligament speed in the co-moving frame following the expansion of the rim, and w_l is the mean diameter of the ligament [23]. For cases $\mathrm{We}_l > \mathrm{We}_c$, we expect the transition from end-pinching to jetting to occur. Here, long ligaments are formed which break into multiple droplets via R-P instabilities [23, 112].

In our experiments, we observe that end-pinching governs the ligament breakup for the dominant fraction of the studied time interval. At late times, however, we clearly see the formation of long ligaments which break up via R-P instabilities, i.e., a transition from end-pinching to jetting occurs. This transition is expected considering the analytical prediction from Ref. [23], which indicates a monotonic increase of We_l and a decrease of We_c with increasing t/τ_c, independent of the droplet's Weber number. As a corollary, the criterion of $\mathrm{We}_l \sim \mathrm{We}_c$ will be met at some constant time t/τ_c, which is analytically given as $t \approx 0.76\tau_c$, as can be derived from Ref. [23]. The transition to jetting appears to occur earlier in our experiments, cf. the example case shown in Figs. 5.2(f-f1, f-f2) where the R-P breakup related to jetting starts to become visible around $t \approx 13\,\mu$s $\approx 0.5\tau_c$. This observation of an earlier transition to jetting should be compared to the fact that our experiments exhibit an earlier apex

time t_{max}/τ_c of the sheet expansion (see below) and a faster expansion rate in the early stages. Therefore, the growth of We_l that is set by the sheet expansion will be faster and may thus be expected to reach the critical Weber number at an earlier time, in line with our observations of R-P breakup.
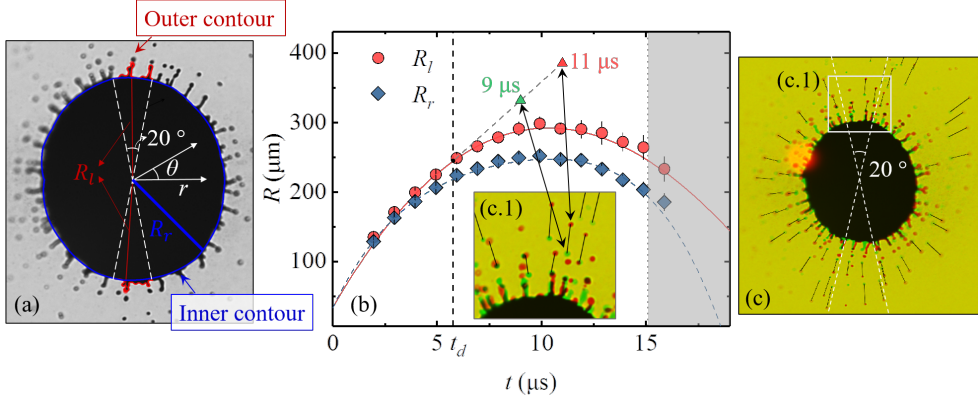

Figure 5.3: (a): Front-view shadowgraphy image (horizontally stretched to correct for the 30° observation angle) of an expanding tin sheet to illustrates the radial position of the sheet's rim R_r (blue inner contour) and the ligaments R_l (red outer contour). On the same image, we overlay a polar coordinate system (r, θ) with its origin at the center of the sheet. The picture was taken 8 μs after illuminating a $D_0 = 67\ \mu$m droplet with a $E_p = 20$ mJ laser pulse. We restrict the ligament and fragment analysis to the region (see the main text) comprising $\theta = 90° \pm 10°$ and $270° \pm 10°$ (dashed white lines). Within this azimuthal range, the longest ligaments originating from the top and bottom of the sheet are highlighted by their radial positions R_l. (b) Expansion trajectory of the ligaments from the top side R_l (red circles) and the rim R_r (blue diamonds) as a function of time. The solid curve presents a polynomial fit to the R_l data. The dashed line presents a polynomial fit to R_r data. The shaded area indicates the time regime $t > 0.6\tau_c (= 15.1\ \mu$s for $D_0 = 67\ \mu$m) that is excluded in the fitting as sheet breakup may hinder accurate tracking of R_r. (c) Post-processed shadowgraphy images captured at $t = 9$ and 11 μs by the double-frame camera, overlapped with respect to the sheet's center. Black pixels indicate overlap regions, where tin is present in both frames. Yellow pixels account for the background in the absence of tin. Green and red pixels indicate the presence of tin at either 9 or 11 μs, respectively. The black lines connecting the same green- and red-colored fragments illustrate their ballistic trajectory over the 2 μs time interval. The inset (c.1) shows a close-up of the ballistic trajectory of fragments. One example of a fragment trajectory is highlighted with its position at $t = 9$ and 11 μs, linked to the data markers in panel (b). The intersection between the fragment's trajectory in panel (b) and ligament expansion curve R_l is used to determine the detachment time t_d as indicated by a vertical line.

5.4   Sheet expansion

Figure 5.3(a) presents a front-view shadowgraphy image of an example sheet, which we use to illustrate the steps taken to determine the radius of the sheet's rim, R_r, and the radial position of the ligaments R_l. In this Section, we will first discuss the expansion trajectory of the rim radius R_r; the ligament radius R_l will be separately discussed in Sec. 5.5.2. The image in Fig. 5.3(a) was recorded 8 μs after illuminating a tin droplet ($D_0 = 67$ μm) with a laser pulse ($E_p = 20$ mJ). In line with the method used in Ref. [23], we first locate the outer contour that bounds the ligaments on the sheet perimeter [see the red lines in Fig. 5.3(a)]. We then locate the inner contour — which is retrieved as the baseline of the outer contour — as the position of the rim [see the blue lines in Fig. 5.3(a)]. The radius of the rim R_r is thus defined as the radial distance from the inner contour to the center of the sheet. Due to the axisymmetric geometry of the sheet, R_r does not show angular fluctuations: our data shows a small 2-4% variation over the relevant angular interval. We can then identify R_r as the average radius of the rim along the sheet's perimeter.

Figure 5.3(b) presents the rim radius R_r as a function of time for the same experimental conditions as used for panel (a). In Fig. 5.4, we further plot the results for $R_r(t)$
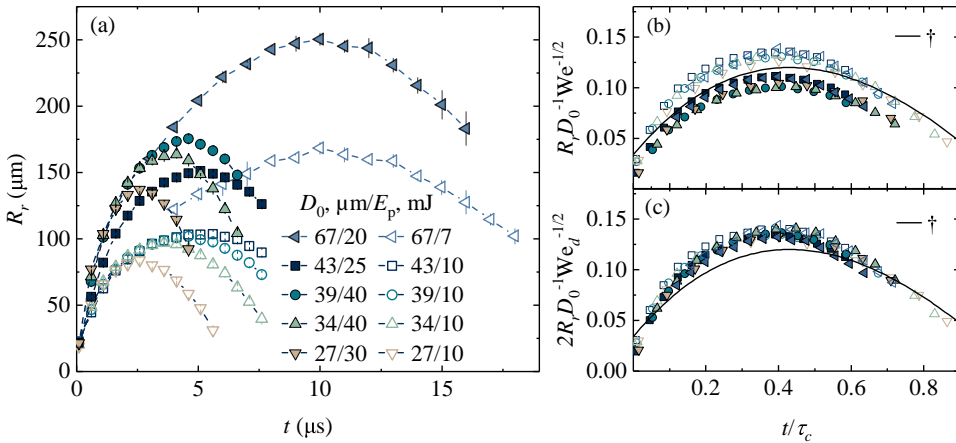
Figure 5.4: (a) Rim radius R_r as a function of time t for several D_0-E_p combinations. The error bars represent the standard deviation of the binned data. (b) Scaled rim radius, $R_r D_0^{-1} \mathrm{We}^{-1/2}$, as a function of the dimensionless time t/τ_c, with $\mathrm{We} = \rho U^2 D_0/\sigma$ and τ_c the capillary time. (c) Scaled rim radius $2R_r D_0^{-1} \mathrm{We}_d^{-1/2}$ as a function of t/τ_c, where the deformation Weber number is $\mathrm{We}_d = \rho \dot{R}_0^2 D_0/\sigma$. Solid lines in (b) and (c) show the solution for R_r from Ref. [79] (†). The error bars have been omitted both in (b) and (c) for better visibility.

for all data available as summarized in Tab. 5.1. For a given parameter set, we record a stroboscopic time series by performing a single laser experiment for each time delay t between laser impact and the illumination pulse (see Fig. 5.1). To ensure the reliability and repeatability of our results, we perform 20–50 impact events per parameter set for each time delay. The uncertainties shown in Fig. 5.3(b) and Fig. 5.4(a) equal the standard deviation of the measurement ensembles. In Fig. 5.4(a), for a fixed droplet size, we observe a faster initial expansion and a larger apex radius of the sheet R_{max} when increasing the laser energy. We also observe that the apex time t_{max} (at which the sheet reaches R_{max}) increases with the droplet size. After reaching R_{max}, the sheet starts to shrink due to the surface tension. In Ref. [23], a collapse of R_r onto a universal curve was reported, captured by the function $y = f(x)$ with variables $x = t/\tau_c$ and $y = R_r D_0^{-1} \mathrm{We}^{-1/2}$ where $\mathrm{We} = \rho U^2 D_0/\sigma$ is the Weber number with U the impact speed. An earlier work by Villermaux *et al.* [24] suggests a similar collapse of R_r by scaling $y = (R_r - R_0) D_0^{-1} \mathrm{We}^{-1/2}$ and $x = t/\tau_c$ which is equivalent to the collapse proposed in Ref. [23] when $\mathrm{We} \gg 1$, applicable in our cases (see Tab. 5.1). In line with Ref. [23], we plot the data of R_r upon rescaling in terms of the similarity variables in Fig. 5.4(b). The speed used in the Weber number in this panel is the center-of-mass speed U of the sheet along the laser pulse direction. This speed is determined by measuring the displacement of the sheet's center-of-mass over a finite time interval (typically over a few microseconds) using side-view images (for further details see Refs. [13, 28, 30]). It is evident that the normalization of t/τ_c successfully collapses the apex time t_{max}. However, normalizing rim radii by the impact Weber number results in a systematic disparity between the lower energies group (open symbols) and the higher energies (full symbols). Therefore, the center-of-mass speed does not characterize the expansion dynamics of the droplet for the full range of droplet sizes and pulse energies. In the case of droplet impact onto a pillar, the initial expansion rate of the droplet $\dot{R}_r(t = 0)$ (referred to as $\dot{R}_0$ hereafter) may deviate from the orthogonal speed of the impact U when varying the size of the drop relative to the pillar diameter [20, 21, 23, 24]. Villermaux *et al.* [24] analytically proposed and further experimentally confirmed that $\dot{R}_0 = U$ under their experimental conditions. Wang *et al.* in Ref. [79], however, observed a much larger deformation speed of $\dot{R}_0 \approx 2U$. The physics origin of the factor two difference between U and $\dot{R}_0$ in the latter case is not yet clear [79]. In case of laser-induced deformation, the correlation between the two orthogonal speeds $\dot{R}_0$ and U is well understood. This correlation is jointly determined by the droplet size, the laser pulse energy, and the beam profile and was shown to be captured by a single dimensionless pressure impulse width exerted by the plasma on the surface of the droplet (for details see [14, 106]). In brief, the expansion speed $\dot{R}_0$ monotonically increases with increasing U and is of the same

order: $\dot{R}_0 \sim U$. A narrower pressure impulse width leads to a larger ratio of $\dot{R}_0/U$ [14]. Typically, an increase in laser pulse energy leads to a reduction of $\dot{R}_0/U$ [17, 106]. In the current study, this ratio varies from 1.4 to 1.8 over the studied range of droplet sizes and pulse energies. Refs. [15, 17] further demonstrated that it is the expansion speed $\dot{R}_0$ that should be taken as the characteristic speed, defining the *deformation* Weber number $\mathrm{We}_d = \rho \dot{R}_0^2 D_0 / \sigma$ to describe the expansion trajectory of the sheet. In line with those works, Fig. 5.4(c) shows the same data in panel (b), but re-scaled as $2R_r D_0^{-1} \mathrm{We}_d^{-1/2}$; a factor 2 is added in the numerator to enable a comparison with Ref. [23, 79] where $\dot{R}_0/U \approx 2$ was observed. The speed of $\dot{R}_0$ used in panel (c) is determined by a linear fitting of R_r data (following Klein *et al.* [28]) using the first three time delays after the onset of the impact, typically up to 300 ns $\sim 1\,\mu$s. Figure 5.4(c) shows that the use of We_d successfully collapses all the data, demonstrating that $2R_r D_0^{-1} \mathrm{We}_d^{-1/2}$ can be described by a function depending solely on t/τ_c. For droplet impact on a pillar, such a function was provided analytically in Ref. [79] as $2R_r D_0^{-1} \mathrm{We}_d^{-1/2} = 0.15(t/\tau_c - 0.43)^3 - 0.4(t/\tau_c - 0.43)^2 + 0.12$. This function is depicted in the graph. Wang *et al.* [79] further used this solution of R_r to predict the speed of fragments over the full course of the shedding process. The comparison of $R_r(t)$ to the prediction thereof from Ref. [79], as presented in panel (c), shows that the sheet expansion in our cases has (i) a larger apex radius $R_{\max} \approx 0.14\,D_0 \mathrm{We}_d^{1/2}/2$ at (ii) an earlier apex moment $t_{\max} \approx 0.38\,\tau_c$, and also indicates (iii) a faster initial expansion speed $\dot{R}_0$ compared to the model (note that the model approximations in Ref. [79] were not aimed at describing the very early time response). These differences may be expected to propagate to the dynamics of the fragment speeds as discussed in Sec. 5.5.

5.5   Fragment speed and its evolution over time

5.5.1   Determination of fragment speed

The trajectories of the fragments are determined from the shadowgraphy images recorded by the double-frame PCO camera (see the microscopy system details in Fig. 5.1 of Sec. 5.2). Figure 5.3(c) illustrates an example of our post-processing procedure, where we overlap two consecutive images of the same sheet with a time delay of $\Delta t = 2\,\mu$s. We align both images by overlapping the pixels with the coordinates of the center of the sheet. Black and yellow colors in the image indicate the presence of tin or its absence at both frames, respectively. Green and red colors indicate the presence of tin at either 9 or 11 μs, i.e., at first and second frames, respectively. Using these

overlapped images we can keep track of the ballistic trajectory of individual fragments, which we draw using black lines that connect the location of single fragments at two moments in time. Individual fragments that detach from the ligaments acquire a speed that is constant over time. Therefore, the fragment speed u_f can be readily determined by dividing the distance traveled by a single fragment over the preset time interval Δt (cf. Fig. 5.1). To avoid including the fragments that are potentially out of focus and to obviate the need for correcting the finite imaging parallax caused by the 30° front-view angle, we restrict the analysis of the fragments and their positions to a region of interest at the top and bottom of the sheet that comprises $\theta = 90° \pm 10°$ and $270° \pm 10°$, see the white dashed lines in Fig. 5.3(c). Inset (c.1) illustrates an example of the detection of a single fragment within this angular range at two moments in time, with its corresponding radial positions plotted in panel (b). In our measurements, u_f is dominated by its radial component, with the contribution from the azimuthal component accounting for a few percent of u_f. We therefore refer to u_f as the radial speed of the fragments hereafter.

5.5.2 Fragment speed vs detachment time

To understand the dynamics responsible for the fragment speeds, we need to establish the origin of the fragments. The fragments are shed from their parent ligaments at a detachment time t_d. Given that the short time scales involved prevent the tracking of the full dynamics of individual ligaments, we determine t_d by individually finding the intersection between the ballistic trajectory of each fragment and the expansion trajectory of the relevant ligaments.

The radial trajectory of the ligaments, R_l, is determined from the distance of the outer contour to the center of the target as was illustrated in Fig. 5.3(a). Similarly to the analysis of the fragment trajectory, we only consider the outer contour for the region of interest identical to that of the relevant fragments, i.e., comprising $\theta = 90° \pm 10°$ and $270° \pm 10°$, as shown by the dashed white lines in Fig. 5.3(a). For each image, we take the ligament whose tip is furthest from the center of the target to be most relevant for the subsequent shedding, as these have a high chance to shed fragments. Averaging sufficient images (typically 20 images) taken at one time delay yields the mean value of the instantaneous radial positions of the ligament, which further enables a description of R_l over time. In Fig. 5.3(b) we plot the expansion trajectory of the ligaments obtained by following this procedure, for the same experimental conditions as those used to obtain the images in panels (a) and (c) ($D_0 = 67\ \mu$m and $E_p = 20$ mJ). Both the ligament R_l and rim trajectories R_r show an initial expansion, followed by a gradual decrease of their expansion rate. For each data set of a D_0-E_p combination, we

fit a fourth-order polynomial to the expansion trajectory of the rim R_r with its initial slope matching the corresponding $\dot{R}_0$. The results obtained allow us to determine the instantaneous speed of the rim $\dot{R}_r$ [cf. the example case shown in Fig. 5.3(b)]. For the ligament, we fit an unconstrained third-order polynomial to R_l in order to describe the continuous change of the position of the ligament tips. From the intersection of the curve for R_l with the fragment trajectory, we obtain the individual detachment time t_d. To gauge the uncertainty in obtaining t_d, we compared taking the instantaneous average ligament length to the instantaneous averaged length of only the outermost ligaments (most relevant for shedding), and found that this choice results in less than a 5% difference in the obtained t_d values.

Figures 5.5(a)-(e) present the fragment speed u_f as a function of the detachment time t_d for different droplet diameters and pulse energies as summarized in Tab. 5.1. The instantaneous speed of the rim $\dot{R}_r$ is also plotted in Figs. 5.5(a)-(e). We observe that the fragment and rim expansion speed $\dot{R}_r$ monotonically decrease over time. Furthermore, our data illustrate that higher laser energies lead to faster fragment speeds for a given droplet size. At any given detachment time, the speed of the fragments u_f is larger than the instantaneous speed of the rim $\dot{R}_r$ (compare symbols to solid & dashed lines in Fig. 5.5). This quantitative finding is consistent with the results reported in Refs. [21, 79], where the fragment speed is described by a local velocity correlated to the ligament dynamics added to the instantaneous expansion velocity of the rim $\dot{R}_r$. Our data further indicates that the initial expansion rate of the rim $\dot{R}_0$ sets the upper limit of the fragment speed during the sheet expansion. With $\dot{R}_0$ setting the starting point of u_f near $t_d = 0$, the moment at which $u_f = 0$ seems to be solely determined by the initial droplet size D_0 and not by the laser energy E_p. Figures 5.5(a)-(e) show how the time span (from the onset of the impact to the moment when $u_f = 0$) increases as we irradiate a larger droplet. These observations on both the characteristic speed and the time scale of the shedding process inspire us to seek a self-similar solution $y = g(x)$ to explain the fragment speeds with similarity variables $x = t/\tau_c$ and $y = u_f/\dot{R}_0$, in line with the findings of Wang *et al.* [21]. Figure 5.5(f) shows the same data presented in panels (a)-(e) but re-scaled using $\dot{R}_0$ and τ_c. The graph indeed reveals a collapse of all data sets onto a single master curve $u_f/\dot{R}_0 = g(t/\tau_c)$. Moreover, as discussed in Fig. 5.4(c), the scaled evolution of the rim $2R_r D_0^{-1} \mathrm{We}_d^{-1/2}$ can be described by a function that solely depends on $f(t/\tau_c)$, hence one expects a universal solution $\dot{R}_r/\dot{R}_0 = \phi(t/\tau_c)$ where $\phi(x) = \sqrt{3/2}f'(x)$ following the definition of the capillary time and the deformation Weber number. This curve, plotted in Fig. 5.5(f), is obtained by a concatenated fourth-order polynomial
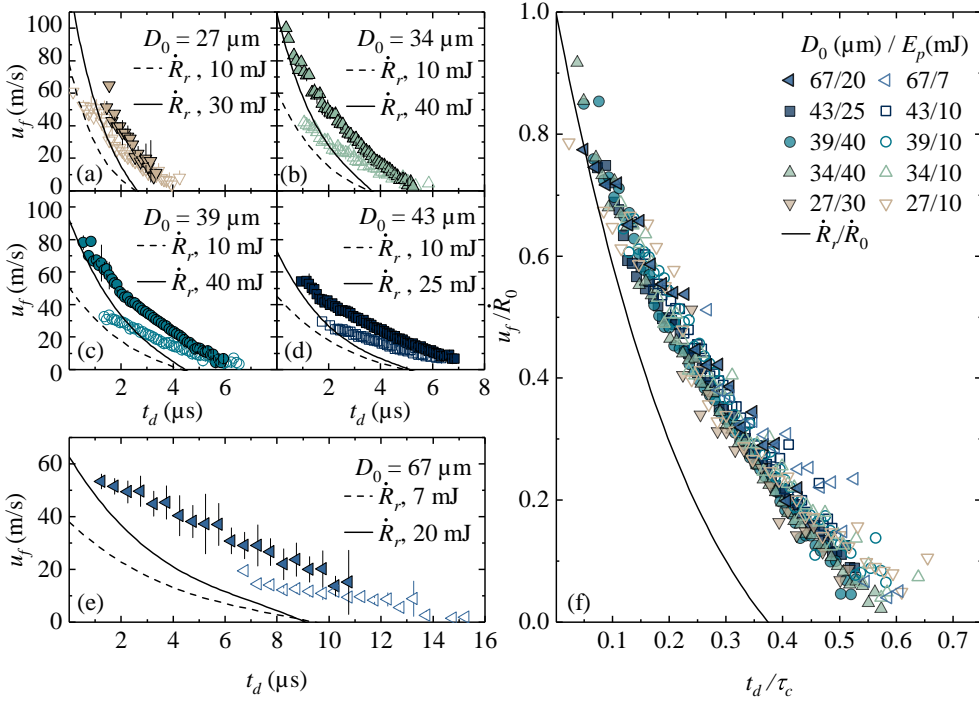
Figure 5.5: (a)-(e): Fragment speed u_f as a function of detachment time t_d for the various droplet diameters D_0. For each droplet size, results obtained using two different laser energies are presented, see Tab. 5.1. The rim expansion speed $\dot{R}_r$ is also plotted, with solid and dashed lines corresponding to the same experimental conditions for the filled and open symbols for u_f, respectively. (f) Same data as presented in (a)-(e) but now scaled by the initial expansion speed of the rim $u_f/\dot{R}_0$ as a function of the dimensionless time t_d/τ_c. The solid line presents the nondimensional speed $\dot{R}_r/\dot{R}_0$ obtained from a polynomial fitting to the data in Fig. 5.4(c). In (a)-(e) the error bars represent the standard deviation of binned data. These error bars have been omitted in (f) for better visibility.

fitting to all the available data of $R_r(t)$ shown in Fig. 5.4(c). For consistency, the fit is performed with the constraint $\phi(0) = 1$. Due to these two independent collapses of $\dot{R}_r/\dot{R}_0$ and $u_f/\dot{R}_0$, the difference between the rim and the fragment speed scales as $(u_f - \dot{R}_r)/\dot{R}_0 \sim g(t_d/\tau_c) - \phi(t_d/\tau_c)$, following a function that monotonically increases with time and is independent of the deformation Weber number.

A self-similar behavior of the fragment speeds has also been reported in Refs. [21, 79] on droplet impact on a pillar. In those works, the difference in velocities u_f and $\dot{R}_r$ is attributed to (a) the ligament growth and (b) the speed difference between the tip of ligaments and the fragments due to a one-necking-time shift (also see the Appendices).

By using the expansion curve of the rim R_r and by invoking mass conservation associated with the ligament and the rim, Wang *et al.* [79] further analytically identified (i) that $(u_f - \dot{R}_r)/\dot{R}_0$ scales as $\text{We}_d^{-3/8}$ and is (ii) almost invariant over time. These two theoretical findings are not supported by our observations, cf. Fig. 5.5. Moreover, the fragment speeds from Refs. [21, 79] may exceed $\dot{R}_0$ at $t = 0$, where the current study finds that $u_f \to \dot{R}_r$ when $t_d \to 0$. We note that the aforementioned description of u_f in Ref. [79] was based on their approximate solution for R_r; the use of their full solution instead may have led to results that are more in line with the current experimental work. The origin of the discrepancy of the current $(u_f - \dot{R}_r)/\dot{R}_0$ scaling with the pillar impact case [21, 79] is yet unclear. A dedicated experimental campaign would be required aimed also at the detailed study of the necking process itself. We hypothesize that part of the difference may originate from the very different original impact dynamics, where the laser-impact case has no "impactor" present even on the early, inertial time scale. This difference could cause different initial corrugations of the rim that further propagate to late-time dynamics such as the formation of ligaments and the shedding of fragments [17].

5.5.2.a *Energy fraction taken by the fragments*

Next, we aim to interpret the collapse of the fragment speed onto $u_f/\dot{R}_0 = g(t/\tau_c)$ by considering the energy partitioning. Once the droplet is set in motion by the laser pulse, the initial energy of the droplet E_{tot} can be described by its kinetic energy $\propto M_0(\dot{R}_0^2 + U^2) \sim M_0\dot{R}_0^2$ (as $U \sim \dot{R}_0$) and its surface energy $\propto \sigma R_0^2$, where M_0 is the mass of the original droplet. Given that $\text{We}_d \gg 1$ in our experiments, the kinetic energy of the initial droplet is much larger than its surface energy, thus leading to $E_{\text{tot}} \sim M_0\dot{R}_0^2$. The total energy E_{tot} is then distributed across the various channels, such as the sheet, rim, ligaments, and the energy accumulated in the fragments. Wang *et al.* [113] have shown, both experimentally and theoretically, that the fraction of the total energy residing in the sheet, rim, and in the fluid shed from the rim (i.e., the sum of ligaments and fragments) is a function of the dimensionless time t/τ_c only and is independent of the Weber number. Inspired by their work, we now further assume that the energy contained in each sub-system is Weber number independent, including those from ligaments and fragments (E_f) separately, i.e., $E_f/E_{\text{tot}} = h(t/\tau_c)$.

As we will explain below, the cumulative kinetic energy of the fragments can be determined by an integration of $\dot{m}_f u_f^2$ over time, where $\dot{m}_f$ is the instantaneous shedding rate of the fragments mass m_f and is also independent of the Weber number. As a result, as we will see, $u_f/\dot{R}_0$ solely depends on t/τ_c. The relative importance of the kinetic energy of a fragment with a speed u_f and a diameter d_f to its surface energy

is captured by the fragment Weber number $\text{We}_f = (1/2)(\rho \pi d_f^3/6)u_f^2/(\pi d_f^2 \sigma) = \rho u_f^2 d_f/12\sigma$. The value of We_f is then estimated by using the experimental data of u_f from Fig. 5.5. Following Wang *et al.* [23], d_f is obtained from $d_f \approx 1.7 b_r$ with the diameter of the bounding rim b_r in turn determined from the universal criterion of the local Bond number $\text{Bo} = \rho b_r^2(-\ddot{R}_r)/\sigma = 1$, where $\ddot{R}_r$ is the instantaneous deceleration of the rim determined from Fig. 5.4(c). The relation $\text{Bo} = 1$ established in Ref. [22] is based on momentum conservation of the corrugations on the rim, and the relation holds for high-Reynolds-number flows as applicable in our case where the Reynolds number $\text{Re} = D_0 \dot{R}_0/\nu \sim 10^4$ given the kinematic viscosity $\nu = 0.26 \times 10^{-6}$ m^{2}s^{-1} of liquid tin [114]. In the present work where the global Weber number $\text{We}_d = \rho \dot{R}_0^2 D_0/\sigma$ changes from approximately 1100 to 5500, We_f is significantly larger than 1 at times up to roughly $t/\tau_c \sim 0.4$. Therefore, for those fragments detached at $t_d \lesssim 0.4\tau_c$, the kinetic energy is the dominant contributor to the fragment's energy. The cumulative energy fraction of fragments E_f/E_{tot} at time t is thus given by

$$\frac{E_f(t)}{E_{\text{tot}}} \sim \int_0^t \left(\frac{\dot{m}_f}{M_0}\right)\left(\frac{u_f}{\dot{R}_0}\right)^2 d\tilde{t} \sim h(t/\tau_c). \tag{5.1}$$

Note that we neglect the (small) onset time of the shedding process and thus the integral in Eq. (5.1) starts from $t_d = 0$ [79]. It has been previously proposed and also experimentally supported in Ref. [23] that for the case of pillar impact the cumulative mass of fragments is independent of the Weber number and is a function of t/τ_c only. In other words, the term $\dot{m}_f/M_0$ in Eq. (5.1) is a function of t/τ_c alone. The instantaneous rate of liquid shed to fragments scales as $\dot{m}_f/M_0 \sim \rho \dot{N}_f d_f^3/M_0$, with $\dot{N}_f$ the instantaneous fragment shedding rate, and d_f the diameter of fragments shed. Given that $\dot{N}_f \sim \text{We}_d^{3/4}$ [23], $d_f \sim D_0 \text{We}_d^{-1/4}$ [22–24, 113] and $M_0 \sim \rho D_0^3$ we also obtain that $\dot{m}_f/M_0$ is independent of the Weber number. Therefore, from Eq. (5.1) we conclude that the term $u_f/\dot{R}_0$ is also a function of t/τ_c only and is independent of the Weber number, consistent with the collapse of all data observed in Fig. 5.5.

5.6 Conclusion

Laser pulse impact onto a tin microdroplet leads to an unsteady, fragmenting liquid sheet bounded by a rim. We experimentally determined the speed of fragments u_f that are formed upon breakup of the ligaments protruding from this bounding rim. We observed that fragments are produced by end-pinching for the most of the time interval relevant for the shedding process. In addition, we observed fragments shed via

Rayleigh-Plateau breakup of long ligaments at late times. A double-frame camera was used to capture the ballistic trajectories of the fragments, from which their speeds were determined. By finding the intersection of the ballistic trajectory of each fragment and the expansion trajectory of the ligaments R_l, we were able to determine the time of detachment t_d of each fragment. Our data show a monotonic decrease of u_f with t_d. The characteristic detachment time is set by the capillary time scale which depends on the initial droplet size. We observed that the fragment speed is larger than the instantaneous expansion rate of the sheet $\dot{R}_r$ at any given detachment moment t_d. The difference between the fragment and the rim speeds $u_f - \dot{R}_r$ monotonically increases over time, starting from $u_f - \dot{R}_r \to 0$ when $t_d \to 0$.

These observations enable us to identify a self-similar behavior, captured by $u_f/\dot{R}_0 = g(t_d/\tau_c)$, which collapses all available data. Such a self-similar behavior, combined with the similarity curve for the sheet expansion speed $\dot{R}_r/\dot{R}_0 = \phi(t_d/\tau_c)$, indicates that the difference in speed between u_f and $\dot{R}_r$ is given by $(u_f - \dot{R}_r)/\dot{R}_0 \sim g(t/\tau_c) - \phi(t/\tau_c)$. The self-similar curves are explicitly independent of the deformation Weber number We_d that was introduced and shown to capture the dynamics of the sheet expansion to a better accuracy than that one offered by the impact Weber number. We further demonstrated that the collapse of u_f is supported by energy conservation arguments, with the assumption that the fraction of the initial energy of the droplet channelled to the fragments is independent of the Weber number. The collapse of u_f enables a model prediction of the instantaneous speed and position of the fragments shed from tin sheets resulting from laser-pulse impact, as employed in state-of-the-art extreme ultraviolet nanolithography. Such a model, requiring as input just the initial droplet expansion speed, would enable the optimization of mitigation strategies against contaminating microparticulate debris to the benefit of the lifetime of industrial lithography tools. The finding that the speed of shed fragments has a robust upper limit of $u_f = \dot{R}_0$ is by itself particularly valuable in this regard. In addition, the correlation found between the rim expansion rate and the fragment speed — covering the full time span of the shedding process — may be applicable to impact scenarios ranging from agriculture, over pathogen transport, to nanolithography.

Appendix I: Summary of the experimental conditions

To assure the robustness of our experimental results, we systematically study the fragmentation process for five different droplet sizes. For each droplet size, we employ two different laser pulse energies. Experimental details are summarized in Tab. 5.1

| D_0 (μm)	τ_c (μs)	E_p (mJ)	U (m/s)	$\dot{R}_0$ (m/s)	We	We$_d$
27	6.5	10	41.5	77.8	583	2091
		30	84.6	126.8	2477	5556
34	9.2	10	33.4	61.3	487	1634
		40	73.1	109.3	2323	5198
39	11.3	10	28.9	50.5	418	1274
		40	62.5	92.2	1949	4240
43	13.0	10	25.4	45.1	355	1122
		25	43.6	72.9	1047	2925
67	25.2	7	19.7	37.9	330	1231
		20	36.6	62.7	1143	3354

Table 5.1: Parameters including the droplet diameter D_0, the related capillary time $\tau_c = [\rho D_0^3/(6\sigma)]^{1/2}$, laser pulse energy E_p, and the resulting parameters such as the center-of-mass speed U, initial expansion rate of the sheet $\dot{R}_0$, impact Weber number We $= \rho U^2 D_0/\sigma$, and deformation Weber number We$_d = \rho \dot{R}_0^2 D_0/\sigma$. Each data entry comprises 20–50 individual laser-droplet events per time delay.

Appendix II: Correlation between the fragment speed and the speed of ligaments tip

It was found in Ref. [21] that the fragment speed in the lab frame follows the velocity of ligaments tip u_l but one necking-time t_{neck} prior to the detachment. In other words, the fragment speed as a function of the detachment time $u_f(t_d)$ relates to the ligament velocity following

$$u_f(t_d) = u_l(t_d - t_{\text{neck}}). \tag{5.2}$$

The necking time $t_{\text{neck}} \sim (\rho w_l^3/\sigma)^{1/2}$ is proportional to the local capillary time with the prefactor varying between 2 to 5 (see, e.g., Refs. [21, 110, 115–117]). This relation yields a t_{neck} ranging from several hundreds of nanoseconds to microseconds in the context of our study where micrometer-thick ligaments are formed.
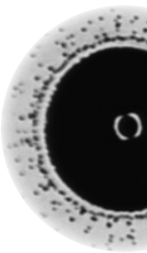
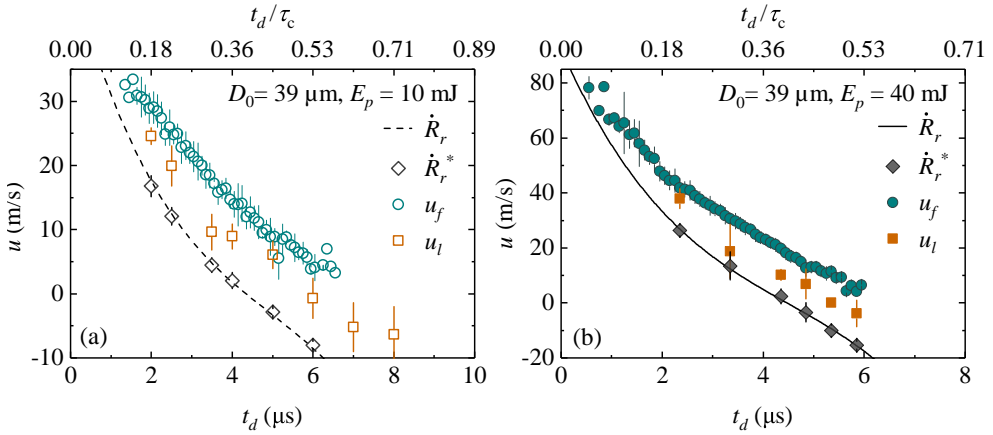Figure 5.6: Speed of fragments u_f and instantaneous velocity of the tip of ligaments u_l as a function of detachment time t_d, along with the expansion rate of the rim $\dot{R}_r$, $\dot{R}_r^*$. Two cases with the same droplet diameter $D_0 = 39\,\mu m$ for two laser pulse energies (a) $E_p = 10\,mJ$ and (b) $E_p = 40\,mJ$ are presented in the figure.

With the double-frame camera employed in this study, we were able to estimate through visual inspection the speed of a single ligament in the lab frame u_l by dividing the travelling distance of the ligament tip by the time delay Δt between the two frames. This method thus provides an average speed of ligaments within Δt. Ligament speeds u_l obtained following this procedure are presented in Fig. 5.6 for selected ligaments from the data sets with $D_0 = 39\,\mu m$ at two different energies $E_p = 10\,mJ$ and $40\,mJ$ that correspond to panel (a) and (b), respectively. Each data point of u_l represents the mean value for typically 10-20 manually inspected ligaments in a region of interest identical to that of the fragment speed, i.e., the region comprising $\theta = 90° \pm 10°$ and $270° \pm 10°$. The corresponding fragment speed [i.e., the same data presented in Fig. 5.5(c)] is also plotted in the graph. Figure 5.6 shows that the ligament velocity u_l indeed follows the fragment speed, with a temporal shift, ranging from several hundreds of nanoseconds to microseconds, toward earlier moments. Additionally, the distance travelled by the basis of each single ligament, i.e., the local travelling distance of the rim (following the discussion in Sec. 5.4) can be obtained. These data, labelled as R_r^* to be distinguished from the data set $\dot{R}_r$, are also presented in Fig. 5.6. As expected, we observe a close agreement between $\dot{R}_r$ and $\dot{R}_r^*$, supporting the validity of our procedures to measure both u_l and $\dot{R}_r^*$.

Appendix III: Polynomial descriptions of the collapse curves[3]

The collapse of the expansion trajectory $R_r(t)$ (Fig. 5.4) and fragment speed $u_f(t_d)$ (Fig. 5.5) onto self-similar curves provides a powerful predictive tool to evaluate the creation of a tin target. For application purposes, we present here the results of polynomial fitting to these data of R_r and u_f.

For the expansion of the rim $R_r(t)$, we fit a third-order polynomial to the concatenated data of $2R_r D_0^{-1} We_d^{-1/2}$ in Fig. 5.4(c). The fitting gives

$$\frac{2R_r}{D_0 \sqrt{We_d}} = A(t/\tau_c)^3 + B(t/\tau_c)^2 + C(t/\tau_c) + D, \tag{5.3}$$

where $A = 0.33(5)$, $B = -0.92(5)$, $C = 0.57(2)$ and $D = 0.035(2)$, with the number in brackets representing the one-standard-deviation uncertainty.
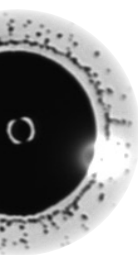
In the case of fragment speeds, we fit a third-order polynomial to the data of $u_f / \dot{R}_0$ as a function of t_d / τ_c in Fig. 5.5(f), with the constraint of constant term set to unity. The fitting gives

$$\frac{u_f}{\dot{R}_0} = P_3(t/\tau_c)^3 + P_2(t/\tau_c)^2 + P_1(t/\tau_c) + 1, \tag{5.4}$$

where $P_3 = -2.1(3)$, $P_2 = 3.9(2)$, and $P_1 = -3.15(4)$. This fitted result was used as input to estimate the fragment Weber number in Sec. 5.5.2.a.

---
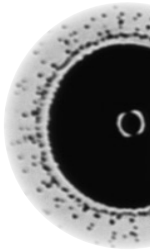
[3]Appendix III is added to this Chapter.

CHAPTER 6

DISCUSSION: MASS DISTRIBUTION OF TIN TARGETS FOR EUV SOURCES

Bo Liu, Randy A. Meijer, Wei Li, Hanneke Gelderblom, Javier Hernandez-Rueda, and Oscar O. Versolato
In preparation

6.1   Introduction

How is liquid tin spatially and temporally distributed in a prepulse-deformed target? This question, as put forward in Chapter 1, motivates the work in this thesis and naturally arises when discussing the coupling of a liquid tin target with the main pulse. Inspired by Wang *et al.* with their observations on ubiquitous cases of droplet impact on a pillar [20, 22], we proposed that after laser impact, the initial volume of a droplet $V_0 = \pi D_0^3/6$ with a diameter of D_0 is distributed over a *sheet*, a bounding *rim*, *ligaments* that radially protrude from this rim, and *fragments* generated by breakup of ligaments. One unique feature of the sheet formed by laser impact is a disk-shaped feature — a *center mass* located in the center of the sheet (cf. Fig. 1.2, Chapter 1). Apart from these channels, a certain fraction of tin will be heated up by the laser pulse and converted to a plasma or vapor phase. To this end, we propose that the volume distribution of the tin from the initial droplet is given by

$$V_0 = V_s + V_r + V_l + V_f + V_c + V_a, \tag{6.1}$$

where the volume in the sheet, rim, ligaments, fragments, center mass, and that ablated by the laser pulse are represented by V_s, V_r, V_l, V_f, V_c, and V_a, respectively.

In Chapter 2, we experimentally provided the volume of the sheet V_s using the measurements on the sheet thickness. Furthermore, data for V_s at earlier moments in the droplet expansion were provided in Chapter 3 using a novel experimental method. In addition, in Chapter 3 we confirmed the presence of the bounding rim and the center mass. Next, as part of our work to investigate the energy partitioning between deformation and propulsion of the laser-impacted droplet, we performed numerical simulations using RALEF-2D in Chapter 4. From the data underlying the presented results, we were able to access the volume fraction ablated by the laser pulse V_a. We further experimentally investigated the fragment speed in Chapter 5. We found a self-similar behavior of this speed which allowed us to describe the spatial distribution of the liquid carried by fragments. Besides the fragment speed, Chapter 5 employed a post-processing on front-view shadowgraphy images that enabled us to accurately identify the location of the rim and its expansion trajectory $R_r(t)$. We found a self-similar curve onto which all the results of $R_r(t)$ can be collapsed. Combining this self-similarity of R_r, and the robust analytical model for the thickness of the rim found by Wang *et al.* [22], the volume of the rim V_r can be determined. In summary, our results revealed a continuous loss of tin from the sheet to the bounding rim and the extruding ligaments. Eventually, the fluid collected in the ligaments disintegrates in the form of fragments, which radially fly away from the sheet with a constant

speed. Although the main channels for tin partitioning have been identified in previous Chapters, a precise quantification of the volume fraction in the channels of fragments V_f, ligaments V_l, and the center mass V_c has not yet been undertaken. To determine these quantities, we need a better optical resolution to access fragment size, ligament length, and other relevant parameters.

In this Chapter, we provide a global volume distribution among the channels listed in Eq. (6.1) by combining our new experimental results on the droplet-laser impact with analytical models previously developed for the analogous case of a droplet falling on a pillar. Our imaging system has been upgraded to provide enhanced resolution not only for the front-view (as previously introduced in Chapter 5), but also for the side-view camera. In Sec. 6.2, we describe how these images are used to determine the diameter of fragments d_f by applying machine learning. Furthermore, by employing a double-frame camera, we obtain the detachment time t_d for each individual fragment as described in Chapter 5. Relating the detachment time of each fragment to its diameter provides the instantaneous size of the shed fragments $d_f(t_d)$. These results, in combination with the shedding rate (the rate of increase of the fragment number), eventually yield the volume of liquid accumulated in the fragments V_f over time.

Next, our post-processing of the front-view images allows us to accurately detect the formation of ligaments at the edge of the sheet. By finding the position of the bounding rim, the length of each ligament L_l growing from the rim is determined. To get the instantaneous thickness of the ligaments w_l, we invoke analytical models from Refs. [22, 23]. As the geometry of a single ligament can be well described by the shape of a cylinder, the data of w_l, L_l, and the ligament number N_l allow determining the volume of ligaments V_l.

In Sec. 6.3, we determine the volume of the center mass V_c by the associated remnant of liquid situated in the center of the sheet, as assessed from the side-view images. By reviewing the numerical simulations performed in Chapter 4, originally designed to study the early-time droplet deformation, we are able to estimate the volume of ablated material V_a and present the results in Sec. 6.4. Next, in Sec. 6.5, we briefly recap the experimental study on the volume of the sheet V_s previously presented in Chapters 2 and 3. In Sec. 6.6, we discuss the volume of the rim V_r obtained by using our data of R_r [cf. Eq. (5.3), Chapter 5] and an analytical model from Ref. [22]. Finally, in Sec. 6.7, we summarize these results of volume fractions taken up by the different channels and provide the full volume distribution of tin in a target.
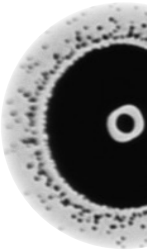
6.2   Volume of the fragments and ligaments

To obtain the volume of fragments and ligaments, we first need to assess their diameters, which are at or below the resolution of our imaging systems ($\approx 3\ \mu$m). In the case of fragments, we employ machine learning to determine their diameters under these challenging conditions. The data obtained are used to validate pre-existing models for the fragment diameter originally devised from Refs. [22, 23] for the case of droplet-pillar impact. In addition to the diameter of the fragments and ligaments, other parameters such as fragment number, ligament number, and ligament length are required to fully determine the volume of fragments and ligaments. In this Section, we first discuss the temporal evolution of the volume accumulated in fragments V_f. Next, we will discuss the length and number of ligaments. Relating these quantities allows us to present the instantaneous volume contained in ligaments V_l.

   The volume accumulated in the fragments over time can be expressed as

$$V_f(t) = \int_{t_{\text{onset}}}^{t} \frac{\pi}{6} d_f^3 \dot{N}_f \, d\tilde{t}, \tag{6.2}$$

where t_{onset} is the onset time of fragmentation, $\dot{N}_f$ the shedding rate related to the fragment number N_f, and d_f the diameter of the newly formed fragments. Equation (6.2) can be approximated by its discretized form

$$V_f(t_i) \approx \sum_{t_{\text{onset}}}^{t_i} \frac{\pi}{6} d_f^3 \bigg|_{t_d = \frac{t_{i-1} + t_i}{2}} (\Delta N_f), \text{ with}$$
$$\Delta N_f = N_f \bigg|_{t_i} - N_f \bigg|_{t_{i-1}}. \tag{6.3}$$

where the subscript i represents the counter for the sampling point in time, and $d_f(t_d)$ is the diameter of the fragments shed at t_d. Equation (6.3) requires as input the fragment number N_f at each time delay, and the instantaneous diameter of the fragments d_f detached at that time. The experimental results on these two parameters will now be discussed.
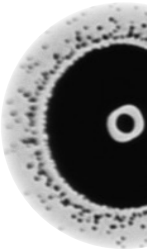
6.2.1   Fragment number

Figure 6.1(a) presents the fragment number N_f as a function t/τ_c for different combinations of droplet diameter D_0 and pulse energy E_p; $\tau_c = [\rho D_0^3 / (6\sigma)]^{1/2}$ is the capillary time with the density $\rho = 6970\ \text{kg m}^{-3}$ and the surface tension of liquid tin $\sigma = 0.544$

N/m. Each data point represents the mean value of the fragment number obtained from several images (typically 20 images) recorded at the same time delay. For each image, the fragment number is obtained by our fragment-detection algorithm with an auxiliary correction from manual inspections. The performance of this post-processing is illustrated in the inset of Fig. 6.1(a). It is shown that our algorithm could fail to correctly identify a fragment when it is (i) too close to its neighbor fragment, (ii) still in a ligament breakup process, and (iii) too far out of focus. These errors are corrected by our manual check. Our data in Fig. 6.1(a) shows that for a fixed D_0, a higher pulse energy results in a larger fragmentation rate $\dot{N}_f$, and also an earlier onset of fragmentation t_{onset}, leading to a larger N_f at a given t/τ_c.

Figure 6.1(b) presents $t_{\mathrm{onset}}/\tau_c$ as a function of the deformation Weber number (referred to as the Weber number hereafter) $\mathrm{We}_d = \rho \dot{R}_0^2 D_0/\sigma$ where $\dot{R}_0$ is the initial expansion speed of the droplet; $\dot{R}_0$ is determined by a linear fit of R_r data (following Klein *et al.* [28]) using the first three time frames after the onset of the impact, typically up to 300 ns $\sim 1\,\mu$s. Our data indicate an earlier onset of fragmentation with an increasing Weber number. This observation has also been reported for the case of droplet impact on a pillar in Ref. [79], in which a scaling law $t_{\mathrm{onset}}/\tau_c \sim \mathrm{We}_d^{-1}$ was found. A fit of this power law to our data is plotted in Fig. 6.1(b) by a solid line. The prefactor from the fit is 263(23), with the number in the bracket representing the standard error of the fit. This number is in reasonable agreement with the prefactor ≈ 320 analytically obtained in Ref. [79].

We observe that for most of the time during the shedding process, the increase in fragment number follows a linear trend, hence there is a constant shedding rate $\dot{N}_f$ that depends only on the Weber number. Figure 6.1(c) presents $\dot{N}_f \tau_c$ as a function of We_d, where $\dot{N}_f$ is obtained by a linear fit to the time domain of N_f where a constant shedding rate is evident. Our graph shows an increase in $\dot{N}_f$ with increasing We_d. In Ref. [23], the fragments are generated with a continuously decreasing rate $\dot{N}_f$, in contrast with our results in Fig. 6.1(b). It is yet unclear what is the origin of this difference between our results and those of Ref. [23]. We do note that we also found a disagreement with the same work on the topic of fragment speed in Chapter 5. Therefore, we speculate that both discrepancies have the same root cause and that a detailed study of the ligament growth and fragment pinch-off dynamics is called for. In Ref. [23] a scaling law of $\dot{N}_f \tau_c \sim \mathrm{We}_d^{3/4}$ is analytically identified. This scaling is also plotted in Fig. 6.1(c) and is shown to be in good agreement with our data, where a prefactor of 1.1(1) is used as obtained from a fit to our data.
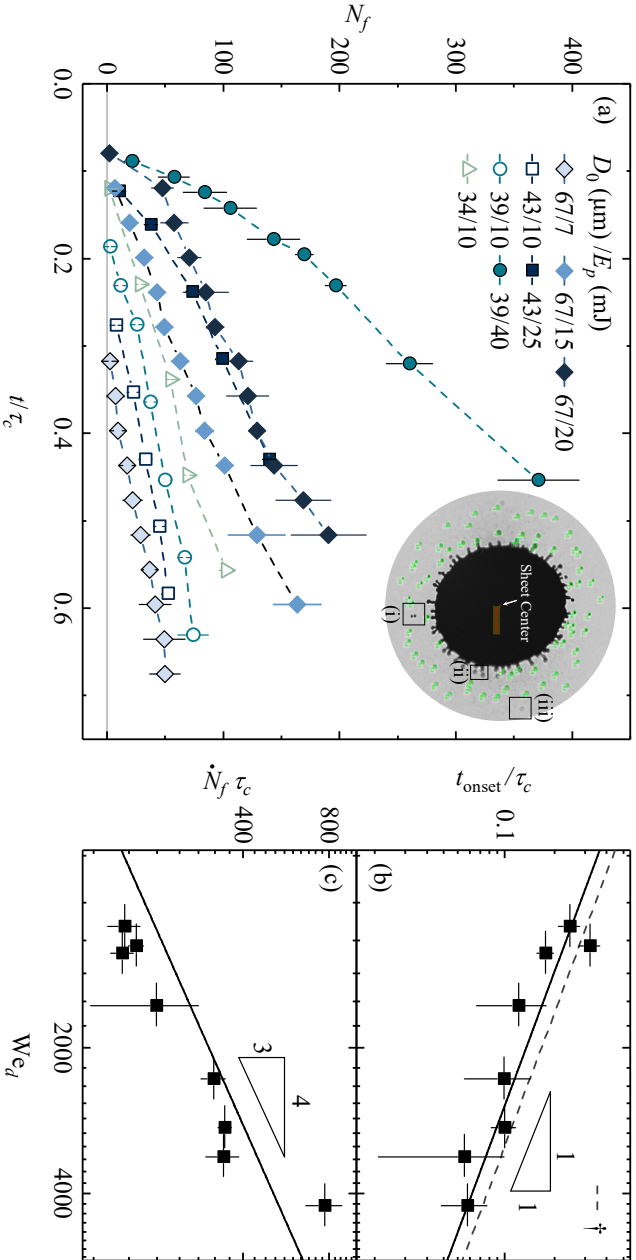
Figure 6.1: (a) Fragment number N_f as a function of nondimensional time t/τ_c for different combination of droplet diameters D_0 and laser pulse energies E_p. The inset shows a front-view shadowgraphy image of an expanding sheet (horizontally stretched to correct for the 30° observation angle) that illustrates the performance of our post-processing for obtaining the fragment number. Three scenarios where our processing will likely fail to detect fragments are indicated by three boxes (i–iii); see the main text. (b) Scaled onset time of fragmentation t_{onset}/τ_c as a function of the Weber number We_d. The solid line is a power-law fit of $t_{onset}/\tau_c \sim We_d^{-1}$ to the data, which yields a prefactor of 263(23) with the number in the bracket indicating the standard deviation. The dashed line represents $t_{onset}/\tau_c = 320\,We_d^{-1}$ from Ref. [79] (†). (c) Scaled shedding rate $\dot{N}_f\tau_c$ as a function of We_d. The solid line represents the power-law fit of $\dot{N}_f\tau_c \sim We_d^{3/4}$ to the data as proposed in Ref. [23]. The fit yields a prefactor of 1.1(1).

6.2.2 Fragment diameter

As mentioned above, the typical fragment diameters studied in this Chapter are at or below the resolution of our imaging system. To still obtain these diameters, we apply machine learning based on a convolutional neural network. The training data for the machine learning are obtained from a custom calibration target. This calibration target consists of a series of 200-nanometer-thick gold disks with stepped diameters ranging from 1.4 to 40 μm. These disks are developed on a fused-silica film substrate with a thickness of 500 ± 20 μm. The calibration target is imaged using the exact same imaging setup and configuration as was used to record the images of the tin target fragments of interest. By recording an image of the calibration target at several focal positions, the training data set is assembled. By including out-of-focus images, the trained network is able to correctly identify the size of fragments, even when they are positioned slightly out of focus. As is conventional, part of the training data set (~20%) is excluded from the training procedure and is used for validation. We find that over the full range of sizes (i.e., from 1.4 to 40 μm), the network is capable of determining the real size with an error less than 10%. To characterize the ability of the network to interpolate the size between the steps of the calibration target, we randomly exclude disks from the training set. In these cases, the network still enables the correct size to be determined during validation with similar precision.

Figure 6.2(b) presents images of the gold disks on the calibration target captured by our imaging system. In Fig. 6.2(c), we present the fragments detected in our experiments with their size determined by machine learning. The images in panel (c) are, visually, indistinguishable from those in panel (b), indicating that the machine learning method can accurately determine the size of the fragments within the range of the calibration target. To obtain the final fragment-size data, we constrain the eccentricity of the identified fragments. This filter enables us to separate the individual fragments — located within a finite distance from the focal plane (approximately ±30 μm) — from aggregated fragments or any ligaments that were mistakenly identified as fragments.

Figure 6.2(a) presents the fragment diameter d_f, as determined with our machine learning analysis, as a function of the radial distance to the center of the sheet r. The data are obtained for the case where $D_0 = 67$ μm and $E_p = 20$ mJ. The radial distribution of d_f at two different time delays ($t = 5$ μs and $t = 10$ μs) are plotted. Our results show that more outward-located fragments have (i) smaller sizes and (ii) travel faster (as indicated by a longer traveling distance in the r direction). These observations are consistent with the conclusions presented in Chapter 5 on (ii) fragment speeds and, as we will discuss below, with previous work on droplet-pillar impact [21–23].

Since detached fragments travel at constant speeds, the radial distribution of
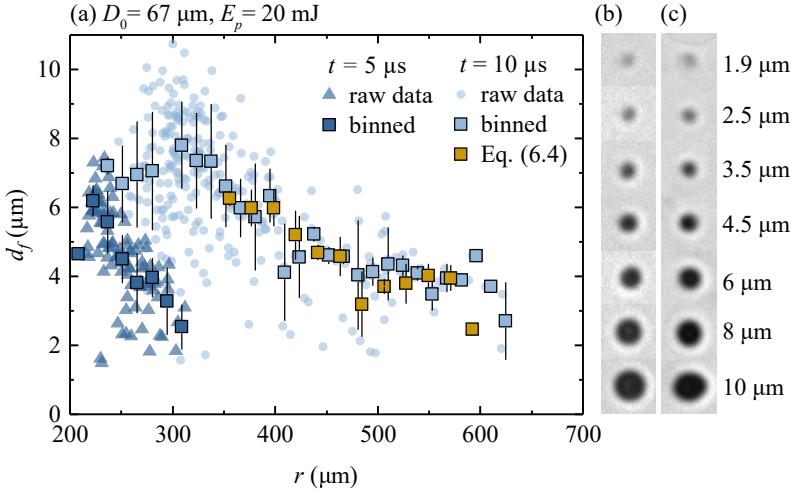
Figure 6.2: Fragment diameter d_f determined by machine learning combined with training data obtained from a custom calibration target. (a) Fragment diameter d_f as a function of radial distance to the center of the sheet r. Results and their corresponding binned data for both $t = 5$ and $10\,\mu$s are plotted, where $t = 0$ marks the onset of the laser pulse. Results for $\tilde{d}_f(r)$ at $t = 10\,\mu$s, based on Eq. (6.4), are also shown. (b),(c) Example images of the calibration target (used for the training of the network) and detected fragments, respectively.

fragment diameters at $t = 10\,\mu$s can be obtained by propagating the distribution $d_f(r)$ at an earlier moment $t = 5\,\mu$s following

$$\tilde{d}_f(r)\ \Big|_{t = 10\,\mu\text{s}} = d_f\left(r - u_f(r)\,\Delta t\right)\ \Big|_{t = 5\,\mu\text{s}}. \tag{6.4}$$

This radial distribution $\tilde{d}_f(r)\ |_{t = 10\,\mu\text{s}}$ is also plotted in Fig. 6.2(a) in which the fragment speed u_f at $t = 5\,\mu$s is obtained by our double-frame camera. Details on determining the fragment speeds can be found in Chapter 5. It is shown that $\tilde{d}_f(r)\ |_{t = 10\,\mu\text{s}}$ agrees well with the data from direct measurements at $t = 10\,\mu$s. This agreement shows our ability to connect each individual fragment with its diameter d_f and speed u_f that define the trajectory of the fragments. Next, by finding the intersection of the ballistic trajectories of fragments with the radial expansion of the ligament, we acquire the detachment time t_d of each corresponding fragment (cf. Chapter 5). The results of d_f and their dependence on t_d will now be discussed.

Figure 6.3 presents d_f as a function of t_d/τ_c. Our observations are consistent with the studies by Wang *et al.* [21–23] on a water droplet falling on a pillar. In these studies,

the relation between the diameter of the bounding rim, ligaments, and fragments has been studied in detail. First, by invoking momentum conservation on an extrusion of a ligament growing from a continuously decelerating rim, Wang *et al.* [22] found a universal criterion that governs the instantaneous thickness of the bounding rim b_r

$$\text{Bo} = \rho b_r^2 (-\ddot{R}_r)/\sigma = 1, \tag{6.5}$$

where Bo is the local Bond number of the rim based on its radial deceleration $\ddot{R}_r$. During the expansion of the sheet, the deceleration scales as $-\ddot{R}_r \sim R_{\max}/\tau_c^2 \sim (\sigma/\rho R_0^2)\text{We}_d^{1/2}$ with $R_{\max} \sim R_0 \text{We}_d^{1/2}$. Substituting this relation into Eq. (6.5) yields $b_r \sim R_0 \text{We}_d^{-1/4}$, consistent with the previous study by Villermaux *et al.* [24]. Next, the relation between the diameters of ligaments w_l and fragments d_f was experimentally investigated in Ref. [21, 23] to yield

$$\begin{aligned} d_f(t) &\approx 1.5 w_l(t), \quad \text{with} \\ w_l(t) &= \alpha(t) b_r, \end{aligned} \tag{6.6}$$

where $\alpha(t) = 0.32(t/\tau_c)^2 + 0.24(t/\tau_c) + 0.92$ is a function of t/τ_c solely and varies from $1 \sim 1.2$ during the expansion of the sheet [23]. Values of $d_f(t_d)$ predicted by Eqs. (6.5) and (6.6) are depicted in Fig. 6.3 by a solid line. The deceleration of the sheet $\ddot{R}_r$ as input for the relation $\text{Bo} = 1$ is obtained by fitting a third-order polynomial to the expansion trajectory of the rim R_r for the corresponding data set. Figure 6.3 presents good agreement between the analytical prediction and our results. This agreement may be seen to either verify our determination of fragment diameter or, alternatively, to demonstrate the robustness of Eq. (6.6). Given the agreement shown in Fig. 6.3, we decide to employ Eq. (6.6) for the discussion below on the global volume fractions.

6.2.3   Ligament length

Next, we seek the results of the instantaneous volume contained in the ligaments V_l. A single ligament can be described as a cylinder with a length L_l and a diameter w_l, hence a volume $\pi w_l^2 L_l/4$. We will first discuss the experimental results for ligament length. The length of each ligament is determined by the distance from the tip of the ligament to the rim. The detection of the rim and the tip of the ligament follows the method detailed in Chapter 5, also see Fig. 6.4(c). For the values of ligament diameter w_l, they are extracted from Eq. (6.6).

Figure 6.4(a) presents the probability density function (PDF) of ligament length scaled by the initial droplet diameter L_l/D_0 ($D_0 = 67 \ \mu\text{m}$) at four different time delays
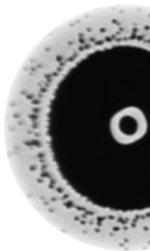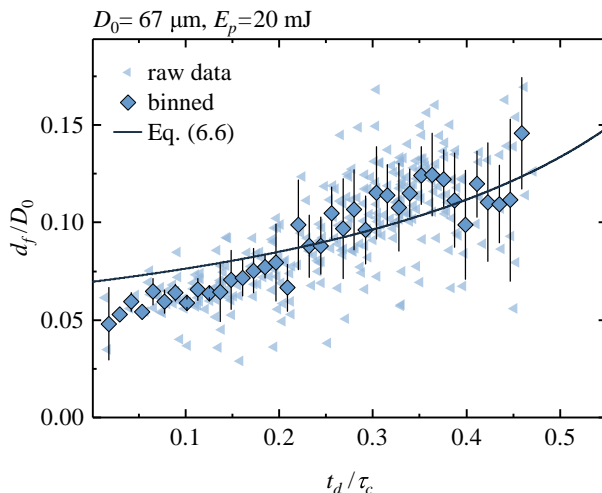
Figure 6.3: Scaled fragment diameter d_f/D_0 instantaneously shed at moments of t_d/τ_c. The solid line presents the prediction from Eq. (6.6).

after laser pulse impact. Our results show that with increasing time, the ligament length shifts toward a greater value with a longer most-probable-length $L_{l,\text{PDF}}$. The spreading of L_l increases as old ligaments grow while new ones are being generated. The increase in $L_{l,\text{PDF}}$ over time is shown in Fig. 6.4(b) in which $L_{l,\text{PDF}}$ for three different pulse energies are presented. Figure 6.4(b) also shows that the growth of $L_{l,\text{PDF}}$ is rather independent of the pulse energy. It should be noted that an accurate estimate of L_l by our post-processing requires that the ligaments protrude radially from the rim. Any deviation from an outward-oriented cylindrical shape will lead to an underestimate of the actual length of the ligament.

6.2.4   Ligament number

In addition to ligament length, the post-processing illustrated in Fig. 6.4 (c) yields ligament number N_l for each processed image. Figure 6.5(a) presents N_l as a function of t/τ_c for different combinations of droplet diameter D_0 and pulse energy E_p. It is shown that for a given droplet size, a larger number of ligaments is induced by a higher pulse energy. Furthermore, once the first ligaments are detected by our post-processing, we observe a slight increase in their number with time, reaching a maximum at $t \approx 0.3$–$0.5\,\tau_c$. Later, N_l decreases, mainly due to the merging of ligaments (cf. Fig. 5.2 in
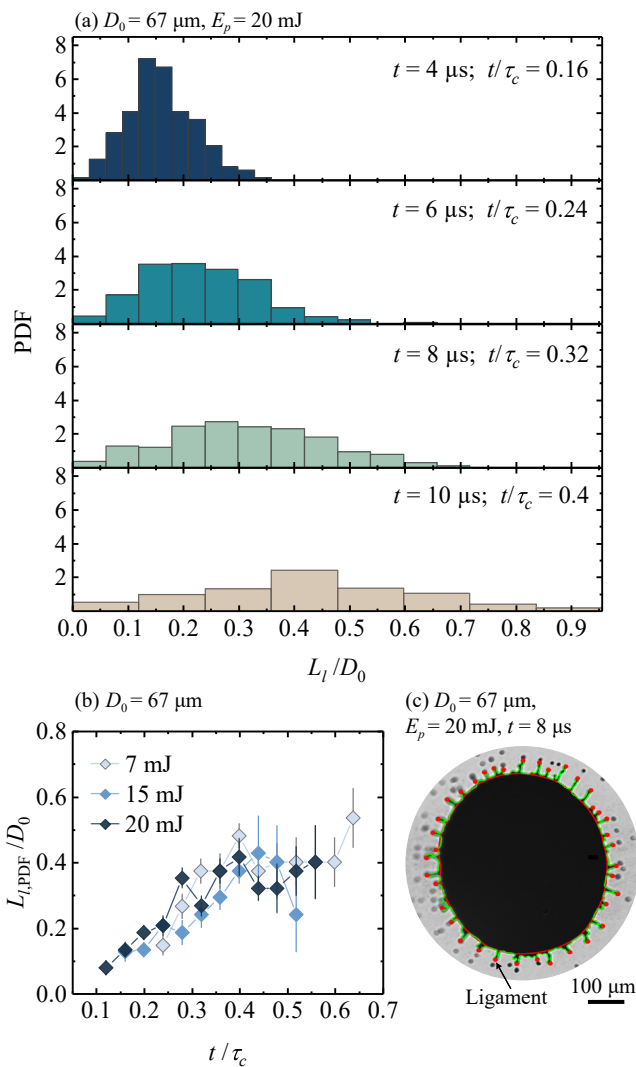
Figure 6.4: (a) Probability density function (PDF) of scaled ligament length L_l/D_0 for four different time delays (see the legend), obtained with $D_0 = 67\,\mu$m and $E_p = 20$ mJ. (b) The most probable length of ligament $L_{l,\mathrm{PDF}}$ as a function of nondimensional time t/τ_c for three different pulse energies (see the legend). The error bar shown equals the bin width in panel (a). (c) A front-view shadowgraphy image of a sheet (horizontally stretched to correct for the $30°$ observation angle) to illustrate the outer contour (green) and the inner contour (red). The image is capture at $t = 8\,\mu$s with $D_0 = 67\,\mu$m and $E_p = 20$ mJ. Each ligament tip which is detected from the outer contour is indicated by red dots.
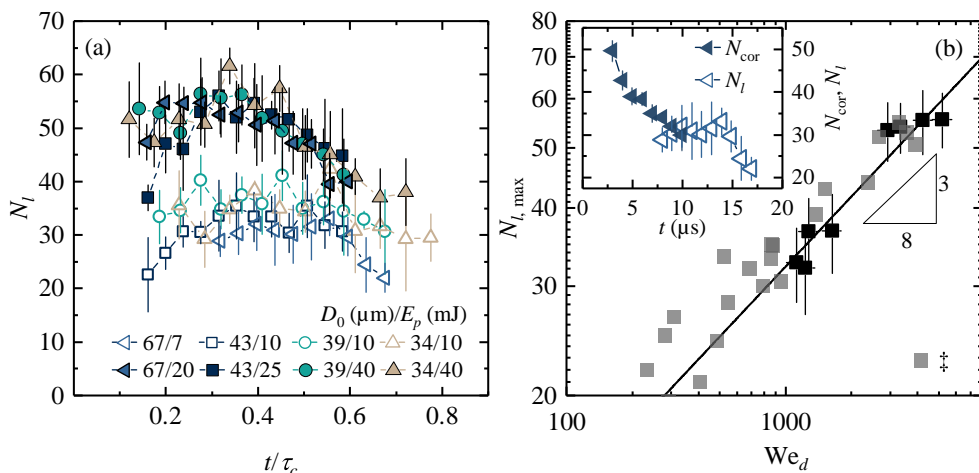
Figure 6.5: (a) Ligament number N_l as a function of t/τ_c for different combination of droplet diameters D_0 and the pulse energies E_p (see the legend). (b) $N_{l,\mathrm{max}}$ obtained as the average ligament number surrounding its apex value as a function of the Weber number We_d. Data from Ref. [17] (‡) are reproduced in the graph. The solid line represents a power-law fit of $N_{l,\mathrm{max}} \sim \mathrm{We}_d^{3/8}$ to the results of our study, which yields a prefactor of 2.4(1) with the number in the bracket representing the standard deviation from the fit. The inset shows corrugation number N_{cor} and the ligament number N_l as a function of t for the data set of $D_0 = 67\,\mu m$ and $E_p = 7\,\mathrm{mJ}$.

Chapter 5). This coalescence of ligaments has also been reported by Klein *et al.* [17] in the context of laser impact, and by Wang *et al.* [21] for pillar-impacted droplets.

Figure 6.5(b) presents $N_{l,\mathrm{max}}$ as a function of We_d. The value of $N_{l,\mathrm{max}}$ for each data set is obtained by averaging the ligament number ranging from two frames in time preceding the maximum of N_l to two frames after that moment. A power-law fit of $N_l \sim \mathrm{We}_d^{3/8}$ is performed to the data and yields a prefactor of 2.4(1). This power law has been analytically proposed in Ref. [17] where it has been further confirmed experimentally for the case of laser impact on a droplet with $D_0 = 50\,\mu m$. These data are reproduced in Fig. 6.5(b), showing their agreement with the results of our measurements.

The scaling $N_l \sim \mathrm{We}_d^{3/8}$ has also been reported by Wang *et al.* [23] for the case of pillar-impact. We note, following Ref [23], that measurements of the number of ligaments should be distinguished from those of initial corrugations — the early-time manifestation of capillary instabilities arising on the rim. Only a fraction of the corrugations develop into ligaments. This phenomenon is also observed in our case (cf. Fig. 5.2, Chapter 5) where both the temporal and spatial dimension are drastically smaller than those in Ref. [23]. The inset in Fig. 6.5(b) shows the number
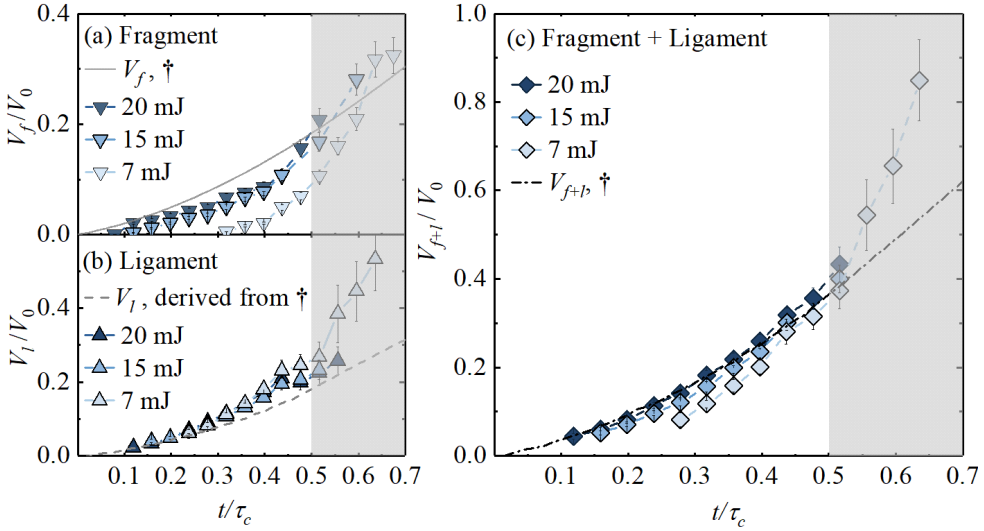
Figure 6.6: (a),(b) Volume ratio of the fragments V_f and ligaments V_l with respect to that of the initial droplet V_0 as a function of t/τ_c. (c) The sum of fragment and ligament volume $V_{f+l} = V_f + V_l$ with its ratio to V_0 as a function of t/τ_c. The solid & dash-dot lines presented in (a) and (c), respectively, plot the predictions on V_f/V_0 and V_{f+l}/V_0 from Ref. [113] (†). From that study, the volume of ligaments is derived as $V_l = V_{f+l} - V_f$ and is plotted as a dashed line in (b). The shaded area indicate the temporal range of $t > 0.5\tau_c$.

of corrugations N_{cor} and ligaments N_l for the same experimental conditions as that shown in Fig. 5.2, Chapter 5 ($D_0 = 67\ \mu m$, $E_p = 7$ mJ). We note that N_{cor} is determined through direct visual inspection. It is clearly shown that the corrugation number decreases, with only part of them becoming ligaments at later moments.

6.2.5 Results of fragment & ligament volume

Figure 6.6(a) shows the volume ratio V_f/V_0 as a function of t/τ_c. Each V_f data point is determined following Eq. (6.3) with N_f retrieved from the experimental data shown in Fig. 6.1, and $d_f(t_d)$ obtained from Eq. (6.6). The application of Eq. (6.6) is supported by the agreement between the model and our machine learning results on $d_f(t_d)$ presented Fig. 6.3. Given the temporal range of the comparison in Fig. 6.3 (i.e., $t \lesssim 0.45\tau_c$) and also the validity range $t \lesssim 0.5\tau_c$ for Bo $= 1$ (cf. Fig. 2.4, Chapter 2) for which the rim requires a sufficiently large deceleration [22], we apply Eq. (6.6) to the determination of d_f and V_f up to $t = 0.5\tau_c$. Figure 6.6(a) indicates a continuous increase in V_f over time, suggesting a progressive detachment of liquid into fragments. Furthermore, the results for the $E_p = 15$ and 20 mJ cases are almost indistinguishable.

For the case of $E_p = 7$ mJ, less liquid is channeled into the fragments at early times. This peculiarity is mainly due to the strongly delayed fragmentation onset moment for the small energy case: $t_{\mathrm{onset}}/\tau_c \approx 0.3$ for $E_p = 7$ mJ, as compared to $t_{\mathrm{onset}}/\tau_c \approx 0.1$ and 0.06 for $E_p = 15$ and 20 mJ, respectively [cf. Fig. 6.1(b)]. Figure 6.6(b) presents the volume ratio of the ligaments to the initial droplet V_l/V_0 as a function of t/τ_c. In addition to the observation of a continuous increase in V_l over time, our results indicate that there is no evident dependence of V_l on the pulse energy and thus also for the Weber number. The independence of V_f/V_0 on the Weber number is expected when substituting the power laws $\dot{N}_f \tau_c \sim \mathrm{We}_d^{3/4}$ [cf. Fig. 6.1(c)] and $d_f \sim D_0\,\mathrm{We}_d^{-1/4}$ (cf. Sec. 6.2.2) into Eq. (6.2), yielding $V_f/V_0(t/\tau_c)$ that is determined by t/τ_c solely. The volume of ligaments scales as $V_l \sim w_l^2 N_l L_l \sim D_0^3 \mathrm{We}_d^{-1/8} L_l$ following $w_l \sim D_0 \mathrm{We}_d^{-1/4}$ and $N_l \sim \mathrm{We}_d^{3/8}$ [cf. Fig. 6.5 (b)]. The scaling would indeed be independent of the Weber number if here the relevant ligament length scales as $L_l \sim \mathrm{We}_d^{1/8}$, which is consistent with the scaling of the necking time $\sim \mathrm{We}_d^{-3/8}$ and radial flow speed $\sim \mathrm{We}_d^{1/2}$ which together set a typical length scale $\sim \mathrm{We}_d^{1/8}$. For the data shown in Fig. 6.6(b), the Weber number ranges from 1200 to 3300, thus giving a limited factor of 1.13 on V_l given by the postulated dependence on the Weber number $\mathrm{We}_d^{-1/8}$. More data, taken over a wider range of Weber number, would be required to experimentally verify the scaling of the ligament length.

The temporal evolution of V_f and V_l has been studied previously by Wang *et al.* [113] for water droplet impact on a pillar. In that work, the sum of ligament and fragment volume represents the liquid shed from the rim $V_{f+l} = V_l + V_f$. The ratio V_{f+l}/V_0, and the ratio V_f/V_0 contributing to it were separately shown to be functions of t/τ_c only and are independent of the droplet's Weber number. As a corollary, V_l/V_0 should also be a function of t/τ_c only, independent of the Weber number. Figures 6.6(a) and 6.6(b) show reasonable agreement between our experimental results and the predictions from Ref. [113]. The slightly lower volume channeled into the fragments, comparing to the model predictions, is shown to be offset by a modestly larger volume channeled into the ligaments — to yield a near-perfect agreement between model and experiment for V_{f+l}/V_0 in the applicable time domain, as shown in Fig. 6.6(c).

6.3   Volume of the center mass

During the expansion of the droplet, a disk-shaped feature may appear in the center of the sheet (cf. Fig. 1.2, Chapter 1). The formation of such a center mass is hypothesized to originate from early-time jetting and bursting, phenomena that could originate from laser-induced cavitation and its collapse inside the droplet [17, 37]. Such bursting

and jetting have also been observed by Klein *et al.* [17] for laser impact upon a liquid methyl-ethyl-ketone (MEK) droplet [see Fig. 6.7(e)].

In Chapter 2, we identified this center mass as a separate channel in the liquid distribution in the target, and excluded its volume from that of the sheet V_s. The thickness of the center-mass disk could not be directly assessed by the methods employed in the previous Chapters. However, our initial observations did indicate that
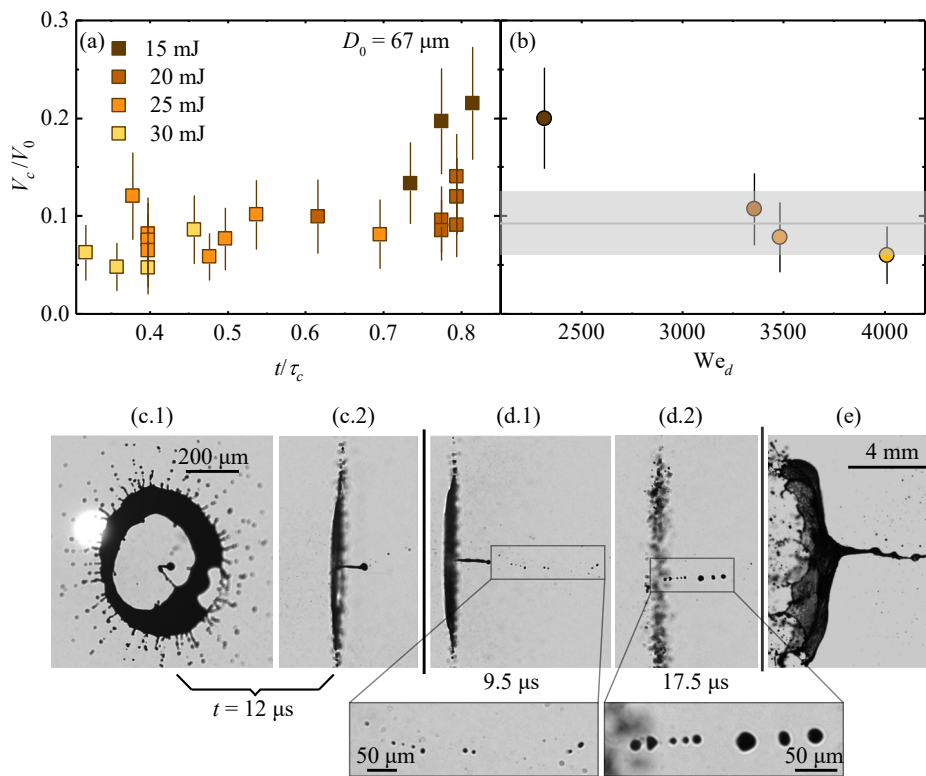

Figure 6.7: Volume ratio of the center mass to the initial droplet V_c/V_0 as a function of (a) t/τ_c, and (b) the Weber number We_d. In panel (b), the horizontal line at $V_c/V_0 = 9(3)$ % presents the average of the four data points; the number in the bracket gives the standard deviation, indicated by the shaded area around the horizontal line. (c.1),(c.2) Front & side-view of a sheet with its center mass and the associated center jet visible. (d.1),(d.2) Side-view images showing two examples of the center mass that reforms into a continuous stream [(d.1)] or a series of droplets [(d.2)]. The zoomed-in inset of (d.1) shows some fine droplets which detach from the jet at early times. (e) A side-view of a MEK liquid droplet impact by a laser pulse, taken and adapted from Ref. [17]. Note the change in length scale.

the center disk is significantly thicker than the surround sheet, and its contribution to the overall mass balance should thus be taken into account. During the sheet expansion, the center mass is bounded by a much thinner halo (cf. Fig. 2.1, Chapter 2). Meanwhile, spontaneously formed holes will appear on the sheet when the amplitude of capillary instabilities exceeds the thickness of the sheet [17]. These holes could open in the bounding halo of the center mass. Once the holes appear, the edges of these holes expand with the Taylor-Culick speed, which increases with decreasing local thickness. Therefore, the relatively thin halo around the center mass retreats promptly, separating the center mass from the rest of the sheet. This phenomenon ceases the exchange of liquid between the center mass and the sheet, effectively maintaining the amount of liquid of the center mass during the rest of the expansion. Figure 6.7(c.1) presents a front view of a sheet to exemplify the separation of the center mass from the rest of the liquid. The corresponding side-view image is shown in Fig. 6.7(c.2). As time passes, the detached center mass collapses as a result of the surface tension, forming either a spherical droplet or a center jet that can be described by the shape of a cylinder [see panels (c.2) and (d.1)]. The jet could further break into a series of small droplets due to a R-P instability, as shown in Fig. 6.7(d.2) with its inset showing a zoom-in on these droplets. Therefore, we are able to determine V_c by the volume of these associated geometries (i.e., the cylindrical liquid jet or spherical droplets) from our 90° side-view images with their improved resolution compared to our previous studies, and using the largest, 67 μm droplet size for optimum visibility.

Figures 6.7(a) and 6.7(b) show the volume ratio of the center mass to the initial droplet V_c/V_0 as a function of t/τ_c, and the Weber number We_d, respectively. Our results in Fig. 6.7(a) indicate that a 5–20% fraction of V_0 is channeled to the center mass, with the precise number depending on the experimental parameters. There is no evident dependence of V_c/V_0 on time. Figure 6.7(b) shows that a larger pulse energy appears to reduce the fraction of tin in V_c. Further studies are required to fully quantify and to clarify the origins of the center-mass feature. In particular, the influence of the initial droplet size needs to be addressed in future work: the droplet size dictates the acoustic timescale (see Sec. 6.7) and the deposited laser energy per droplet volume (cf. Ref [37]), which in turn characterize the degree of compressibility of the flow and could influence the formation of the center mass.

Averaging the available data in Fig. 6.7(b) yields a fraction of 9(3)% for the center mass, which we will use in the following discussion for the global volume distribution. We note that the obtained volume of the center mass may slightly underestimate the actual volume as some of the liquid shed from the center jet may appear in the form of fine particles, see the zoom-inset of Fig. 6.7(d.1). These particles detach at an early time from the center of the sheet and travel forward at high speeds. Therefore, they
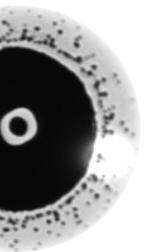
quickly move out of the scope of our side-view images and thus cannot be captured by our measurements.

6.4 Volume of ablated material

When a tin microdroplet is irradiated with a laser pulse, a fraction of liquid material at the surface of the droplet is transformed into plasma that expands away from the droplet. This expansion provides a momentum kick to the droplet, which results in a radial expansion and a propulsion velocity of the droplet along the laser direction [13, 14, 17, 30, 106]. The volume of ablated material V_a can be obtained from the data underlying Chapter 4, where detailed radiation-hydrodynamic simulations by RALEF-2D were performed to examine the partitioning of kinetic energy between propulsion and expansion. Based on simulations for two different droplet sizes $D_0 = 27$ and 45 μm, impacted by laser pulses with energy E_p ranging in 0.5–30 mJ and 20–104 μm (FWHM) beam size, the ablated material accounts for 5–23% of the initial amount of tin. With these numerical settings, the droplet is conditioned with a propulsion and expansion speed ranging from 30 to 250 m/s, yielding a wide range of Weber number from 600 to 15 000. The scaling of V_a/V_0 with We$_d$ and D_0 is highly non-trivial given the complex interplay of the underlying physical processes. The simulations show a monotonic increase of V_a/V_0 with increasing We$_d$ and a decrease with increasing D_0. A fit to the simulation data results in a very approximate, heuristic scaling relation of the ablated fraction $\sim D_0^{-\beta}\text{We}_d^{\gamma}$, with $0.6 \leq \beta \leq 0.8$ and $0.3 \leq \gamma \leq 0.5$. This scaling relation is only applicable for a limited parameter range and does not capture the full set of dependencies. For one of the industrially relevant cases studied, our simulations indicate that approximately 16 % of the total material will be ablated when a droplet with diameter of 27 μm is impacted by a laser pulse with energy of 4 mJ and beam diameter of 50 μm (FWHM). As a result, the droplet is accelerated to a speed of 144 m/s along the laser direction. Propelling the droplet with the same size instead to 219 m/s would require a laser pulse energy of 8 mJ, ablating 23 % of the initial mass, consistent with the approximate scaling relation.

6.5 Volume of the sheet

Given that the droplet expands into an axisymmetric sheet, the volume of the sheet can be determined by spatial integration of the thickness profile. In Chapter 2 and Chapter 3, this thickness profile — for a wide range of pulse energies and three different droplet sizes — were experimentally measured by (i) determining the opening velocity

(Taylor-Culick speed) of spontaneously formed holes on the sheet, and (ii) the partial transmissivity of the backlight through the sheet, and (iii) by using a probe pulse that gradually removes the liquid from the sheet. Our results revealed that a sheet with a thickness of several tens of nanometers is formed a few microseconds after the laser impact. The thickness profile $h(r)$ presents a slender spatial gradient, where h decreases with radial distance to the center of the sheet r. With further spatial integration, we provided the volume of the sheet V_s in a time range of $t/\tau_c \in (0.15, 0.7)$. The data of V_s indicates a continuous loss of tin from the sheet. Furthermore, we showed that the volume ratio V_s/V_0 depends on the non-dimensional time t/τ_c only and is independent of the Weber number.

In Chapter 2, we found a self-similar curve to which all data can be collapsed after rescaling by similarity variables [i.e., Eq. (2.6), Chapter 2]. This self-similar curve for the thickness in combination with the sheet expansion trajectory produces a description of the time evolution of the sheet volume V_s. We note that at early times, the slender-slope approximation [20, 24, 25, 54], underpinning the self-similarity, no longer applies to the sheet. As a result, we cannot expect that our self-similar curve for the thickness profile and the corresponding description for the sheet volume are valid for early-time dynamics.

6.6   Volume of the rim

The bounding rim can be described by the shape of a curved cylinder with a length of $2\pi R_r$ and a diameter of b_r. Therefore, its volume reads $V_r = (\pi^2/2) R_r b_r^2$. The length of the rim has been well captured by our experiments with the post-processing that determines the radial position of the rim [see Fig. 6.4(c)]. However, direct measurements of the thickness of the rim b_r are still lacking. Our experiments in Chapter 3 confirmed the presence of the rim, where it is directly visualized with a vaporization pulse that removes the fluid from the thin sheet. Regardless, the yet unknown mass fraction removed from the rim by the vaporization pulse prevents an accurate determination of b_r. Moreover, the sub-resolution size of b_r would make an estimation of its volume through direct optical inspection particularly challenging.

To still determine the volume of the rim, we employ the robust relation for the local Bond number $\mathrm{Bo} = \rho b_r^2 (-\ddot{R}_r)/\sigma = 1$ [i.e., Eq. (6.5)] that universally governs the instantaneous thickness of the rim [22]. The relation $\mathrm{Bo} = 1$ is valid for low viscous flow, which is applicable in our case where the Reynolds number $\mathrm{Re} = D_0 \dot{R}_0/\nu \sim 10^4$ given the viscosity $\nu = 0.27 \times 10^{-6}\,\mathrm{m^2/s}$ of liquid tin [114]. The deceleration of the rim $\ddot{R}_r$ that serves as input for the Bond number can be obtained by fitting a third-order

polynomial to the concatenated data of $R_r(t)$ in Fig. 5.4(c). The result of this fit was given by Eq. (5.3) in Chapter 5. Therefore, by using Eq. (6.5) for b_r and the fitting result of $R_r(t)$, the volume of the rim can be determined as

$$\frac{V_r}{V_0} = \frac{(\pi^2/2)R_r b_r^2}{\pi D_0^3/6}$$
$$= \frac{0.26}{0.93 - (t/\tau_c)}[(t/\tau_c)^3 - 2.79(t/\tau_c)^2 + 1.72(t/\tau_c) + 0.11]. \tag{6.7}$$

Equation (6.7) indicates that V_r/V_0 is a function of t/τ_c only. This is expected as $b_r^2 \sim D_0^2 \mathrm{We}_d^{-1/2}$ and $R_r \sim D_0 \mathrm{We}^{1/2}$. Thus, $b_r^2 R_r/D_0^3$ is independent of the droplet's Weber number. Note that Eq. (6.7) for V_r/V_0 is different from Eq. (2.11) in Chapter 2, where the rim expansion trajectory $R_r(t)$ from Ref. [24] was applied instead.

6.7 Discussion: global mass partitioning

So far, we have discussed the volume fraction of liquid taken up by various channels. In our experiments, we systematically alter the Weber number $\mathrm{We}_d = \rho \dot{R}_0^2 D_0/\sigma$ by varying the droplet diameter D_0 and the pulse energy E_p, which jointly condition the different initial expansion speeds of droplets $\dot{R}_0$.

We have shown that for a given D_0, the volume fractions taken up by fragments V_f/V_0, ligaments V_l/V_0, rim V_r/V_0, and sheet V_s/V_0 are independent of the Weber number and can be described as functions of t/τ_c. Our experimental results suggest a dependence of V_c/V_0 on the Weber number. However, this mass channel provides a relatively small contribution of approximately 9% for the relevant cases. This volume fraction is constant over the accessible time. The ablated fraction V_a is not readily captured in a scaling relation but can be shown to increase with increasing We_d and decrease with increasing D_0.

These observations allow us to summarize the complete liquid distribution in these channels in a graph where the non-dimensional time t/τ_c is the only characteristic parameter. This graph will be discussed in the following. We exclude the volume of ablated material V_a from the graph given that the material ablation occurs instantly (within 10 ns) after the start of the laser pulse and hence V_a is not a variable changing with t/τ_c throughout the droplet expansion process. We note that our discussion is based on the assumption that the density of liquid tin remains constant in our observation time regime ($\sim \mu$s). This assumption is valid in our case where the laser-generated plasma shields the liquid surface from direct laser irradiation. Even in
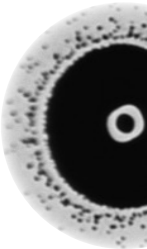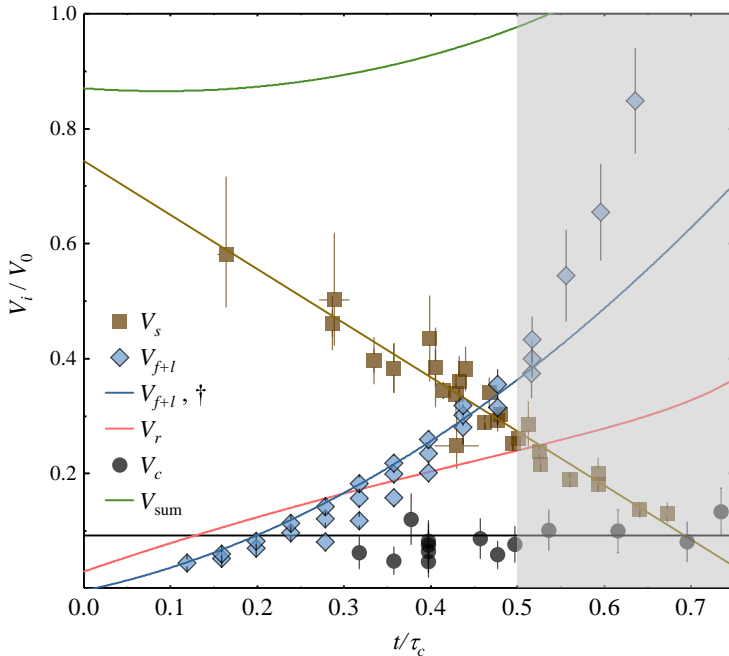
Figure 6.8: Volume fraction of different channels with respect to the initial droplet V_0 as a function of t/τ_c. The volume of the sheet V_s is reproduced from the experimental data presented in Chapter 2 and Chapter 3, along with a linear fit. The summed volume of fragments and ligaments V_{f+l} is from Fig. 6.6(c), along with the prediction on V_{f+l} from Ref. [113] (†). The red line represents Eq. (6.7) for the volume of the rim V_r. The volume of the center mass V_c is reproduced from Fig. 6.7(a), along with a horizontal line at 9 %, i.e., the mean values of the data shown in Fig. 6.7(b). The sum of all these channels $V_{sum} = V_s + V_{f+l} + V_r + V_c$ is plotted by a green line. The shaded area indicate the temporal range of $t > 0.5\tau_c$ where the assumptions underpinning the models are invalid (see the main text).

extreme cases most of the sheet's liquid has a temperature < 1000 K, which would lead to a modest decrease of 5% in the liquid density w.r.t. the density at melting point[1]. We also assume that the response of the droplet to a 10-ns-length (FHWM) laser pulse is dominated by incompressible flow. The validity of this assumption is supported by Chapter 4 where our results of kinetic energy partitioning were shown to agree with an analytical fluid-dynamic model developed by Gelderblom *et al.* [14]

---

[1]To support this, an example case of RALEF-2D simulation is investigated where a droplet with $D_0 = 30\ \mu$m is irradiated with a particularly energetic laser pulse with $E_p = 80$ mJ, a beam diameter of $60\ \mu$m (flattop), and a pulse duration of 20 ns (square). At $t = 21$ ns (i.e., 1 ns after laser off), most of the liquid has a temperature < 1021 K, at which the density of liquid tin is 6641 kg/m^3, 4.7% less than the density at the melting point of tin (6970 kg/m^3 at 507 K) [118].

for an incompressible liquid droplet responding to an instantaneous pressure impulse. The assumption is further supported by the studies by Reijer *et al.* [45] and Meijer *et al.* [38] which conclude that an incompressible flow will dominate the droplet response when $\tau_p/\tau_a \gtrsim 1$ for a Gaussian-temporally-shaped pulse; $\tau_a = R_0/c_s$ is the acoustic time which characterizes the acoustic wave that traverses the droplet at the speed of sound $c_s \approx 2500\,\mathrm{m/s}$ [102]. In our case, the pulse duration satisfies $\tau_p \gtrsim \tau_a$ to a sufficient degree. Still, we do find some compressibility effects as we hypothesize that the center-mass feature is a result of the collapse of a cavity generated by a rarefaction wave (cf. Sec. 6.3).

Figure 6.8 presents the volume ratio of the channels (except V_a) listed in Eq. (6.1) as functions of t/τ_c. The data for V_s from Chapters 2 and 3 are reproduced in the graph[2]. Furthermore, we sum up the volume of these channels, that is, $V_{\mathrm{sum}} = V_s + V_r + V_c + V_{f+l}$. To plot V_{sum}/V_0, a linear fit is performed to the data of V_s/V_0 in order to produce a continuous description of V_s based on experimental data. For a continuous description of V_{f+l}, the model from Ref. [113] is used. This model has been shown to agree with our experimental data [cf. Fig. 6.6(c)]. For the volume of the center mass, a constant fraction of 9% is added to V_{sum}/V_0 given the fact that there is no evident dependence of V_c/V_0 on t/τ_c for the fixed droplet size $D_0 = 67\,\mu m$ presented in Fig. 6.7. The obtained V_{sum}/V_0 is represented by a green curve in Fig. 6.8. Our results indicate that V_{sum}/V_0 captures approximately 90% of the original droplet volume in the applicable domain. The "missing" volume fraction of $\sim 10\%$ to V_{sum}/V_0 is consistent with the expected volume of the ablated material V_a/V_0 which accounts for 5–23% (cf. Sec. 6.4). Therefore, we have equalized both sides of Eq. (6.1) with reasonable accuracy. This observation is remarkable given the complexity of the interplay between the underlying physical processes, and the experimental and theoretical approaches as represented in Fig. 6.8. We note that V_{sum} becomes larger with increasing time. This observation could be an intrinsic consequence of the higher pulse energies and smaller droplets that correspond to the data of V_s for the early times [cf. Fig 2.4(b), Chapter 2 and Fig. 3.2(c), Chapter 3], effectively leading to a larger fraction of ablated material and hence a smaller V_{sum}.

6.8 Application perspective

We will now apply our results to the industrial context associated with EUV nano-lithography. In particular, we will provide recommendations on how to optimize the

---

[2]Note the different definition of the capillary time comparing this Chapter to Chapters 2 and 3.

dual-pulse (i.e., prepulse – main pulse) EUV generation system on minimizing the contaminating debris, and on maximizing the mass-efficiency for EUV generation.

Shoot early (main pulse), shoot hard (prepulse)

Our results enable quantifying the loss of tin volume from the sheet, over the rim, ligaments, and eventually to fragments. The volume ratio of these channels with respect to the original droplet volume can be characterized by the non-dimensional time $t/\tau_c = t/[\rho D_0^3/(6\sigma)]^{1/2}$ solely. In other words, given a droplet diameter D_0, time is the key parameter determining the tin volume distribution in a target. As a corollary, to minimize the tin lost from the sheet to the fragments, it is best that the successive main pulse or the vaporization pulse following the prepulse starts with a minimum time delay (i.e., "shoot early"). To allow the tin target to reach a sufficient size in this short time to provide an optimal geometrical overlap with the large main pulse, an energetic prepulse is needed to induce a higher expansion rate of the droplet (i.e., "shoot hard"). Furthermore, as a direct result of a larger V_s, a larger sheet thickness will be available (i.e., more tin is available for interacting with the main pulse), and scaling to larger main pulse energies — and more output EUV light — may be feasible in this case.

Once the sheet starts to fragment, the first (and fastest) fragments generated move with a speed close to that of the initial expansion rate of the rim $\dot{R}_0$ (see Fig. 5.5, Chapter 5 and Fig. 3.1, Chapter 3). The trajectory of these outermost fragments defines a boundary of the region in which the liquid debris is distributed. Given the fact that the fragments follow ballistic trajectories, and that the sheet expansion continuously decelerates under the action of surface tension, our *shoot early, shoot hard* solution will also lead to a smaller area over which the liquid debris dispersed: at equal sheet "target" size, the outer fragments are closer to the rim.

A customized spatial profile of the main pulse & vaporization pulse

In addition to the global picture of material distribution, we provided details of local morphology of a sheet including the spatial profile of the sheet thickness, and the presence of the center mass and a thick rim. A predefined spatial shape of the main pulse or the vaporization pulse could be implemented in such a way that it relates to the spatial characteristics of the sheet (see Fig. 6.9). This approach may lead to a more efficient utilization of the tin material and reduce the required laser energy in the EUV light generation process. Specifically, the local fluence of the vaporization pulse may be matched to the local thickness of the sheet (cf. Chapter 3).
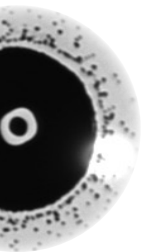
Furthermore, at a given time the local amount of tin distributed in fragments is determined jointly by fragment size (Fig. 6.3), fragment ballistic trajectory (Fig. 5.5), and fragment shedding rate (Fig. 6.1). Here, we envision spatially tailoring a vaporization pulse to specifically target the outermost fragments, now of known size, which may not interact with the main laser pulse. An example case of the spatial distribution of tin on sheet targets calculated based on the results of this thesis is shown in Fig. 6.9 (see caption for details).
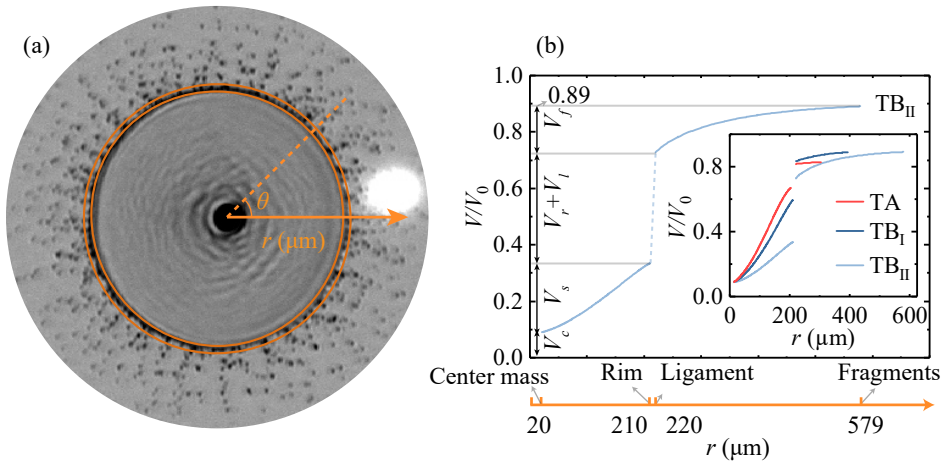
Figure 6.9: Spatial distribution of liquid tin volume on targets A, B_I, and B_{II} previously discussed in Chapter 3. Briefly, these targets were obtained by using laser pulses with $E_p = 12$ mJ (Target A) and 20 mJ (Target B_I, B_{II}), respectively, focused down do a spot size of 55 μm at the location of the droplet which has a diameter of $D_0 = 29$ μm. (a) A front-view shadowgraphy image of Target B_{II}. The contrast of the image is modified for a better visual on the fine rim, ligaments, and fragments. The image is horizontally stretched to correct for the $30°$ observation angle. A polar coordinate (r, θ) with its origin at the center of the sheet is depicted. We also draw two concentric circles, with the inner one (with a radius of 210 μm) representing the location of the rim, and the outer one (with a radius of $210 + 10$ μm) indicating the approximate position of the ligament tip. (b) The cumulative volume fraction of tin as a function of r for target B_{II}, while the results for Target A and B_I are included in the inset. The r-axis in the polar coordinate [depicted in (a)] is plotted at the bottom, with the radial position of the center-mass' edge (20 μm), rim (210 μm), ligament tip (220 μm), and the outermost fragments (579 μm). For all three targets, the volume fraction taken up the center mass is set as 9%. The segment curves representing the sheet volume are determined by integrating the thickness profile $h(r)$ shown in Fig. 3.2(a), Chapter 3. The volume fractions taken by the rim and ligaments are determined by Eq. (6.7), and by V_l shown in Fig. 6.6(b), respectively. Curves that represent fragment volume are obtained by combining the descriptions of fragment speeds provided by Fig. 5.5, Chapter 5, and the data of V_f presented in Fig. 6.6(a). Our results show a steep gradient of the mass distribution at the rim and ligaments: for target B_{II} almost 40% of the total mass is located within a narrow ring with a width of approximately 10 μm. This "localized mass" could be a source of inefficient usage of the tin by the main pulse or the second prepulse (see the main text).

Bibliography

[1] A. Guzman, *20 breakthroughs from 20 years of science aboard the ISS*, 2020.

[2] M. Javaid, A. Haleem, R. P. Singh, and R. Suman, "Artificial intelligence applications for industry 4.0: A literature-based study," *J. Ind. Inf. Integr.*, vol. 07, no. 01, pp. 83–111, 2022.

[3] G. E. Moore, "Lithography and the future of Moore's law," *Proc. SPIE*, vol. 2439, pp. 2439 –2439 –16, 1995.

[4] J. van Schoot, K. Troost, F. Bornebroek, R. van Ballegoij, S. Lok, P. Krabbendam, J. Stoeldraijer, J. Benschop, J. Finders, H. Meiling, E. van Setten, B. Kneer, P. Kuerz, W. Kaiser, T. Heil, and S. Migura, "The future of EUV lithography: continuing Moore's Law into the next decade," *Proc. SPIE*, vol. 10583, 2018.

[5] R. F. Pease and S. Y. Chou, "Lithography and Other Patterning Techniques for Future Electronics," *Proc. IEEE*, vol. 96, no. 2, pp. 248–270, 2008.

[6] P. VanZant, *Microchip fabrication: a practical guide to semiconductor processing*. McGraw-Hill, 2014.

[7] A. J. den Boef, "Optical wafer metrology sensors for process-robust CD and overlay control in semiconductor device manufacturing," *Surf. Topogr.*, vol. 4, no. 2, p. 023 001, 2016.

[8] B. Wu and A. Kumar, "Extreme ultraviolet lithography: A review," *J. Vac. Sci. Technol. B*, vol. 25, no. 6, pp. 1743–1761, 2007.

[9] C. Wagner and N. Harned, "Lithography gets extreme," *Nat. Photonics*, vol. 4, no. 1, pp. 24–26, 2010.

[10] D. G. Stearns, R. S. Rosen, and S. P. Vernon, "Multilayer mirror technology for soft-x-ray projection lithography," *Appl. Opt.*, vol. 32, no. 34, pp. 6952–6960, 1993.

[11] I. Fomenkov, "EUV Source for High Volume Manufacturing: Performance at 250 W and Key Technologies for Power Scaling," *Proceedings of 2017 International Workshop on EUV and Soft X-Ray Sources, Dublin*, 2017.

[12] I. Fomenkov, D. Brandt, A. Ershov, A. Schafgans, Y. Tao, G. Vaschenko, S. Rokitski, M. Kats, M. Vargas, M. Purvis, R. Rafac, B. La Fontaine, S. De Dea, A. LaForge, J. Stewart, S. Chang, M. Graham, D. Riggs, T. Taylor, M. Abraham, and D. Brown, "Light sources for high-volume manufacturing EUV lithography: technology, performance, and power scaling," *Adv. Opt. Technol.*, vol. 6, no. 3-4, pp. 173–186, 2017.

[13] D. Kurilovich, A. L. Klein, F. Torretti, A. Lassise, R. Hoekstra, W. Ubachs, H. Gelderblom, and O. O. Versolato, "Plasma propulsion of a metallic microdroplet and its deformation upon laser impact," *Phys. Rev. Appl.*, vol. 6, p. 014 018, 1 2016.

[14] H. Gelderblom, H. Lhuissier, A. L Klein, W. Bouwhuis, D. Lohse, E. Villermaux, and J. H. Snoeijer, "Drop deformation by laser-pulse impact," *J. Fluid Mech.*, vol. 794, pp. 676–699, 2016.

[15] B. Liu, R. A. Meijer, J. Hernandez-Rueda, D. Kurilovich, Z. Mazzotta, S. Witte, and O. O. Versolato, "Laser-induced vaporization of a stretching sheet of liquid tin," *J. Appl. Phys.*, vol. 129, no. 5, p. 053 302, 2021.

[16] B. Liu, D. Kurilovich, H. Gelderblom, and O. O. Versolato, "Mass loss from a stretching semitransparent sheet of liquid tin," *Phys. Rev. Applied*, vol. 13, p. 024 035, 2 2020.

[17] A. L. Klein, D. Kurilovich, H. Lhuissier, O. O. Versolato, D. Lohse, E. Villermaux, and H. Gelderblom, "Drop fragmentation by laser-pulse impact," *J. Fluid Mech.*, vol. 893, A7, 2020.

[18] V. Y. Banine, K. N. Koshelev, and G. H. P. M. Swinkels, "Physical processes in EUV sources for microlithography," *J. Phys. D*, vol. 44, no. 25, p. 253 001, 2011.

[19] I. Fomenkov, A. Schafgans, and D. Brandt, "Laser-produced plasma sources for high-volume-manufacturing euv lithography," *Synchrotron Radiation News*, vol. 32, no. 4, pp. 3–8, 2019.

[20] Y. Wang and L. Bourouiba, "Drop impact on small surfaces: Thickness and velocity profiles of the expanding sheet in the air," *J. Fluid Mech.*, vol. 814, no. 1, pp. 510–534, 2017.

[21] L. Wang Y. and Bourouiba, "Unsteady sheet fragmentation: Droplet sizes and speeds," *J. Fluid Mech.*, vol. 848, 946–967, 2018.

[22] Y. Wang, R. Dandekar, N. Bustos, S. Poulain, and L. Bourouiba, "Universal rim thickness in unsteady sheet fragmentation," *Phys. Rev. Lett.*, vol. 120, p. 204 503, 2018.

[23] Y. Wang and L. Bourouiba, "Growth and breakup of ligaments in unsteady fragmentation," *J. Fluid Mech.*, vol. 910, A39, 2021.

[24] E. Villermaux and B. Bossa, "Drop fragmentation on impact," *J. Fluid Mech.*, vol. 668, pp. 412–435, 2011.

[25] J. Eggers, M. Fontelos, C. Josserand, and S Zaleski, "Drop dynamics after impact on a solid wall: Theory and simulations," *Phys. Fluids*, vol. 22, no. 1, p. 1063, 2010.

[26] G. Riboux and J. M. Gordillo, "Experiments of Drops Impacting a Smooth Solid Surface: A Model of the Critical Impact Speed for Drop Splashing," *Phys. Rev. Lett.*, vol. 113, no. 2, p. 024 507, 2014.

[27] G. Riboux and J. M. Gordillo, "The diameters and velocities of the droplets ejected after splashing," *J. Fluid Mech.*, vol. 772, pp. 630–648, 2015.

[28] A. L. Klein, W. Bouwhuis, C. W. Visser, H. Lhuissier, C. Sun, J. H. Snoeijer, E. Villermaux, D. Lohse, and H. Gelderblom, "Drop Shaping by Laser-Pulse Impact," *Phys. Rev. Appl.*, vol. 3, no. 4, p. 044 018, 2015.

[29] A. L. Klein, C. W. Visser, W. Bouwhuis, H. Lhuissier, C. Sun, J. H. Snoeijer, E. Villermaux, D. Lohse, and H. Gelderblom, "Laser impact on a drop," *Phys. Fluids*, vol. 27, no. 9, p. 091 106, 2015.

[30] D. Kurilovich, M. M. Basko, D. A. Kim, F. Torretti, R. Schupp, J. C. Visschers, J. Scheers, R. Hoekstra, W. Ubachs, and O. O. Versolato, "Power-law scaling of plasma pressure on laser-ablated tin microdroplets," *Phys. Plasmas*, vol. 25, p. 012 709, 1 2018.

[31] D. Hudgins, N. Gambino, B. Rollinger, and R. Abhari, "Neutral cluster debris dynamics in droplet-based laser-produced plasma sources," *J. Phys. D*, vol. 49, no. 18, p. 185 205, 2016.

[32] C. W. Visser, P. E. Frommhold, S. Wildeman, R. Mettin, D. Lohse, and C. Sun, "Dynamics of high-speed micro-drop impact: Numerical simulations and experiments at frame-to-frame times below 100 ns," *Soft Matter*, vol. 11, no. 9, pp. 1708–1722, 2015.

[33] J. Philippi, P.-Y. Lagrée, and A. Antkowiak, "Drop impact on a solid surface: Short-time self-similarity," *J. Fluid Mech.*, vol. 795, 96–135, 2016.

[34] I. V. Roisman, "Inertia dominated drop collisions. ii. an analytical solution of the navier–stokes equations for a spreading viscous film," *Physics of Fluids*, vol. 21, no. 5, p. 052 104, 2009.

[35] S. T. Thoroddsen, K. Takehara, and T. G. Etoh, "Micro-splashing by drop impacts," *J. Fluid Mech.*, vol. 706, 560–570, 2012.

[36] D. Kurilovich, "Laser-induced dynamics of liquid tin microdroplets," English, Ph.D. dissertation, Vrije Universiteit Amsterdam, 2019.

[37] R. Meijer, "Tailored laser-droplet interaction: For target formation in extreme ultraviolet sources," English, Ph.D. dissertation, Vrije Universiteit Amsterdam, 2021.

[38] R. A. Meijer, D. Kurilovich, K. S. E. Eikema, O. O. Versolato, and S. Witte, "The transition from short- to long-timescale pre-pulses: Laser-pulse impact on tin microdroplets," *J. Appl. Phys.*, vol. 131, no. 10, p. 105 905, 2022.

[39] Y. Tao, M. S. Tillack, K. L. Sequoia, R. A. Burdt, S. Yuspeh, and F. Najmabadi, "Efficient 13.5 nm extreme ultraviolet emission from sn plasma irradiated by a long CO_2 laser pulse," *Appl. Phys. Lett.*, vol. 92, no. 25, p. 251 501, 2008.

[40] J. Benschop, V. Banine, S. Lok, and E. Loopstra, "Extreme ultraviolet lithography: Status and prospects," *J. Vac. Sci. Technol. B*, vol. 26, no. 6, pp. 2204–2207, 2008.

[41] S. Fujioka, M. Shimomura, Y. Shimada, S. Maeda, H. Sakaguchi, Y. Nakai, T. Aota, H. Nishimura, N. Ozaki, A. Sunahara, K. Nishihara, N. Miyanaga, Y. Izawa, and K. Mima, "Pure-tin microdroplets irradiated with double laser pulses for efficient and minimum-mass extreme-ultraviolet light source production," *Appl. Phys. Lett.*, vol. 92, no. 24, p. 241 502, 2008.

[42] V. Y. Banine, K. N. Koshelev, and G. H. P. M. Swinkels, "Physical processes in EUV sources for microlithography," *J. Phys. D*, vol. 44, no. 25, p. 253 001, 2011.

[43] O. O. Versolato, "Physics of laser-driven tin plasma sources of EUV radiation for nanolithography," *Plasma Sources Sci. Technol.*, vol. 28, no. 8, p. 083 001, 2019.

[44] R. W. Coons, S. S. Harilal, D. Campos, and A. Hassanein, "Analysis of atomic and ion debris features of laser-produced Sn and Li plasmas," *J. Appl. Phys.*, vol. 108, no. 6, p. 063 306, 2010.

[45] S. A. Reijers, J. H. Snoeijer, and H. Gelderblom, "Droplet deformation by short laser-induced pressure pulses," *J. Fluid Mech.*, vol. 828, pp. 374–394, 2017.

[46] C. Vernay, L. Ramos, and C. Ligoure, "Free radially expanding liquid sheet in air: Time- and space-resolved measurement of the thickness field," *J. Fluid Mech.*, vol. 764, pp. 428–444, 2015.

[47] S. Kooij, R. Sijs, M. M. Denn, E. Villermaux, and D. Bonn, "What determines the drop size in sprays?" *Phys. Rev. X*, vol. 8, no. 3, p. 031 019, 2018.

[48] G. Cisneros, J. S. Helman, and C. N. J. Wagner, "Dielectric function of liquid tin between 250 and 1100 °C," *Phys. Rev. B*, vol. 25, no. 6, pp. 4248–4251, 1982.

[49] F. E. C. Culick, "Comments on a ruptured soap film," *J. Appl. Phys.*, vol. 31, no. 1, pp. 1128–1129, 1960.

[50] D. Kurilovich, T. de Faria Pinto, F. Torretti, R. Schupp, J. Scheers, A. S. Stodolna, H. Gelderblom, K. S. Eikema, S. Witte, W. Ubachs, R. Hoekstra, and O. O. Versolato, "Expansion Dynamics after Laser-Induced Cavitation in Liquid Tin Microdroplets," *Phys. Rev. Applied*, vol. 10, p. 054 005, 5 2018.

[51] J. A. Stratton, *Electromagnetic Theory*, 2nd. McGraw-Hill book company, inc., New York and London, 1941.

[52] N. Bremond and E. Villermaux, "Bursting thin liquid films," *J. Fluid Mech.*, vol. 524, pp. 121–130, 2005.

[53] A. Rozhkov, B. Prunet-Foch, and M. Vignes-Adler, "Dynamics of a liquid lamella resulting from the impact of a water drop on a small target," *Proc. Royal Soc. Lond.*, vol. 460, no. 2049, pp. 2681–2704, 2004.

[54] H. Lastakowski, F. Boyer, A.-L. Biance, C. Pirat, and C. Ybert, "Bridging local to global dynamics of drop impact onto solid substrates," *J. Fluid Mech.*, vol. 747, pp. 103–118, 2014.

[55] F. Torretti, J. Sheil, R. Schupp, M. Basko, M. Bayraktar, R. Meijer, S. Witte, W. Ubachs, R. Hoekstra, O. Versolato, *et al.*, "Prominent radiative contributions from multiply-excited states in laser-produced tin plasma for nanolithography," *Nat. Commun.*, vol. 11, no. 1, pp. 1–8, 2020.

[56] A. L. Klein, W. Bouwhuis, C. W. Visser, H. Lhuissier, C. Sun, J. H. Snoeijer, E. Villermaux, D. Lohse, and H. Gelderblom, "Drop shaping by laser-pulse impact," *Phys. Rev. Appl.*, vol. 3, no. 4, p. 044 018, 2015.

[57] Y. Tao, J. T. Stewart, J. Jur, A. LaForge, D. Brown, M. J. Arcand, A. A. Schafgans, and M. A. Purvis, "Extreme ultraviolet light source," Patent US 20160007434A1, ASML Netherlands B.V., US Patent 20160007434A1, Jan. 7, 2016.

[58] M. Purvis, I. V. Fomenkov, A. A. Schafgans, P. Mayer, K. Hummler, M. H. Leenders, Y. Tao, S. I. Rokitski, J. Stewart, A. I. Ershov, R. J. Rafac, S. D. Dea, G. O. Vaschenko, D. C. Brandt, and D. J. Brown, "Laser-produced plasma incoherent EUV light sources for high-volume manufacturing semiconductor lithography (Conference Presentation)," *X-Ray Lasers and Coherent X-Ray Sources: Development and Applications XIII*, A. Klisnick and C. S. Menoni, Eds., vol. 11111, SPIE, 2019.

[59] S. A. Reijers, D. Kurilovich, F. Torretti, H. Gelderblom, and O. O. Versolato, "Laser-to-droplet alignment sensitivity relevant for laser-produced plasma sources of extreme ultraviolet light," *J. Appl. Phys.*, vol. 124, no. 1, p. 013 102, 2018.

[60] R. A. Meijer, A. S. Stodolna, K. S. E. Eikema, and S. Witte, "High-energy Nd:YAG laser system with arbitrary sub-nanosecond pulse shaping capability," *Opt. Lett.*, vol. 42, no. 14, pp. 2758–2761, 2017.

[61] J. Blaisot and J. Yon, "Droplet size and morphology characterization for dense sprays by image processing: Application to the diesel spray," *Exp. Fluids*, vol. 39, pp. 977–994, 2 2005.

[62] M. S. Qaisar and G. J. Pert, "Laser ablation of Mg, Cu, and Pb using infrared and ultraviolet low-fluence lasers," *J. Appl. Phys.*, vol. 94, no. 3, pp. 1468–1477, 2003.

[63] C. Porneala and D. A. Willis, "Time-resolved dynamics of nanosecond laser-induced phase explosion," *J. Phys. D*, vol. 42, no. 15, p. 155 503, 2009.

[64] V. Bakshi, *EUV Lithography*. SPIE Press, Bellingham, 2018.

[65] T. Sizyuk and A. Hassanein, "Tuning laser wavelength and pulse duration to improve the conversion efficiency and performance of EUV sources for nanolithography," *Phys. Plasmas*, vol. 27, no. 10, p. 103 507, 2020.

[66] S. Churilov and A. Ryabtsev, "Analysis of the spectra of In XII–XIV and Sn XIII–XV in the far-VUV region," *Opt. Spectrosc.*, vol. 101, no. 2, pp. 169–178, 2006.

[67] A. Ryabtsev, É. Y. Kononov, and S. Churilov, "Spectra of rubidium-like Pd X-Sn XIV ions," *Opt. Spectrosc.*, vol. 105, no. 6, pp. 844–850, 2008.

[68] G. O'Sullivan, B. Li, R. D'Arcy, P. Dunne, P. Hayden, D. Kilbane, Tom McCormack, H. Ohashi, F. O'Reilly, P. Sheridan, E. Sokell, C. Suzuki, and Takeshi Higashiguchi, "Spectroscopy of highly charged ions and its relevance to EUV and soft x-ray source development," *J. Phys. B*, vol. 48, no. 14, p. 144 025, 2015.

[69] J. Scheers, C. Shah, A. Ryabtsev, H. Bekker, F. Torretti, J. Sheil, D. A. Czapski, J. C. Berengut, W. Ubachs, J. R. C. López-Urrutia, R. Hoekstra, and O. O. Versolato, "Euv spectroscopy of highly charged $Sn^{13+} - Sn^{15+}$ ions in an electron-beam ion trap," *Phys. Rev. A*, vol. 101, p. 062 511, 6 2020.

[70] J. Sheil, O. O. Versolato, A. J. Neukirch, and J. Colgan, "Multiply-excited states and their contribution to opacity in CO_2 laser-driven tin-plasma conditions," *J. Phys. B: At. Mol. Opt. Phys.*, vol. 54, no. 3, p. 035 002, 2021.

[71] H. Mizoguchi, T. Abe, Y. Watanabe, T. Ishihara, T. Ohta, T. Hori, A. Kurosu, H. Komori, K. Kakizaki, A. Sumitani, O. Wakabayashi, H. Nakarai, J. Fujimoto, and A. Endo, "First generation laser-produced plasma source system for HVM EUV lithography," *Proc. SPIE*, vol. 7636, p. 763 608, 2010.

[72] V. Y. Banine, K. N. Koshelev, and G. H. P. M. Swinkels, "Physical processes in EUV sources for microlithography," *J. Phys. D*, vol. 44, no. 25, p. 253 001, 2011.

[73] E. Louis, A. Yakshin, T. Tsarfati, and F. Bijkerk, "Nanometer interface and materials control for multilayer euv-optical applications," *Prog. Surf. Sci*, vol. 86, no. 11, pp. 255–294, 2011.

[74] D. J. Hemminga, L Poirier, M. M. Basko, R Hoekstra, W Ubachs, O. O. Versolato, and J Sheil, "High-energy ions from nd:YAG laser ablation of tin microdroplets: Comparison between experiment and a single-fluid hydrodynamic model," *Plasma Sources Sci. Technol.*, vol. 30, no. 10, p. 105 006, 2021.

[75] M. M. Basko, V. G. Novikov, and A. S. Grushin, "On the structure of quasi-stationary laser ablation fronts in strongly radiating plasmas," *Phys. Plasmas*, vol. 22, no. 5, p. 053 111, 2015.

[76] C. Josserand and S. T. Thoroddsen, "Drop impact on a solid surface," *Annu. Rev. Fluid Mech.*, vol. 48, pp. 365–91, 2016.

[77] S. Wildeman, C. W. Visser, C. Sun, and D. Lohse, "On the spreading of impacting drops," *J. Fluid Mech.*, vol. 805, 636–655, 2016.

[78] C. Clanet, C. Béguin, D. Richard, and D. Quéré, "Maximal deformation of an impacting drop," *J. Fluid Mech.*, vol. 517, pp. 199–208, 2004.

[79] Y. Wang, "Fundamentals in unsteady fluid fragmentation from drop impact," Ph.D. dissertation, Massachusetts Institute of Technology, 2021.

[80] T. de Faria Pinto, J. Mathijssen, R. Meijer, H. Zhang, A. Bayerle, D. Kurilovich, O. O. Versolato, K. S. Eikema, and S. Witte, "Cylindrically and non-cylindrically symmetric expansion dynamics of tin microdroplets after ultrashort laser pulse impact," *Appl. Phys. A*, vol. 127, no. 2, pp. 1–10, 2021.

[81] R. A. Meijer, R. Schupp, J. Sheil, M. M. Basko, K. S. E. Eikema, O. O. Versolato, and S. Witte, "Spall-velocity reduction in double-pulse impact on tin microdroplets," *Phys. Rev. Applied*, vol. 16, p. 024 026, 2 2021.

[82] J. Hermens, H. Gelderblom, B. Liu, J. Duffhues, P. Rindt, and O. O. Versolato, "Laser-impact-induced splashing: An analysis of the splash crown evolution after Nd:YAG ns-pulse laser impact on a liquid tin pool," *Appl. Phys. B*, vol. 127, p. 44, 2021.

[83] M. M. Basko, J. A. Maruhn, and A. Tauschwitz, "Development of a 2D radiation-hydrodynamics code RALEF for laser plasma simulations," GSI Helmholtzzentrum für Schwerionenforschung GmbH, GSI Report 2010-1, PLASMA-PHYSICS-25, 2010.

[84] M. M. Basko, P. V. Sasorov, M Murakami, V. G. Novikov, and A. S. Grushin, "One-dimensional study of the radiation-dominated implosion of a cylindrical tungsten plasma column," *Plasma Phys. Control.*, vol. 54, no. 5, p. 055 003, 2012.

[85] A. Tauschwitz, M. Basko, A. Frank, V. Novikov, A. Grushin, A. Blazevic, M. Roth, and J. Maruhn, "2D radiation-hydrodynamics modeling of laser-plasma targets for ion stopping measurements," *High Energy Density Phys.*, vol. 9, no. 1, pp. 158–166, 2013.

[86] S. Faik, A. Tauschwitz, M. M. Basko, J. A. Maruhn, O. Rosmej, T. Rienecker, V. G. Novikov, and A. S. Grushin, "Creation of a homogeneous plasma column by means of hohlraum radiation for ion-stopping measurements," *High Energy Density Phys.*, vol. 10, pp. 47–55, 2014.

[87] M. M. Basko, "On the maximum conversion efficiency into the 13.5-nm extreme ultraviolet emission under a steady-state laser ablation of tin microspheres," *Phys. Plasmas*, vol. 23, no. 8, p. 083 114, 2016.

[88] M. M. Basko, M. S. Krivokorytov, A. Y. Vinokhodov, Y. V. Sidelnikov, V. M. Krivtsun, V. V. Medvedev, D. A. Kim, V. O. Kompanets, A. A. Lash, and K. N. Koshelev, "Fragmentation dynamics of liquid–metal droplets under ultra-short laser pulses," *Laser Phys. Lett.*, vol. 14, no. 3, p. 036 001, 2017.

[89] R. Schupp, L. Behnke, J. Sheil, Z. Bouza, M. Bayraktar, W. Ubachs, R. Hoekstra, and O. O. Versolato, "Characterization of 1-and 2-μm wavelength laser-produced microdroplet-tin plasma for generating extreme-ultraviolet light," *Phys. Rev. Research*, vol. 3, p. 013 294, 1 2021.

[90] F. L. Addessio, J. R. Baumgardner, J. K. Dukowicz, N. L. Johnson, B. A. Kashiwa, R. M. Rauenzahn, and C. Zemach, *CAVEAT: A computer code for fluid dynamics problems with large distortion and internal slip*, Report No. LA-10613-MS-Rev. 1, UC-32, Los Alamos National Laboratory, 1992.

[91] E. Livne and A. Glasner, "A finite difference scheme for the heat conduction equation," *J. Comput. Phys.*, vol. 58, no. 1, pp. 59–66, 1985.

[92] M. M. Basko, J. A. Maruhn, and A. Tauschwitz, "An efficient cell-centered diffusion scheme for quadrilateral grids," *J. Comput. Phys.*, vol. 228, no. 6, pp. 2175–2193, 2009.

[93] A. Dedner and P. Vollmöller, "An Adaptive Higher Order Method for Solving the Radiation Transport Equation on Unstructured Grids," *J. Comput. Phys.*, vol. 178, no. 2, pp. 263–289, 2002.

[94] J. I. Castor, "Radiation hydrodynamics," Lawrence Livermore National Lab, Livermore, CA (United States), Tech. Rep., 2003.

[95] A. F. Nikiforov, V. G. Novikov, and V. B. Uvarov, *Quantum-Statistical Models of Hot Dense Matter: Methods for Computation Opacity and Equation of State (Progress in Mathematical Physics)*. Birkhauser, 2005.

[96] V. G. Novikov, V. V. Ivanov, K. N. Koshelev, V. M. Krivtsun, and A. D. Solomyannaya, "Calculation of tin emission spectra in discharge plasma: The influence of reabsorption in spectral lines," *High Energy Density Phys.*, vol. 3, no. 1, pp. 198–203, 2007.

[97] S. Faik, A. Tauschwitz, and I. Iosilevskiy, "The equation of state package FEOS for high energy density matter," *Comp. Phys. Comm.*, vol. 227, pp. 117–125, 2018.

[98] R. M. More, K. H. Warren, D. A. Young, and G. B. Zimmerman, "A new quotidian equation of state (QEOS) for hot dense matter," *Phys. Fluids*, vol. 31, no. 10, pp. 3059–3078, 1988.

[99] A. Kemp and J. M. ter Vehn, "An equation of state code for hot dense matter, based on the QEOS description," *Nucl. Instrum. Methods.*, vol. 415, no. 3, pp. 674–676, 1998.

[100] M. M. Basko and I. P. Tsygvintsev, "A hybrid model of laser energy deposition for multi-dimensional simulations of plasmas and metals," *Comput. Phys. Commun.*, vol. 214, pp. 59 –70, 2017.

[101] C. R. Phipps, T. P. Turner, R. F. Harrison, G. W. York, W. Z. Osborne, G. K. Anderson, X. F. Corlis, L. C. Haynes, H. S. Steele, K. C. Spicochi, and T. R. King, "Impulse coupling to targets in vacuum by KrF, HF, and CO_2 single-pulse lasers," *J. Appl. Phys.*, vol. 64, no. 3, pp. 1083–1096, 1988.

[102] P. W. Humrickhouse, "An equation of state and compendium of thermophysical properties of liquid tin, a prospective plasma-facing material," *IEEE Trans. Plasma Sci.*, vol. 47, no. 7, pp. 3374–3379, 2019.

[103] C. A. E. Peirce, C. Priest, T. M. McBeath, and M. J. McLaughlin, "Uptake of phosphorus from surfactant solutions by wheat leaves: Spreading kinetics, wetted area, and drying time," *Soft Matter*, vol. 12, pp. 209–218, 1 2016.

[104] L. Bourouiba, E. Dehandschoewercker, and J. Bush, "Violent expiratory events: On coughing and sneezing," *J. Fluid Mech.*, vol. 745, 537–563, 2014.

[105] B. E. Scharfman, A. H. Techet, J. W. Bush, and L. Bourouiba, "Visualization of sneeze ejecta: Steps of fluid fragmentation leading to respiratory droplets," *Exp. Fluids*, vol. 57, no. 2, 2016.

[106] J. Hernandez-Rueda, B. Liu, D. J. Hemminga, Y. Mostafa, R. A. Meijer, D. Kurilovich, M. Basko, H. Gelderblom, J. Sheil, and O. O. Versolato, "Early-time hydrodynamic response of a tin droplet driven by laser-produced plasma," *Phys. Rev. Research*, vol. 4, p. 013 142, 1 2022.

[107]   D. Hudgins and R. S. Abhari, "Rupture time of droplets impacted by a burst of picosecond laser pulses," *Phys. Rev. E*, vol. 99, p. 031 102, 3 2019.

[108]   Y. H. Jo, I. Jung, C. S. Choi, I. Kim, and H. M. Lee, "Synthesis and characterization of low temperature Sn nanoparticles for the fabrication of highly conductive ink," *Nanotechnology*, vol. 22, no. 22, p. 225 701, 2011.

[109]   J. Pstruś, "Surface tension and density of liquid In-Sn-Zn alloys," *Appl. Surf. Sci.*, vol. 265, pp. 50–59, 2013.

[110]   C. Clanet and J. C. Lasheras, "Transition from dripping to jetting," *J. Fluid Mech.*, vol. 383, pp. 307–326, 1999.

[111]   B. Ambravaneswaran, H. J. Subramani, S. D. Phillips, and O. A. Basaran, "Dripping-jetting transitions in a dripping faucet," *Phys. Rev. Lett.*, vol. 93, p. 034 501, 3 2004.

[112]   T. Driessen, R. Jeurissen, H. Wijshoff, F. Toschi, and D. Lohse, "Stability of viscous long liquid filaments," *Phys. Fluids*, vol. 25, no. 6, p. 062 109, 2013.

[113]   Y. Wang and L. Bourouiba, "Mass, momentum and energy partitioning in unsteady fragmentation," *J. Fluid Mech.*, vol. 935, A29, 2022.

[114]   T. Gancarz, Z. Moser, W. Gąsior, J. Pstrus, and H. Henein, "A Comparison of Surface Tension, Viscosity, and Density of Sn and Sn–Ag Alloys Using Different Measurement Techniques," *Int. J. Thermophys.*, vol. 32, pp. 1210–1233, 2011.

[115]   L. Rayleigh, "On the instability of jets," *Proc. Lond. Math. Soc.*, vol. s1-10, no. 1, pp. 4–13, 1878.

[116]   R. M. S. M. Schulkes, "The contraction of liquid filaments," *J. Fluid Mech.*, vol. 309, 277–300, 1996.

[117]   S. Gekle and J. M. Gordillo, "Generation and breakup of worthington jets after cavity collapse. part 1. jet formation," *J. Fluid Mech.*, vol. 663, 293–330, 2010.

[118]   M. J. Assael, A. E. Kalyva, K. D. Antoniadis, R. Michael Banish, I. Egry, J. Wu, E. Kaschnitz, and W. A. Wakeham, "Reference data for the density and viscosity of liquid copper and liquid tin," *J. Phys. Chem. Ref. Data.*, vol. 39, no. 3, p. 033 105, 2010.

LIST OF PUBLICATIONS

CHAPTER 2

B. Liu, D. Kurilovich, H. Gelderblom, and O. O. Versolato, *Mass Loss from a stretching semitransparent sheet of liquid tin*, Phys. Rev. Applied **13**, 024035 (2020).

CHAPTER 3

B. Liu⋆, R. A. Meijer⋆, J. Hernandez-Rueda, D. Kurilovich, Z. Mazzotta, S. Witte, and O. O. Versolato, *Laser-induced vaporization of a stretching sheet of liquid tin*, J. Appl. Phys. **129**, 053302 (2021).
⋆ These authors contributed equally.

CHAPTER 4

J. Hernandez-Rueda, B. Liu⋆, D. J. Hemminga, Y. Mostafa, R. A. Meijer, D. Kurilovich, M. Basko, H. Gelderblom, J. Sheil, and O. O. Versolato, *Early-time hydrodynamic response of a tin droplet driven by laser-produced plasma*, Phys. Rev. Research **4**, 013142 (2022).
⋆ B. Liu contributed to the design of the experiments, data collection, post-analysis, and part of the writing.

CHAPTER 5

B. Liu, J. Hernandez-Rueda, H. Gelderblom, and O. O. Versolato, *Speed of fragments ejected by an expanding liquid tin sheet*, Phys. Rev. Fluids **7**, 083601 (2022).

CHAPTER 6

B. Liu, R. A. Meijer, W. Li, H. Gelderblom, and O. O. Versolato, *Mass distribution of liquid tin sheets induced by laser pulse impact on droplets*.
In preparation.

The author has also contributed to the following publications:

J. Hermens, H. Gelderblom, B. Liu, J. Duffhues, P. Rindt, and O. O. Versolato, *Laser-impact-induced splashing: an analysis of the splash crown evolution after Nd:YAG ns-pulse laser impact on a liquid tin pool*, Appl. Phys. B **127**, 44 (2021).

R. A. Meijer, D. Kurilovich, B. Liu, Z. Mazzotta, J. Hernandez-Rueda, O. O. Versolato and S. Witte, *Nanosecond laser ablation threshold of liquid tin microdroplets*, Appl. Phys. A **128**, 570 (2022).

Acknowledgments

I still remember the thrilling feeling when I received the email that offered me the position of PhD student at ARCNL. I can also remember my first lab visit to our group at the old concrete building of ARCNL. I was overwhelmed by the tangling BNC cables, the vacuum chamber made of shining metal with numerous view-ports, and the stable noise made from the pumps in the lab. Starting my PhD as a master student who was mainly working on numerical studies and had barely any experience in a lab is, no doubt, extremely challenging. Looking back at all that I have gone through during my PhD, I feel nothing but gratitude.

First, I would like to thank my two promoters, Oscar Versolato and Hanneke Gelderblom. Oscar, I want to express my deepest appreciation for the opportunity to join the group and for your trust. I must say that I have been constantly impressed by the vitality you have every day and by your extreme passion for new knowledge. This work would not have been possible without your guidance, encouragement, and inspiration throughout my PhD research. Hanneke, you have provided me with guidance and suggestions on my research since my Master. I have always enjoyed talking to you. I am very much looking forward to our new collaboration in the future. I would also like to thank Wim Ubachs and Ronnie Hoekstra for their input to my research in our weekly group meeting.

It was a great privilege to work with my colleagues at ARCNL. Working in a multidisciplinary group allows me to significantly broaden my scope. I want to thank Dmitry Kurilovich, Ruben Schupp, Francesco Torretti, Joris Scheers, and Alex Bayerle, particularly for the help and guidance at the beginning of my PhD, and also for the recent suggestion for my future career. Furthermore, I could not have undertaken this journey without the contributions and help of Randy Meijer, Javier Hernández Rueda, Lars Behnke, John Sheil, Diko Hemminga, Adam Lassise, Laurens van Buuren, Zoi Bouza, Lucas Poirier, Yahia Mostafa, Edcel Salumbides, Dion Engels, Karl Schubert, Stan de Lange, Sander Schouwenaars, Jane Babenko, and Mardou Bijker. You guys are not only my colleagues, but also my teachers on basic optics, beam alignment,

致谢

时光飞逝，不知不觉已经是我来荷兰的第八个年头。回想从研究生一路走到这里，我心怀感恩，因为一路上有太多帮助过我的朋友们。是你们让我即使作为一个身处异国他乡的游子也能时常感到温暖。

较瘦(AKA 王佳南)，言语不尽对你在博士期间对我的的帮助和扶持。祝我们在Diemen的峥嵘岁月长存，也祝你也能早日完成学业，和兴宇弟妹百年好合！鞠季宏（AKA 炸过的土匪）还有高晓旭（AKA 上海房姐），你们分别是我在荷兰认识的第一个和第二个中国人。很荣幸能有你们这样的朋友。祝你们工作顺利，早生贵子！JJ (AKA 李金骏)，你是我在荷兰认识的第三个中国人。感谢你从硕士期间就开始的长久以来的支持还有帮助。祝你学业有成，也祝嫂子工作顺利！洋哥，即使多年过去，在瓦格宁根第一次看到你那初音贴纸的PSP给我带来的震撼依旧记忆犹新。你一直是我学习的榜样。作为擎天之玉柱，架海之津梁，祝你工作，生活一切顺利！

我衷心感谢我在ARCNL的中国同事们，凤苓，阿姆诗人Kevin刘，杜峻晓，聂忠辉老师，肖晨博士，洲萍，杜梦琪，李伟博士，彭亮。你们在我工作中以及生活中的帮助不可或缺。没有你们的支持和帮助，我恐怕难以完成我的博士。祝你们在今后的工作中顺利！我也借此机会感谢我在Science Park认识的伙伴们，阿耿，天翼，璇姐。感谢在你们家蹭过的饭，一起的coffee break，以及一起在我司吃过的午饭。同样祝你们工作顺利！当然，我也感谢我平常一起打球的伙伴们：宝烘，亚辉，还有广然。在异国他乡还能找人一起组组养身篮球局真的是一件很幸福的事情。祝你们在荷兰随后的岁月一切顺利！特别感谢我在卡迪夫的兄弟涛哥。作为高中的同桌，我们之间不必客气了，虽然你承诺的请我伦敦九宫格火锅已经从2017年说到现在... 总之，祝你早日毕业，博士顺利！我也要特别感谢我在国内的同学陈运起。2020春夏之际，欧洲疫情初期，你给我从国内寄来了关键的两包口罩。这些东西在当时来说的重要性不言而喻。感谢！等我回国了，咱们好好面聊！

最后，我想感谢我的父母。你们的支持和鼓励永远是我温暖的港湾。还有太多的人我需要感谢，碍于词汇匮乏，言不能尽。此时此刻，我怀着感激的心情，感叹我如此幸运，能在短短的几年之内认识如此多优秀的朋友。合上

这本论文的最后一页，并不代表一个结束，而是下一个新的开始。我也祝愿我自己，能在新的道路上，充满希望，勇敢前行。

刘博
阿姆斯特丹, 2022, 十月